Laser and wave-guides system for endoscopic/fiberscopic laser surgery

Inaugural dissertation

to

be awarded the degree of Dr. sc. med.

presented at
the Faculty of Medicine
of the University of Basel

by

Lina M. Beltrán Bernal

From Bogotá, Colombia

Basel, 2021

Approved by the Faculty of Medicine

On application of

Prof. Dr. Azhar Zam, University of Basel, First examiner
Prof. Dr. Philippe C. Cattin, University of Basel, Second examiner
Prof. Dr. Niklaus F. Friederich, Further advisor
Prof. Dr. Alfred Vogel, External expert

Basel, 22nd March, 2021

Dean
Prof. Dr. Primo Leo Schär

To my parents Mary Bernal and Julio Beltrán, and my brother Andrés Beltrán.

Acknowledgments

First, I am extremely grateful to my supervisor Prof. Dr. Azhar Zam for giving me the opportunity to work in such an amazing PhD project, for the discussion, for his support during my studies and the development of my project. I would also like to extend my deepest gratitude to Prof. Dr. Philippe Cattin, for the discussions, for his support, for his ability to manage so well the MIRACLE project. I am very grateful to Prof. Dr. Alfred Vogel, for his willingness to be my external examinator, and take the time to read my thesis. I thank my colleagues, Dr. Ferda Canbaz, Dr. Hamed Abbasi, Yakub Bayhaqi, Dr. Hervè Nguendon, and Arsham Hamidi for their friendship, their company, their support, the discussions and the leisure time we have shared. I would like to thank colleagues who left long time ago: Iris Schmidt, Irena Sugiarto, Antoine Droneau, and Olivia Kindongo. I am also very grateful to Prof. Dr. Georg Rauter and his team, especially to Manuela Eugster for the joint projects we worked on together, and for their support. I want to express my gratitude to Prof. Dr. Niklaus Friederich for the fruitful discussions we had about medical applications, for reading all my papers and giving me his inputs. I want to acknowledge Prof. Dr. Andrea Barbero, Dr. Karoliina Pelttari, and Dr. Salim Darwiche for all the support and help I have received from them. I am grateful to Marek Zelechowski, Sara Freund, Samaneh Manavi, Neha Sharma, and Olivier Braissant for their help when I needed it. Special thanks to the great team behind the MIRACLE project, especially to Constanze Dorothee, Gabriela Osser, Daniela Vavrecka-Sidler, Corinne Eymann-Baier, and Beat Fasel.

Last but not least, I am so grateful to the God of the heaven for the opportunity of being here, for making all this possible. I want to thank my family, especially my parents, Mary Bernal and Julio Beltrán, and my brother Andrés Beltrán Bernal and his family (Lida Huertas and Juano), for their great support, for the strong relashionship we have built even being so far away. Without my family, I would not have had enough motivation for doing this. I thank my boyfriend Alejandro Durán for his support, for being with me every time, for bringing happiness and motivation to my life, and I also express my gratitude to his family, they are also a great support for me. I would also like to thank my friends, Cindy Montenegro, Martin Frei, Jennifer Bohler, Ramiro Cardona, the Cool-Gsteigstrasse team, the Monachos team, especially Caori Organista for her infinite friendship. Finally, I would like to thank every single person I could not mention here, who has helped me, who has given me inputs, ideas, motivation, and good wishes.

Basel, February 2021
Lina M. Beltrán Bernal

Contents

List of acronyms and abbreviations ix

Summary 1

Zusammenfassung 2

Chapter 1 – Introduction 3
1.1 Motivation . . . 3
1.2 Contribution . . . 4
1.3 Outline . . . 4

Chapter 2 – Properties of laser beams and fiber optics 7
2.1 Stimulated absorption, spontaneous emission, and stimulated emission . . . 7
2.2 Light Amplification by Stimulated Emission of Radiation: LASER . . . 8
2.3 Paraxial wave equation and Gaussian beams . . . 14
2.4 Basics of fiber optics . . . 24

Chapter 3 – Laser ablation of biological tissue 29
3.1 Lasers in medicine . . . 29
3.2 Laser-tissue interaction . . . 30
3.3 Ablation of hard tissue with pulsed lasers . . . 34

Chapter 4 – Exploring Er:YAG laser and water irrigation for bone ablation 47

Chapter 5 – Optimizing Er:YAG laser for deep bone ablation 69

Chapter 6 – Laser ablation of bone through optical fibers 91

Chapter 7 – Discussion and conclusion 105
7.1 Discussion . . . 105
7.2 Future research . . . 107
7.3 Conclusion . . . 107

Bibliography 109

Curriculum vitae 117

Acronyms and abbreviations

MIRACLE *Minimally Invasive Robot-Assisted Computer-guided LaserosteotomE*

LASER *light amplification by stimulated emission of radiation*

CW *continuous wave*

Er:YAG *erbium-doped yttrium aluminium garnet*

Cr^{3+}:Al_2O_3 *ruby*

Nd:YAG *neodymium yttrium aluminium garnet*

Ar^+ *argon ion*

q(z) *complex parameter*

R(z) *radius of curvature*

w(z) *beam radius at the propagation position z*

w_0 *beam waist radius at $z = 0$*

Z_R *Rayleigh length*

TEM *transverse electromagnetic mode*

M^2 *beam quality factor*

NA *numerical aperture*

GaAs *gallium arsenide*

He-Ne *helium–neon*

ArF *argon fluoride*

Nd:YLF *neodymium-doped yttrium lithium fluoride*

CO_2 *carbon dioxide*

Er,Cr:YSGG *erbium-chromium-dopped yttrium-scandium-gallium garnet*

Ho:YAG *holmium-doped yttrium aluminium garnet*

Ti:Sapphire *titanium-doped sapphire*

Nd:YVO_4 *neodymium-doped yttrium orthovanadate*

CPA *Chirped Pulse Amplifier*

PDT *photodynamic therapy*

ECM *extracellular matrix*

UTS *ultimate tensile strength*

GeO_2 *germanium oxide*

Al_2O_3 *sapphire*

ZrF *zirconium fluoride*

HSW *hollow-core silica waveguide*

Summary

Laser technology in medical applications is a fascinating field for both scientific and non-scientific societies. The main motivation for using lasers in medicine is to attain a contactless procedure, which lowers the risk of viral and bacterial infections, and leads to a less painful, more flexible and, often, faster procedure. Lasers are capable of ablating even the most rigid tissues, such as bone. For this thesis project, a laser system for deep bone ablation was optimized, with the ultimate purpose of implementing the laser system in an endoscopic device for minimally invasive bone surgery.

In the first part of the thesis, an *erbium-doped yttrium aluminium garnet* (Er:YAG) laser was optimized and paired with a suitable irrigation system to cool down the tissue, and with a feedback system to control the tissue temperature and prevent carbonization. The irrigation system consisted of a novel water jet measuring 50 μm in diameter at 30 bar pressure. The water jet was very fine and its laminar flow regime reached up to 15 cm, making it very useful for irrigation during deep bone ablation. With this optimized laser system, it was possible to reach ablation depths of up to 21 mm in cortical bone.

In the second part of the thesis, the Er:YAG laser was coupled into different fibers: germanium oxide, sapphire, zirconium fluoride, and a hollow-core silica waveguide. Ultimately, a germanium oxide fiber was selected. The beam was refocused using a suitable miniaturized lens system; with this setup, ablation depths of up to 10 mm in cortical bone were achieved.

The results obtained in this thesis open up the possibility of further optimizing laser and fiber systems to achieve greater ablation depths in less time. This thesis was part of the *Minimally Invasive Robot-Assisted Computer-guided LaserosteotomE* (MIRACLE) project, which aims to develop a robotic endoscope to perform laser-based, contact-free bone surgery.

Zusammenfassung

Lasertechnologie in der Medizin ist ein faszinierendes Feld für die wissenschaftliche wie auch die nichtwissenschaftliche Gemeinschaft. Die Hauptmotivation für den Einsatz von Lasern in der Medizin besteht darin, einen berührungslosen Eingriff zu ermöglichen, was das Risiko von viralen und bakteriellen Infektionen senkt und zu einem weniger schmerzhaften, flexibleren und oft auch kürzeren Eingriff führt. Laser ermöglichen auch das Abtragen von hartem Gewebe, wie beispielsweise Knochen. In dieser Dissertation wurde ein Lasersystem für tiefe Knochenschnitte optimiert, mit dem letztendlichen Ziel, das Lasersystem in ein endoskopisches Instrument zu integrieren und damit minimal invasive Knochenchirurgie zu ermöglichen. Im ersten Teil der Arbeit wurde ein Er:YAG-Laser optimiert und mit einem geeigneten System zur Kühlung und Befeuchtung des Gewebes, sowie einem Rückkopplungssystem zur Kontrolle der Gewebetemperatur und zur Vermeidung von Karbonisierung ausgestattet. Das Kühlungs- und Befeuchtungssystem bestand aus einem neuartigen Wasserstrahl, mit einem Durchmesser von 50 μm bei einem Druck von 30 bar. Der Wasserstrahl war sehr schmal und sein laminares Strömungsregime reichte bis zu 15 cm, was ihn für die Kühlung und Befeuchtung des Gewebes bei tiefen Knochenschnitten sehr nützlich macht. Mit diesem optimierten Lasersystem konnten im kortikalen Knochen Schnitttiefen von bis zu 21 mm erreicht werden.

Im zweiten Teil der Arbeit wurde der Er:YAG-Laser in unterschiedliche Lichtleitfasern aus unterschiedlichen Materialien eingekoppelt; Germaniumoxid, Saphir, und Zirkoniumfluorid. Auch eine Hohlkern-Silizium Lichtleitfaser wurde getestet. Letztendlich wurde eine Germaniumoxid-Lichtleitfaser ausgewählt und der Laserstrahl wurde nach der Lichtleitfaser mit einem geeigneten Linsensystem fokussiert. Mit diesem Aufbau wurden im kortikalem Knochen Schnitttiefen von bis zu 10 mm erreicht. Die in dieser Arbeit erzielten Ergebnisse ermöglichen es, Laser- und Lichtleitfasersysteme weiter zu optimieren, um in kürzerer Zeit tiefere Knochenschnitte zu realisieren. Diese Arbeit war Teil des Projekts “Minimally Invasive Robot-Assisted Computer-guided LaserosteotomE” (MIRACLE), welches die Entwicklung eines robotischen Endoskops zur Durchführung von laserbasierter, berührungsfreier Knochenchirurgie zum Ziel hat.

Chapter 1

Introduction

1.1 Motivation

Osteotomy is a surgical operation that has been used since ancient times, especially for bone alignment. Bone alignment can provide the patient with better posture by correcting affected areas of the skeleton. Several traumas generated in the bones, induced either by accidents or diseases, can only be fixed by means of osteotomy. For example, pain due to arthritis in the knee can be relieved by removing a wedge from the tibia, on the side with healthy cartilage. The procedure allows the patient to shift their body weight by tilting the tibia and femur toward the healthy side, removing weight from the damaged cartilage [1]. Osteotomy is also necessary to correct hip dysplasias or deformities. Here, sections of the hip joint are removed to stabilize alignment, thereby improving the patient's posture [2]. Osteotomy of the jaw is needed when some malocclusions, such as severe mandibular retrognathia, cannot be corrected with orthodontics. Mandibular retrognathia is a deformity of the jaw joints such that both jaws are misaligned with respect to one another. The lower first molar is posterior to the upper first molar. Orthognathic surgery (a type of osteotomy) is performed on the jaws to correct the patient's occlusion [3].

New technologies have improved osteotomy procedures, however, conventional oscillating saws and drills are still in use. Among the drawbacks of using mechanical tools are vibrations and mechanical stress, and the risk of contamination due to contact, especially in the case of open surgeries, leading to prolonged healing processes. With the use of mechanical tools, it is very difficult to achieve the flexible shape desired by surgeons. Lack of flexibility can lead to inadequate surgical practices, compromising functionality, aesthetics, and stability of the region where the surgery has been performed. The risk of contamination, along with large lesions and delayed healing times, have decreased with new approaches for minimally invasive surgeries. In minimally invasive surgeries, smaller openings are made in the skin and smaller tools are introduced into the body, resulting in less trauma [4].

Shortly after the first realization of the laser by Mainman in 1960 (Ruby laser) [5], researchers began investigating the effect of lasers on biological tissues, envisioning diagnostic and treatment applications with laser light [6–9]. For treatment applications, laser ablation of hard tissues has been investigated extensively. Several studies demonstrate efficient ablation of hard tissue (dentin, enamel, bone, cartilage) with lasers, especially with those in the mid-infrared wavelength region [10–12]. Based on these studies, *laserosteotomy*, that is, cutting bone with lasers, has become a promising tool to overcome the current challenges of standard osteotomy with mechanical implements. Lasers allow for contactless cutting, free and flexible cutting shapes, and localized ablation that minimizes heat in the surrounding tissue. Therefore, the side effects of conventional osteotomy techniques can be overcome by implementing lasers instead. Lasers delivered by means of optical fibers can be used in minimally invasive procedures [13], reinforcing the enormous potential of laserosteotomy.

Currently, the extent to which laser technology is implemented in clinics for deep ablation ($\geqslant 1\,\mathrm{cm}$) of hard tissues is very limited, and has not yet been reported in the literature. The first robotic device used for laserosteotomy in clinics was a free-space laser called CARLO® [14–16]. The device performed the world's first clinical bone surgery on 3 July 2019. It was used for a mid-face human laserosteotomy *in vivo* at the Department of Oral and Maxillofacial Surgery, University Hospital Basel, Switzerland. CARLO® has been used to operate on 28 patients since early July 2020, at the University Hospital Basel. Minimally invasive laserosteotomy requires additional technologies in the field of fiber optics. The Swiss flagship project MIRACLE, short for *Minimally Invasive Robot-Assisted Computer-guided LaserosteotomE*, at the University of Basel, aims to build such a device. The MIRACLE project has envisaged an endoscopic device capable of deep bone ablation in minimally invasive procedures, using lasers delivered through optical fibers.

1.2 Contribution

The PhD project presented in this thesis provided an efficient ablation laser for the MIRACLE flagship project. First, a free-space laser and irrigation system was optimized for deep bone ablation, achieving a maximum depth of 21 mm in pure cortical bone. Next, high-power laser delivery through optical fibers was optimized by exploring the maximum capacity of the fibers to transmit laser light. Finally, bone was ablated by means of an optical fiber and a miniaturized refocusing lens system, resulting in deep bone ablation up to a maximum depth of 10 mm. With these achievements, the first prototype for endoscopic laser ablation was developed for the MIRACLE project.

1.3 Outline

The following two chapters present the main concepts underlying this research and its results. In the first part of Chapter 2, the basic concepts of *light amplification by stimulated*

emission of radiation (LASER) are explained. The second part of Chapter 2 describes the principles of fiber optics, whereby the laser light is transported through wave-guides, making the delivery system to the ablation zone more compact and flexible. Chapter 3 describes the concepts of laser-tissue interaction, focusing on bone ablation. The theory presented in Chapters 2 and 3 formed the basis for understanding and developing a laser system that would meet the needs of the MIRACLE project. Chapters 4, 5, and 6 contain the publications that show the results obtained from the research project. Chapter 4 reviews studies showing the feasibility of using Er:YAG lasers for hard tissue ablation, the implications of using water for cooling (first paper), and attempts to optimize the lateral speed of line ablation in bone (second paper). Chapter 5 describes the optimized Er:YAG laser parameters and a novel irrigation system for deep bone ablation in free-space. Chapter 6 is a study of laser coupling in fibers suitable for transmitting the Er:YAG laser light. Using the optimized irrigation system and the main results outlined in Chapter 5, ablation through optical fibers was made possible. The thesis concludes in Chapter 7 with a discussion of the findings, outlook for future research, and some closing remarks.

Chapter 2

Properties of laser beams and fiber optics

2.1 Stimulated absorption, spontaneous emission, and stimulated emission

Let's assume a quantum system (e.g., a molecule, an atom, an ion, or a subatomic particle) of two energy levels; the ground level E_1 and an excited state E_2. When the atomic particle remains in the ground level and an external electromagnetic wave of frequency ν and energy $E_2 - E_1 = h\nu$ (h is the Planck's constant $h = 6.626 \times 10^{-34}$ Js [17]), is incident on the material, the particle undergoes a transition to an excited state of energy E_2, this is called a *stimulated absorption* process [18].

The transition from an excited energy state E_2 to the ground energy state E_1 is a decay. One possible decay is the *spontaneous emission*. In spontaneous emission, by energy conservation principle, the quantum system decays by emitting a quantized amount of energy; a photon, with energy $E_2 - E_1 = h\nu$.

In contrast, if the excited-state particle is perturbed by an electromagnetic wave of frequency ν, an additional photon with the same phase, polarization, frequency, and direction of travel as the photons of the incident wave will be emitted, this process is called *stimulated emission*.

The energy transitions described above are probabilistic processes, an illustration is shown in Fig. 2.1.

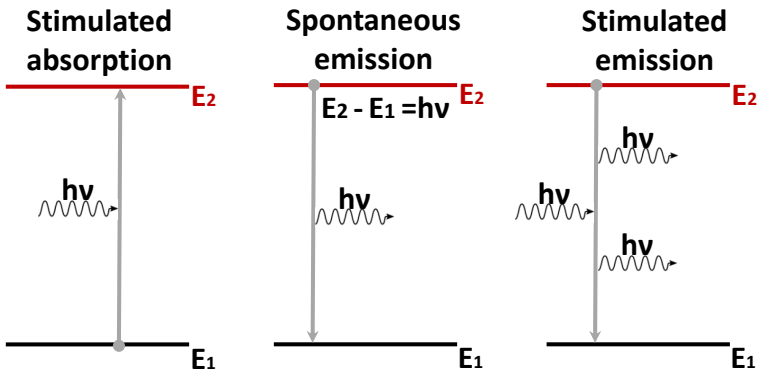

Figure 2.1: Illustration of the stimulated absorption, spontaneous emission, and stimulated emission processes. Image adapted with permission from [18].

2.2 Light Amplification by Stimulated Emission of Radiation: LASER

The main components of a laser are an energy source or pump, a gain or active medium, and an optical resonator or cavity. For simplicity, let's consider the gain medium as the two-level quantum system described in the previous section. The electrons of the atoms in the gain medium can be excited from the ground energy state E_1 to an excited energy state E_2 by the action of an external source (the pump) via *stimulated absorption*. For this process to happen, the pump must have energy $E_2 - E_1 = h\nu$. The electron rapidly returns to the ground state releasing a photon of energy $E_2 - E_1$ by *spontaneous emission*. When the electron is already in an excited state and interacts with a stimulating photon, this photon perturbs the electron and forces it to return to the ground state, and emits a photon via *stimulated emission*. The emitted photon ideally has the same frequency, phase, direction, and polarization as the stimulating photon [18]. This process must be generated multiple times to produce amplification of the laser light. There is no possibility to produce laser light via spontaneous emission, since the photons released go in a random direction [19]. For an electron to undergo stimulated emission instead of spontaneous emission, there must be enough time for the transitions. As the photon emitted by spontaneous emission serves as the seed to trigger an avalanche of stimulated emissions in the atoms, and since the lifetime of an electron in an excited state is too short, the result is that there will not be enough excited atoms nearby to undergo stimulated emission. Therefore, to generate stimulated emission, the upper state must have a longer lifetime. This usually never happens in a two-level system, instead, a more realistic system is called quasi-three-level system. Here the two energy levels are two manifolds (or Stark level manifolds: groups of energy levels which have very similar energies due to the Stark effect [20]) whose energy levels E_{1a}, E_{1b} and E_{2a}, E_{2b} are very close to each other (see Fig. 2.2).

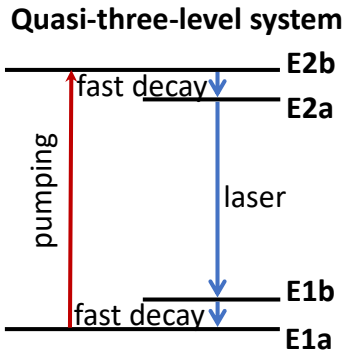

Figure 2.2: Diagram of a quasi-three-level system.

When the gain medium is pumped and the electron is excited to the upper state E_{2b}, the electron undergoes a fast decay called radiationless transition in the upper manifold, where no photons are emitted. In the fast decay, the energy is dissipated, for example in the form of heat. The lower manifold state E_{2a} in the upper energy level has a longer lifetime, allowing the stimulated emission to happen. In addition, to ensure stimulated emission, the probability that a stimulating photon is absorbed must be minimized. This leads us to the concept of population inversion, see Section 2.2.1. As stimulated emission occurs, more and more stimulating photons interact with the atoms inside the optical resonator composed of two mirrors, one highly reflective and one partially transmissive (Fig. 2.3), allowing partial transmission of the generated photons to go outside the cavity, those photons form the *laser beam*. To keep the process going, many generated photons stay in the cavity amplifying the laser light.

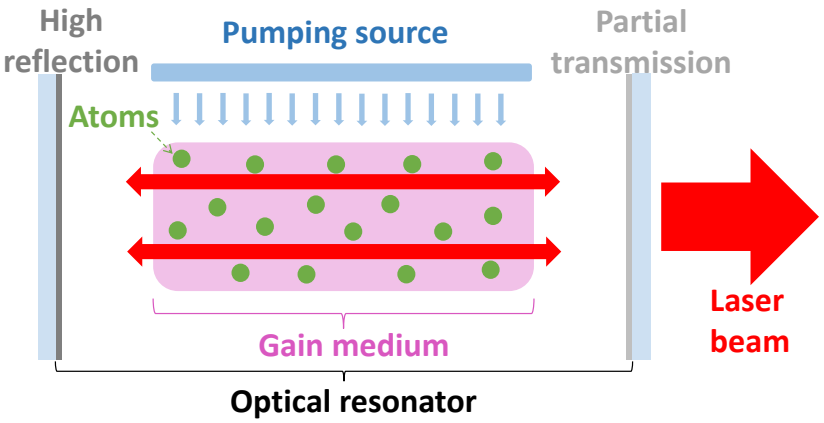

Figure 2.3: Schematic of a typical laser.

2.2.1 Population inversion

Once the gain medium has more atoms in an excited state than in a lower energy state, the gain medium undergoes *population inversion*, meaning that the thermal equilibrium condition (when absorption predominates) is not anymore fulfilled. When the population inversion is achieved, the rate of stimulated emission is higher than the rate of absorption of light in the medium, producing an *amplification* of the light. However, this scheme would not be efficient because it requires very strong pumping to send the electron back to the excited state. While pumping the active medium, the incoming wave would produce more transitions from level 1 to level 2 than from level 2 to level 1 [18, 19]. After a while the absorption and the stimulated emission will compensate to each other, the system is called *two-level saturation*. Under this scheme, the laser will never work because the population inversion cannot be achieved. The most common laser schemes are referred to *quasi-three-level system* (Fig. 2.2), *three-level system*, and *four-level system* (Fig. 2.4).

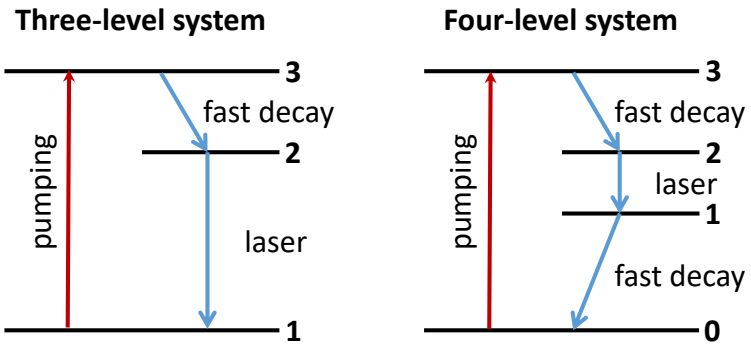

Figure 2.4: Diagrams of three- and four-level laser systems. Image adapted with permission from [18].

In a three-level system, the atoms are raised from the ground level 1 to an excited level 3, if the atoms rapidly decay to level 2 (e.g by radiationless decay), then, the population inversion can be obtained between level 2 and level 1. In a four-level system, the atoms are raised from the ground level 0 to an excited level 3. Again, if the atom rapidly decays from level 3 to level 2, a population inversion can be obtained between levels 2 and 1. An example of three-level system is the first laser ever built; the *ruby* (Cr^{3+}:Al_2O_3) laser [5]. Examples of four-level system are the Er:YAG laser at wavelength 2.94 μm and the *neodymium yttrium aluminium garnet* (Nd:YAG) laser at 1064 nm [18, 21].

2.2.2 Types of lasers

In general, laser systems are classified in *continuous wave* (CW) and *pulsed* lasers, some lasers operate in both ways. Although all lasers have the same principle of operation,

there are different types of medium. The most common types of lasers are *gas*, *liquid*, *solid-state crystal*, *semiconductor*, and *optical fiber* [22]. In Chapter 3, the lasers which are mainly used in medicine will be described.

Er:YAG laser operation

In erbium doped lasers, the transition between the upper active level $^4I_{11/2}$ and the lower level $^4I_{13/2}$ allows laser output near 3 μm. The Er:YAG is a solid-state laser, whose crystal Er^{3+}:YAG has a *yttrium aluminium garnet* (YAG) host and a 50 % doping concentration of Er^{3+} ions. Figure 2.5 shows a diagram of the lowest energy levels of the laser crystal and the most important transitions that allow having emission at the oscillation wavelength of 2.94 μm in a four-level system.

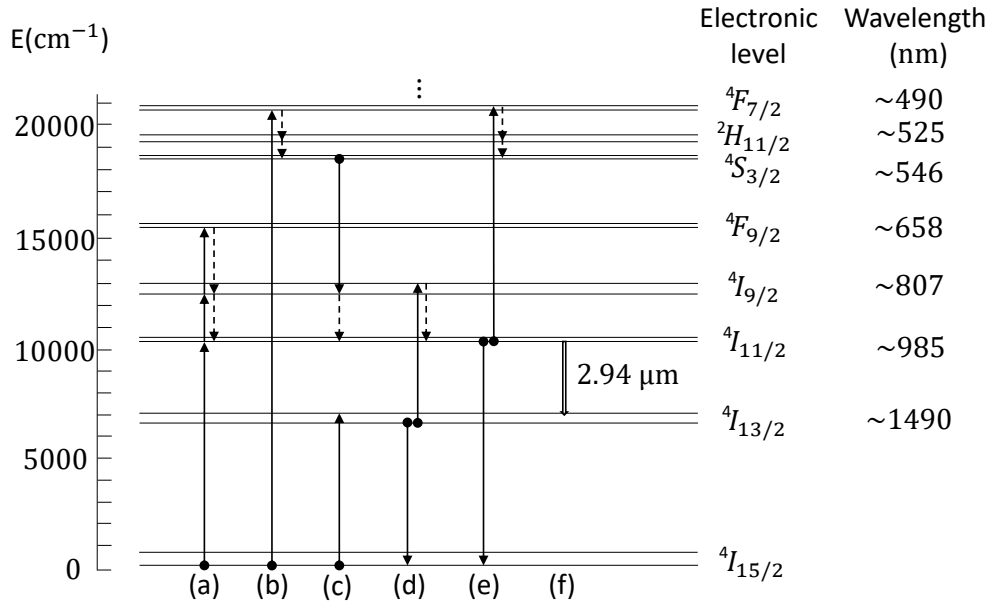

Figure 2.5: Diagram of the lowest energy levels of the Er^{3+}:YAG crystal and the most important transitions that allow to obtain laser emission at 2.94 μm. (a) Direct pumping. (b) Indirect pumping. (c) Cross relaxation. (d) Upconversion from the lower laser level. (e) Upconversion from the upper laser level. (f) Laser transition: emission at $\lambda = 2.94\,\mu$m. Image adapted with permission from [23].

The Er:YAG laser transition is very particular since the upper laser level $^4I_{11/2}$ has shorter lifetime ($\tau_2 = 0.12$ ms) than the lower laser level $^4I_{13/2}$ ($\tau_1 = 7.25$ ms) [24]. In classical laser theory, the population inversion in a four-level system where $\tau_1 > \tau_2$ would not produce CW laser operation mode, because it assumes only one transition from the upper level (Fig. 2.5(f)), therefore the system would lase only in a pulsed self-terminating mode [25], which is the most common Er:YAG high-power laser operation available.

However, efficient CW laser operation has been achieved due to the existence of other transitions from the upper state, and to the splitting of the laser levels into manifolds [24]. Two pumping mechanisms are produced in Er:YAG lasers; direct and indirect pumping [23]. Direct pumping (Fig. 2.5(a)) encompasses the ground state absorption of the Er^{3+} ions and the excitation to the energy levels ${}^4I_{11/2}$, ${}^4I_{9/2}$, and ${}^4F_{9/2}$, followed by a nonradiative relaxation of ${}^4I_{9/2}$ and ${}^4F_{9/2}$ to the upper laser level ${}^4I_{11/2}$. The indirect pumping (Fig. 2.5(b)) consists of shorter wavelength excitation to the energy levels ${}^4S_{3/2}$, ${}^2H_{11/2}$, and ${}^4F_{7/2}$, and subsequently, a nonradiative relaxation of ${}^2H_{11/2}$ and ${}^4F_{7/2}$ to the level ${}^4S_{3/2}$. An ion from this level and a ground state ion produce cross relaxation (Fig. 2.5(c)), populating both the upper ${}^4I_{11/2}$ and the lower laser level ${}^4I_{13/2}$. This mechanism helps the two upconversion mechanisms present in the Er:YAG laser; upconversion from the lower laser level (Fig. 2.5(d)), and from the upper laser level (Fig. 2.5(e)) [26]. At sufficient high pumping rate, the multiple transitions of the Er:YAG laser suppress the pulsed self-terminating mode allowing an efficient CW operation [27, 28].

2.2.3 Main properties of laser beams

The capacity of the laser to have high degree of (1) monochromaticity, (2) coherence, (3) directionality, (4) radiance, and (5) short time duration, makes it differ from other laser sources [18].

Monochromaticity

Laser beams can have a very narrow spectrum band, therefore, the emitted wavelength λ is, in many cases well defined. For example, for lasers in the visible spectrum, their emitted *color* is unique. Due to the quantized energy levels of the atom, the electromagnetic wave has a defined frequency as well, namely ν, described in Sec. 2.1. The first reason why the wavelength of the laser has narrow band is that only the electromagnetic wave of frequency ν can be amplified in the gain medium, providing a unique wavelength, related to the frequency through the relation $\lambda = c/\nu$, where c is the speed of light in vacuum; $c \approx 2.998 \times 10^8$ m/s. The second reason is that the cavity composed of two mirrors can only resonate at the resonant frequencies of the cavity.

Directionality

The high directionality of a laser beam means that the beam has very small divergence. This property comes from the fact that the wave propagates in a resonant cavity composed of two mirrors, the waves orthogonal to the mirrors are the ones that are amplified and therefore go outside the cavity, forming the laser beam. The laser beam is relatively narrow and travels in a specific direction, parallel to the resonant cavity. The divergence of a beam can be obtained in the far field as $\theta = w(z)/z$; where θ is the half-angle beam divergence, $w(z)$ is the beam radius at the propagation position z. The divergence of a laser beam can be determined in different ways depending on the type of beam present in

the cavity. We are interested in lasers producing Gaussian beams, this will be discussed in Sec. 2.3.

Coherence

The two concepts of coherence are the *temporal coherence* and the *spatial coherence*, both are characteristics of a laser, and are independent to each other.

The spatial coherence is given when two points that belong to the same wave front (along the laser's beam profile) of the electromagnetic wave, keep a fixed phase difference at different times. In reality, for having a high space coherence, the two points remain on a finite area with respect to each other, this is partial spatial coherence. The high spatial coherence is a prerequisite for strong directionality of the beam. For measuring the spatial coherence degree, the phase front fluctuation of the wave should be measured by means of a wavefront sensor which is available in the market. However, those sensors are usually expensive. For a laser with Gaussian beam distribution, a sense of the spatial coherence degree can be given by the beam quality measurement. The beam quality provides information about how the beam differs from an ideal Gaussian beam with perfect spherical wavefront. A more detailed explanation about the beam quality will be discussed in Sec. 2.3.5.

The temporal coherence is given when the electric field at a certain point of the wavefront and the electric field at the same position but at a different time are highly correlated. The temporal coherence provides information about the monochromaticity of the laser through the coherence time or length. One way to measure the coherence time of a laser is by means of an spectrometer, which can be used to determine the spectrum bandwidth $\Delta\lambda$ of the laser. The coherence length is given by $L_c = c/n\Delta f$, where $\Delta f = c/\Delta\lambda$, and n is the refractive index of the medium where the light is traveling. For instance, a single mode Nd:YAG laser has a coherence length of 15 km [18].

Radiance (Brightness)

Due to the high directionality of the laser beam, the power of a laser can be easily concentrated in a very small beam area. An example is the comparison between one of the brightest commercial light source; a Mercury vapor lamp of output optical power $P = 10\,\mathrm{W}$ at its most intense line $\lambda = 546\,\mathrm{nm}$, and an *argon ion* ($Ar^+$) laser of wavelength $\lambda = 514\,\mathrm{nm}$ and output optical power $P = 1\,\mathrm{W}$. The radiance of the lamp is $L \cong 95\,\mathrm{W/cm^2 \times sr}$, and the radiance of the laser, calculated as $L = (4P/\lambda^2)$ as it is diffraction limited is $L \cong 1.6{\times}10^9\,\mathrm{W/cm^2 \times sr}$. The radiance of the Argon ion laser is 7 orders of magnitude above the radiance of the lamp [18]. In general, the laser beams have greater radiance than any other light sources.

Short time duration

Another important property of laser beams is their capability to concentrate their energy in a very short time, leading to high peak power. Shortening the time can be achieved

by changing the initial CW mode to pulsed mode by techniques like *Q-switching*, *mode-locking*, or by *pulsed pumping* in case the laser cannot operate at CW. The Q-switching operation produces short laser pulses typically of few tens of nanoseconds, and peak power of the order of gigawatts. For Q-switching, a variable attenuator called Q-switch is placed inside the cavity to prevent the laser amplification to happen, increasing the energy losses and therefore the quality factor Q of the cavity. However, allowing the population inversion to happen. Meanwhile, the pumped energy is being stored in the cavity until reaching a saturation point. When the cavity reaches the saturation, the attenuator mode is switched to decrease the energy losses. Afterwards, the amplification occurs and therefore the pulsed laser is produced. The Q-switch device can be active when it is externally controlled, or passive when the Q-switch is such that its transmission is increased when the energy exceeds a certain threshold, it is called saturable absorber. The mode-locking operation produces ultrashort laser pulses down to tens of femtoseconds. Unlike the Q-switching technique, in mode-locking technique the laser amplification and therefore the stimulated emission are not prevented to happen. Instead, a rapid light modulator inside the cavity is used to divide the light into periods of the length of a round trip in the cavity. The pulses duration depends on the Fourier transform of the spectrum of the laser; the pulses get shorter as the spectrum gets wider. Laser pulses can be also obtained by pumping the active medium with a pulsed light source or a pulsed laser itself. The laser pulses produced when the pumping source is pulsed are usually much larger than the ones produced with Q-switching, reaching up to ms pulse durations. Active Q-switching of a flashlamp-pumped high-power Er:YAG laser has been achieved by using a mechanically spinning mirror as part of the cavity of the laser; output energy as high as 805 mJ with a pulse duration of 61 ns at 1 Hz repetition rate was achieved [29].

2.3 Paraxial wave equation and Gaussian beams

2.3.1 Wave equation

Considering a medium with no charges (charge density $\rho = 0$) and no currents (current density vector $\boldsymbol{J} = 0$), the Maxwell's equations are simplified as follows [30]:

$$\nabla \cdot \boldsymbol{E} = 0, \tag{2.1}$$

$$\nabla \times \boldsymbol{E} = -\frac{\partial \boldsymbol{B}}{\partial t}, \tag{2.2}$$

$$\nabla \cdot \boldsymbol{B} = 0, \tag{2.3}$$

$$\nabla \times \boldsymbol{B} = \mu_0 \epsilon_0 \frac{\partial \boldsymbol{E}}{\partial t}, \tag{2.4}$$

where μ_0 is the permeability in free space; $\mu_0 \approx 1.256 \times 10^{-6}$ H/m, ϵ_0 is the permitivity in free space; $\epsilon_0 \approx 8.854 \times 10^{-12}$ F/m.

From Eqs. 2.1, 2.2, and 2.4, we have the equation which governs the propagation of the electric field $\boldsymbol{E}$ in a medium with no charges and no currents:

$$\nabla^2 \boldsymbol{E} - \frac{1}{c^2} \frac{\partial^2}{\partial t^2} \boldsymbol{E} = 0, \tag{2.5}$$

μ_0 and ϵ_0 are related to the speed of light in vacuum c as $c^2 = 1/\mu_0\epsilon_0$.

2.3.2 Paraxial (Gauss) approximation

The *paraxial approximation* means that the optical rays are confined around the optical axis [31]. We assume this approximation for a laser beam due to the laser properties described in Sec. 2.2.3. Since the transverse distances are smaller than the longitudinal distances, the angle θ between the optical axis and the propagation direction of the beam can be approximated as follows

$$\sin\theta \simeq \tan\theta \simeq \theta. \tag{2.6}$$

The partial differential Eq. 2.5 can be solved by separation of variables, by separating the electric field in space and time. Assuming that the electric field propagates in the z direction and is linearly polarized in the direction $\boldsymbol{n}$, ($\boldsymbol{n} \perp z$), the electric field can be written as

$$\boldsymbol{E}(x, y, z, t) = U(x, y, z)T(t)\boldsymbol{n}, \tag{2.7}$$

after substituting Eq. 2.7 in Eq. 2.5 and simplifying, we obtain the separation in space ($U(x, y, z)$) and time ($T(t)$):

$$\frac{\nabla^2 U}{U} = \frac{1}{c^2 T}\frac{d^2 T}{dt^2}. \tag{2.8}$$

In Eq. 2.8, both sides should be equal to a constant value, for the subsequent calculations, let $-k^2$ be the constant. Therefore, the left side of Eq. 2.8 becomes the *spatial Helmholtz equation*, and is written as follows

$$\nabla^2 U = -k^2 U. \tag{2.9}$$

A solution of the spatial Helmholtz Eq. 2.9 in the paraxial approximation can be written in the form

$$U(x, y, z) = \psi(x, y, z)e^{-ikz}, \tag{2.10}$$

where ψ is the complex amplitude of the electric field $\boldsymbol{E}$, ψ modulates the sinusoidal exponential factor.

Replacing Eq. 2.10 in Eq. 2.9 and applying the corresponding spatial derivatives, we obtain

$$\nabla_\perp^2 \psi - 2ik\frac{\partial \psi}{\partial z} = 0, \tag{2.11}$$

where $\nabla_\perp^2 = \left(\frac{\partial^2}{\partial x^2} + \frac{\partial^2}{\partial y^2}\right)$ is the transverse part of the Laplacian. Eq. 2.11 is the *paraxial Helmholtz equation* [31].

2.3.3 Propagation of Gaussian beams

Transforming the transverse Laplacian in cylindrical coordinates, Eq. 2.11 can be written

$$\frac{1}{r}\frac{\partial}{\partial r}\left(\frac{1}{r}\frac{\partial \psi}{\partial r}\right) - 2ik\frac{\partial \psi}{\partial z} = 0, \tag{2.12}$$

a solution to the paraxial Helmholtz equation in cylindrical coordinates represents the complex part of a Gaussian shape of the form:

$$\psi(r) = e^{-i\left[p(z)+\frac{kr^2}{2q(z)}\right]}, \tag{2.13}$$

by now, the phase parameters of the ansatz are unknown, however, the idea is to find conditions on $p(z)$ and $q(z)$ such that Eq. 2.13 is a solution of Eq. 2.11. Replacing Eq. 2.13 in Eq. 2.12, we obtain several important parameters which define the Gaussian beam propagation. One is the *complex parameter* (q(z)), whose inverse is separated into real and imaginary part as

$$\frac{1}{q(z)} = \frac{1}{R(z)} - i\frac{\lambda}{\pi w^2(z)}. \tag{2.14}$$

From Eq. 2.14 two more concepts in Gaussian optics arise; the *radius of curvature* (R(z)) of the wavefronts and the *beam radius at the propagation position* z (w(z)), both describing the propagation of the fundamental Gaussian beam, also called *transverse electromagnetic mode* (TEM) in its lowest order mode; TEM_{00} [18]. The radius of curvature $R(z)$ as a function of z is

$$R(z) = z\left(1 + \frac{Z_R^2}{z^2}\right) = z\left[1 + \left(\frac{\pi w_0^2}{\lambda z}\right)^2\right], \tag{2.15}$$

and the laser beam radius $w(z)$ as a function of z is

$$w^2(z) = w_0^2\left(1 + \frac{z^2}{Z_R^2}\right) = w_0^2\left[1 + \left(\frac{\lambda z}{\pi w_0^2}\right)^2\right]. \tag{2.16}$$

Since the proposed solution is a Gaussian shape for the intensity distribution of the beam, the amplitude is reduced by $1/e$ when $r = r_0 = \sqrt{\frac{2Z_R}{k}}$, which can be named as the *beam waist radius at* $z = 0$ (w_0): $r_0 = w_0$, and k as the wave number, related to the wavelength as $k = 2\pi/\lambda$ therefore,

$$Z_R = \frac{\pi w_0^2}{\lambda}. \tag{2.17}$$

The definition found in Eq. 2.17 is very relevant in Gaussian optics for understanding the propagation of a Gaussian beam. This quantity is called the *Rayleigh length* (Z_R), and defines the length over which the beam keeps confined in a very thin region while propagating in z direction. Due to the symmetry in both sides of the beam along z, $2Z_R$ is considered to be the length at which the laser beam remains collimated and is called depth of focus (DoF).

The function $w(z)$ in Eq. 2.16 is an hyperbolic function, its asymptotes form a half angle θ with the optical axis z, defined as

$$\tan\theta = \lim_{z\to\infty} \frac{w(z)}{z} = \frac{\lambda}{\pi w_0} \Longrightarrow \theta = \frac{\lambda}{\pi w_0}, \tag{2.18}$$

therefore, by using the paraxial approximation defined in Eq. 2.6, we have the definition of the half divergence angle θ of a Gaussian beam propagating in free space (Eq. 2.18).

By replacing $1/q(z)$ from Eq. 2.14 in the second exponential of Eq. 2.13, and using the definition found in Eq. 2.16 for $w(z)$, we obtain

$$\exp\left(-i\frac{kr^2}{2q(z)}\right) = \exp\left(-i\frac{kr^2}{2R(z)}\right)\exp\left(\frac{r^2}{w_z^2}\right). \tag{2.19}$$

Knowing q from Eq. 2.14, and integrating, the first phase of Eq. 2.13 is:

$$e^{-ip(z)} = \frac{1}{1 - i\frac{z}{Z_R}} = \frac{e^{i\tan^{-1}\left(\frac{z}{Z_R}\right)}}{\sqrt{1+\frac{z^2}{Z_R^2}}}, \tag{2.20}$$

where the trigonometric identity $e^{i\tan^{-1}(x)} = \frac{1+ix}{\sqrt{1+x^2}}$ was applied.

By looking at the phase of the paraxial approximation in Eq. 2.10, we can add the phases found for Eq. 2.13 in Eqs. 2.19 and 2.20. Therefore, the total phase of the Gaussian beam is:

$$\phi = kz + \frac{kr^2}{2R(z)} - \tan^{-1}\left(\frac{z}{Z_R}\right), \tag{2.21}$$

where $\varphi = -\tan^{-1}\left(\frac{z}{Z_R}\right)$ is called the Gouy phase. The amplitude is defined by the real part in Eq. 2.19, and the real part in Eq. 2.20. Hence, The electric field of the Gaussian beam can be written as

$$E(x,y,z) = \frac{w_0}{w(z)}\exp\left(-\frac{r^2}{w^2(z)}\right)\exp\left(-i\left(kz + \frac{kr^2}{2R(z)} - \varphi\right)\right). \tag{2.22}$$

2.3.4 Higher-order modes

Also called transverse or spatial modes, the higher-order modes are solutions of the spatial Helmholtz equation (Eq. 2.9). Such solutions are, for instance, the Hermite-Gaussian beams or the Laguerre-Gaussian beams [18]. Most of the existing laser beams can be modelled with one of those higher-order modes (including the pure Gaussian: transverse electromagnetic mode TEM_{00}) or superpositions of them.

Hermite-Gaussian beams

The Hermite-Gaussian beams can be written as the product of a Hermite polynomial with a Gaussian function, their symmetry is rectangular, so their electric field can be written in Cartesian coordinates:

$$E_{n,m}(x,y,z) = \frac{w_0}{w(z)} e^{\left(-\frac{r^2}{w^2(z)}\right)} H_n\left(x\frac{\sqrt{2}}{w(z)}\right) H_m\left(y\frac{\sqrt{2}}{w(z)}\right) e^{-i\left(kz+\frac{kr^2}{2R(z)}-\Phi\right)},$$

where $\Phi = (n+m+1)\varphi$. The variations of the transverse field in directions x and y are represented by the integers n and m, respectively. The Hermite polynomials are:

$$H_n(x) = (-1)^n e^{x^2} \frac{d^n}{dx^n} e^{-\frac{x^2}{2}}.$$

Laguerre-Gaussian beams

The Laguerre-Gaussian beams can be written as the product of a Laguerre polynomial with a Gaussian function, this set is radially symmetric and therefore, their electric field is written in cylindrical coordinates:

$$E_{l,p}(r,\theta,z) = \frac{w_0}{w(z)} e^{\left(-\frac{r^2}{w^2(z)}\right)} \left(\frac{r\sqrt{2}}{w(z)}\right)^{|l|} L_p^{|l|}\left(\frac{2r^2}{w^2(z)}\right) e^{-i\left(kz+\frac{kr^2}{2R(z)}-\Phi\right)} e^{-i\theta l},$$

where $\Phi = (2p+|l|+1)\varphi$, $L_p^{|l|}\left(\frac{2r^2}{w^2(z)}\right)$ are the Laguerre polynomials with argument $\left(\frac{2r^2}{w^2(z)}\right)$. The radial index is represented by p and the helical index is represented by l. These modes carry quantized optical angular momentum $L = hl/2\pi$ per photon [32]. The Laguerre polynomials are:

$$L_p^{|l|}(x) = \frac{x^{-|l|}}{p!} e^x \frac{\partial^p}{\partial x^p}(x^{p+|l|}e^{-x}).$$

An alternative form of the Laguerre-Gaussian beams is visualized when taking the real or the imaginary part of the beam electric field [33]. The normalized intensity distributions of a Gaussian beam TEM_{00}, and some higher-order Hermite and Laguerre beams are visualized in Fig. 2.6. The intensity distributions of the alternative Laguerre-Gaussian modes were calculated by taking the real part of their electric field.

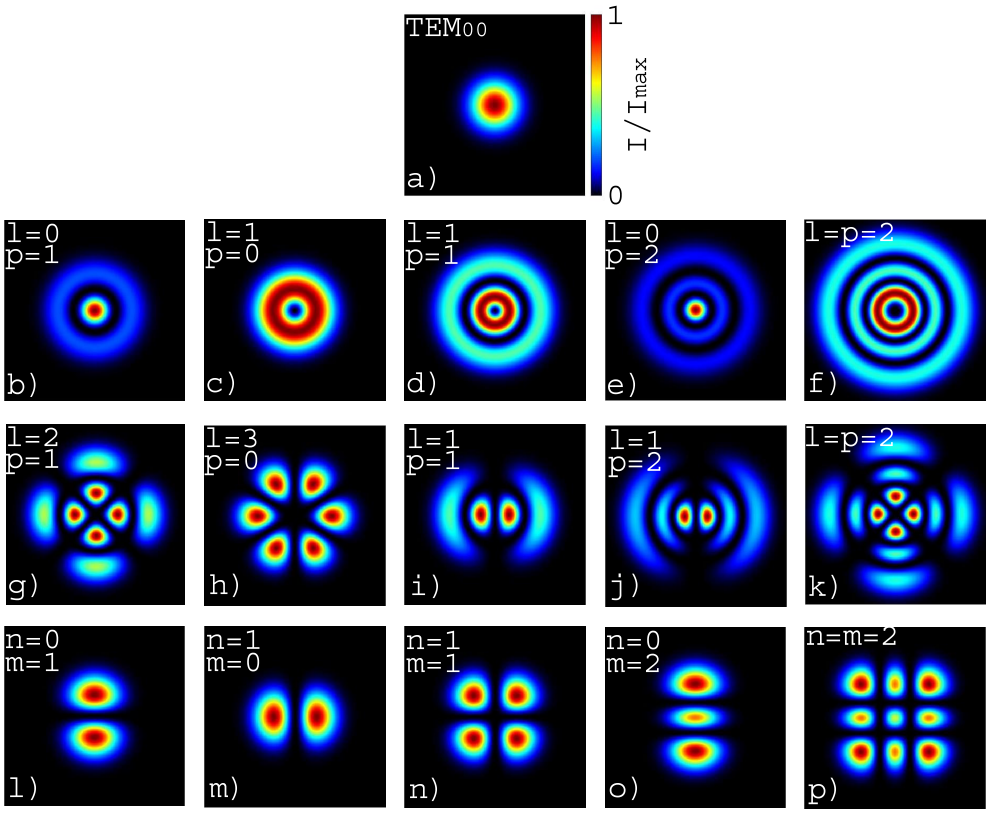

Figure 2.6: Illustration of normalized intensity distributions: Gaussian beam TEM_{00} (a), some higher-order Laguerre-Gaussian modes (b-f), some higher-order alternative Laguerre-Gaussian modes (g-k), and some higher-order Hermite-Gaussian modes (l-p).

Spatial distortions in high-power solid-state lasers

Some high-power solid-state lasers like the Er:YAG possess beam distortions due to several effects, especially thermal effects in the laser rod (typically the active medium of high-power Er:YAG pulsed lasers has cylindrical geometry). These spatial distortions are described as higher-order modes, which can also be combinations of them. Nonuniform pumping in high-power solid-state lasers leads to a nonuniform temperature profile across the laser rod, because the edges of the rod are pumped more than the center. Therefore, the temperature of the rod surface is higher than the temperature of the center, creating

a thermal lens which distorts the beam wavefront. Other thermal effects associated with thermal gradients are stresses caused to the active medium, leading to birefringence, and therefore, distorting the beam too. Moreover, stress fracture occurs when the stress induced by the temperature gradients in the active medium exceeds the tensile strength of the medium. Compared to diode-pumped lasers, in flashlamp-pumped lasers, the thermal effects are more pronounced because additional nonradiative decay processes that do not contribute to the laser output but add heat. Moreover, there is additional heating because there is background absorption of the pump radiation by the host material, and also because of impurity atoms. For instance, some measurements on Nd:YAG lasers revealed that diode pumping produced in the rod crystal one third of the heat produced by flashlamp pumping [21, 34].

Compensation of the thermal effects is challenging because the focal length of the thermal lens and the birefringence level change with pump power. Due to the nonuniform pumping, thermal lens leads to nonspherical aberrations because the focal length at the center of the rod is different than that at the edges of the rod, so the thermally-induced refractive index profile of the rod contains higher order terms. There are mainly two possibilities to correct the nonspherical aberrations. The first approach is dynamic correction by means of phase conjugation with a stimulated Brillouin scattering (SBS) mirror, where the amplified beam is reflected and then passed again through the amplifier to compensate phase distortions. The second approach is static correction by means of an aspheric plate. To compensate thermal birefringence, a Faraday rotator can be placed between the rod and the rear mirror. A broader and deeper description on how to compensate for thermal effects in high-power solid state lasers are found in more detail in [21].

2.3.5 The beam quality factor M^2

A measure of the spatial distortion level is the *beam quality factor* (M^2), it is defined as the variation of a laser beam with respect to an ideal Gaussian beam TEM_{00} of the same wavelength. The closer this factor is to 1, the closer to an ideal Gaussian beam the laser is. The definition of the quality factor is

$$M^2 = \frac{w_{0R}\theta_{0R}}{w_{0G}\theta_{0G}},$$

where w_{0R} is the beam waist radius of the laser of interest, θ_{0R} is the half-divergence angle of the laser of interest, w_{0G} is the beam waist radius of the ideal Gaussian beam, and θ_{0G} is the half-divergence angle of the ideal Gaussian beam. Usually, the comparison is between the laser beam and the ideal Gaussian beam of the same beam waist radius. Since the beam product $w_{0G}\theta_{0G} = \lambda/\pi$ is constant, it is convenient to calculate M^2 as [35]

$$M^2 = \pi\frac{w_{0R}\theta_{0R}}{\lambda}. \tag{2.23}$$

The Rayleigh length for real Gaussian beam ($M^2 > 1$) defined in Eq. 2.17 becomes [19]

$$Z_{Rw_{0R}} = \frac{\pi w_{0R}^2}{M^2 \lambda}. \tag{2.24}$$

From Eqs. 2.23 and 2.24, when the divergence of the beam θ_{0R} is constant, the depth of focus (or $2Z_{Rw_{0R}}$) increases with increasing M^2. In contrast, when the spot radius w_{0R} is constant, the DoF decreases with increasing M^2.

For a laser which resonates in Hermite-Gaussian modes, the beam quality factor can be calculated in each direction as follows [36]

$$M_x^2 = \sum_{n=0}^{\infty}\sum_{m=0}^{\infty}(2n+1)|\tilde{C}_{nm}|^2; \quad M_y^2 = \sum_{n=0}^{\infty}\sum_{m=0}^{\infty}(2m+1)|\tilde{C}_{nm}|^2,$$

where $\tilde{C}_{nm}$ is the weighting factor for the electric fields of the modes contained in the superposition.

For a laser which resonates in Laguerre-Gaussian modes, the beam quality factor M^2 can be calculated as [36]

$$M_r^2 = \sum_{p=0}^{\infty}\sum_{l=-p}^{p}(2p+l+1)|\tilde{C}_{pl}|^2, \tag{2.25}$$

where $\tilde{C}_{pl}$ is the weighting factor for the electric fields of the Laguerre-Gaussian modes contained in the superposition.

Higher-order modes in high-power Er:YAG lasers

Because of the difficulty in finding sensors that capture the light beam of a mid-infrared laser such as the Er:YAG, some authors have devised a way to capture the heat pattern of several Er:YAG lasers at different energies and repetition rates [33]. The patterns were acquired using thermal paper. The distribution of one of the patterns suggests that the beam could be composed of at least two Laguerre-Gaussian beams, for example $\mathrm{LG}_{l=0,p=3}$ and the alternative Laguerre-Gaussian beam $\mathrm{LG}_{l=1,p=3}$. However, the suggested superposition might not be the only one that approximately resembles the shape of the real beam. For instance, the authors of the study [33] suggested that the pattern resembles the alternative $\mathrm{LG}_{l=1,p=3}$ only. The weighting of each mode can also vary, for illustrative purposes, we used equal contributions from each of the modes.

The two beam intensity distributions suggested, their combination, and the real pattern are shown in Fig. 2.7.

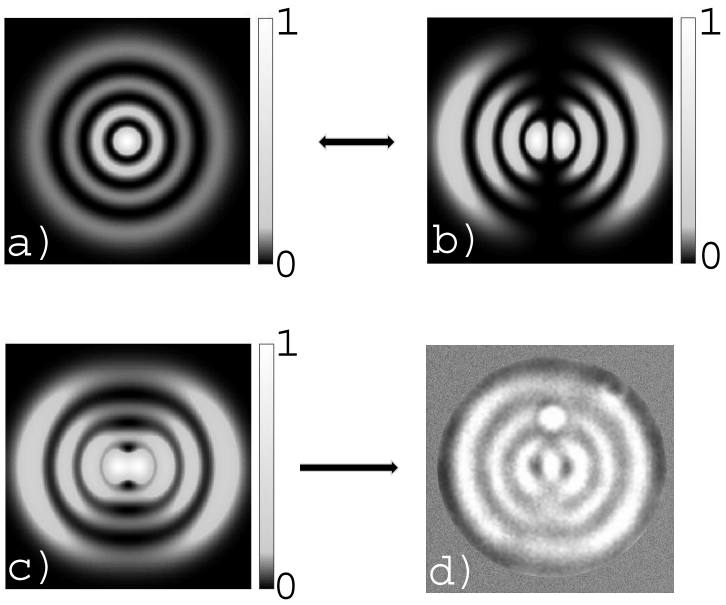

Figure 2.7: Illustration of normalized intensity distributions corresponding to the Laguerre-Gaussian mode $LG_{l=0,p=3}$ (a), the alternative Laguerre-Gaussian mode $LG_{l=1,p=3}$ (b), the superposition of the last two (c), and the real pattern of an Er:YAG laser obtained in thermal paper (d). Image in panel (d) is adapted and reprinted with permission from [33].

Following the superposition of the modes $\mathrm{LG}_{l=0,p=3}$ and the alternative Laguerre-Gaussian beam $\mathrm{LG}_{l=1,p=3}$, the beam quality factor M^2 can be estimated with Eq. 2.25, obtaining $\mathrm{M}^2 = 15$, which is reasonable for a high-power Er:YAG laser.

2.3.6 Finding M^2 experimentally

By measuring the size of the beam at several positions along its propagation axis z (see Fig. 2.8(a)), the beam radius $w(z)$ in Eq. 2.16 can be fitted by an Hyperbolic function as observed in Fig. 2.8(b).

The fitting hyperbolic function possess the general form

$$Az^2 - Cy^2 + Dz + Ey + F = 0,$$

whose intersection point is $K = \left(\frac{-D}{2A}, \frac{E}{2C}\right)$. Centering the hyperbola in the z axis, then $E = 0$, therefore, $K = \left(\frac{-D}{2A}, 0\right)$ and the hyperbolic function can be written as

$$y^2 = \frac{A}{C}z^2 + \frac{D}{C}z + \frac{F}{C},$$

from which the beam size propagation $y = d(z) \equiv 2w(z)$ in z-direction can be written as

$$d(z) = \sqrt{a + bz + cz^2}, \tag{2.26}$$

where the following substitutions were done: $c = A/C$, $b = D/C$, and $a = F/C$.

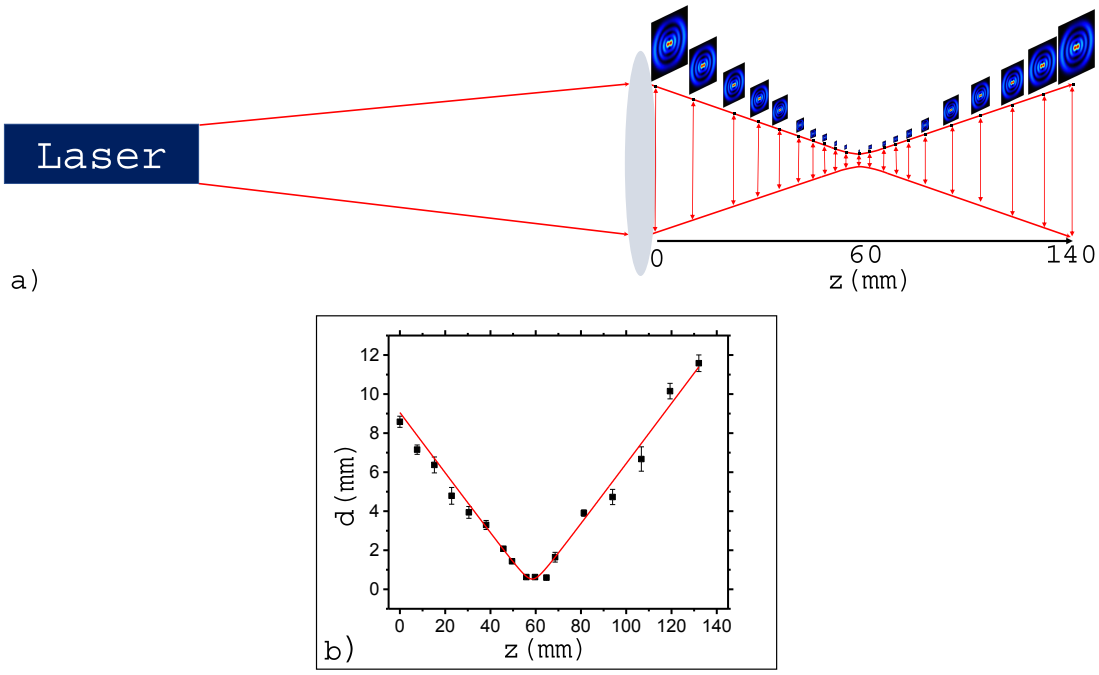

Figure 2.8: Illustration of the method to determine the quality factor M^2 of a beam. Measuring the size of the beam at several positions using a focusing lens (a), and fitting the size to an hyperbolic function (b).

The hyperbola's beam waist is located at the intersection point K in its horizontal axis z, therefore,

$$z_0 = -\frac{b}{2c}, \tag{2.27}$$

is the position where the minimum beam radius is located in z-direction.

The beam waist (minimum beam diameter) is given by its position in z-direction by replacing Eq. 2.27 in Eq. 2.26:

$$d_0 = \frac{1}{2\sqrt{c}}\sqrt{4ac - b^2}, \tag{2.28}$$

from Eq. 2.23, and replacing $w_0 = d_0/2$ from Eq. 2.28, we obtain

$$M^2 = \frac{\pi}{8\lambda}\sqrt{4ac - b^2}, \tag{2.29}$$

from Eq. 2.17 and Eq. 2.28 as well, we get the fitting parameters for the Rayleigh length Z_R:

$$Z_R = \frac{1}{2c}\sqrt{4ac - b^2}, \tag{2.30}$$

finally, we can also find the fitting parameters for full beam divergence angle $\Theta = 2\theta$ from Eqs. 2.17, 2.18, 2.28, and 2.30:

$$\Theta = \frac{2w_0}{Z_R} = \sqrt{c}. \tag{2.31}$$

A more detailed explanation on the procedure for measuring the beam size at several z positions and the fitting can be found in [35].

2.4 Basics of fiber optics

Nowadays, fiber optics has become the center of several technologies, for instance, optical fibers are widely used in communication systems, allowing the transmission of information in a fast and low-cost way [37]. Fiber-optic communication systems began in 1975, this first generation was operated with *gallium arsenide* (GaAs) semiconductor lasers at a wavelength near 0.8 μm. The creation of optical fibers meant an enormous leap in the transmission of information for communication systems. More specifically, the bit rate-distance product BL, where B is the bit rate and L is the repeater spacing; the distance at which the fiber needs a repeater device to regenerate the optical signal. The BL product increased by a factor of 10^{18} in the past 180 years since the creation of the telegraph [38]. In other fields, such as medicine, the use of fiber optics is at the core of endoscopic surgical tools for minimally invasive procedures. In medicine, optical fibers are used to carry light from the source to the patient, providing a more flexible and less invasive surgery. In contrast to communication systems, fiber distances of several kilometers are usually not necessary in medicine. The light source can be installed inside the endoscopic device or outside near the patient. Therefore, the BL product is negligible.

An optical fiber is a waveguide structure that has the ability to deliver light from one place to carry light from one place to another through a flexible path. The main components of an optical fiber are: a dielectric cylindrical central core through which light is mainly transmitted, and its cladding, a dielectric material with lower refractive index. The most commonly used optical fiber is the step index fiber, whose core refractive index remains constant along the fiber length [39].

In the following lines, we will describe the basics and the most relevant concepts of fiber optics in medicine, especially the delivery of laser light for endoscopic laser surgeries.

2.4.1 Total internal reflection

When light travels from one medium to another, the velocity of the wave changes, resulting in refraction of light, which is due to the different refractive index of the materials. The relationship between the refractive index of the incident n_1 and the refracted n_2 rays is known as the *Snell's law* [31]:

$$n_1 \sin\theta_i = n_2 \sin\theta_{ra}, \tag{2.32}$$

where θ_i is the incident ray angle, and θ_{ra} is the refracted ray angle.

In 1841, Daniel Colladon first demonstrated that light was guided in a jet of water falling from a tank, Colladon is considered the pioneer of fiber optics [40]. When light is coupled to an optical fiber, propagation through the fiber is made possible by the difference in refractive index of the core and cladding. In an optical fiber, a light ray travels from a medium with higher refractive index n_1 to a medium with lower refractive index n_2, there is an incident angle called the critical angle θ_C, at which the refracted ray reaches 90°. Since $\theta_{ra} = 90°$, from the Snell's law Eq. 2.32, the critical angle is $\theta_C = \sin^{-1}\left(\frac{n2}{n1}\right)$. At higher angles of incidence, there is no refracted ray, and the light only undergoes reflection within the medium. Therefore, light undergoes *total internal reflection*, all light rays entering the medium at $\theta_T > \theta_C$ face the same phenomenon, see Figure 2.9.

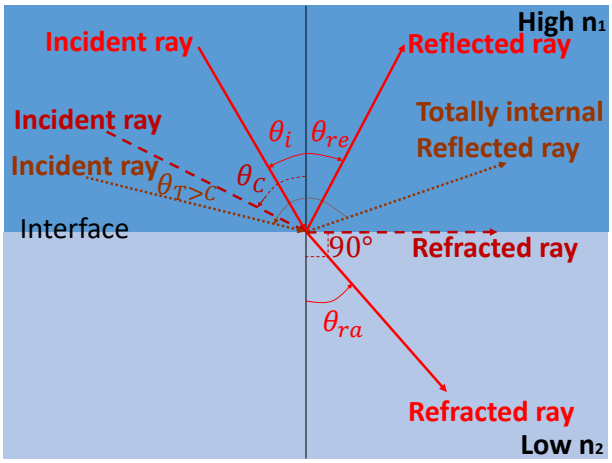

Figure 2.9: Schematic representing Snell's law and the total internal reflection phenomenon.

Since the shape of the fiber is cylindrical, when the ray reaches the second interface

once again, it experiences total internal reflection again. Multiple internal reflection is the way light propagates through an optical fiber.

2.4.2 Types of optical fibers

The most common fibers are glass-based, for instance the silica fiber, which is transparent in part of the visible and in the near infrared region; 600 - 1600 nm, except in 1400 nm. Its highest transmission is at 850 nm, 1300 nm, and 1550 nm; the *telecom wavelengths*. Some silica fibers are also used in the UV region. Plastic fibers operate primarily in the visible region. Other non-silica fibers are made to operate in the infrared region [37]. Figure 2.10 shows examples of the refractive index distribution of the most common fibers. In general, optical fibers are classified in three groups. The step-index multimode fibers, the core size is very large compared to the cladding size. The graded-index multimode fibers have a special distribution of refractive index in the core, being maximum only along the axial direction, their core size occupies around half of the total size of the fiber. The multimode fibers are capable of transmitting several modes, these fibers have usually large core sizes of more than 50 μm up to 600 μm. When the optical fiber core size is much larger than the wavelength of the light, a geometrical optics approach based on using light rays can explain how light travels along the fiber [22]. This is always the case for multimode fibers. The step-index single-mode fiber supports only one mode, and the result is obtaining a very nice and clean Gaussian TEM_{00} beam at the output. However, the coupling of the light becomes harder, because the core size is too small, typically 8-12 μm in diameter.

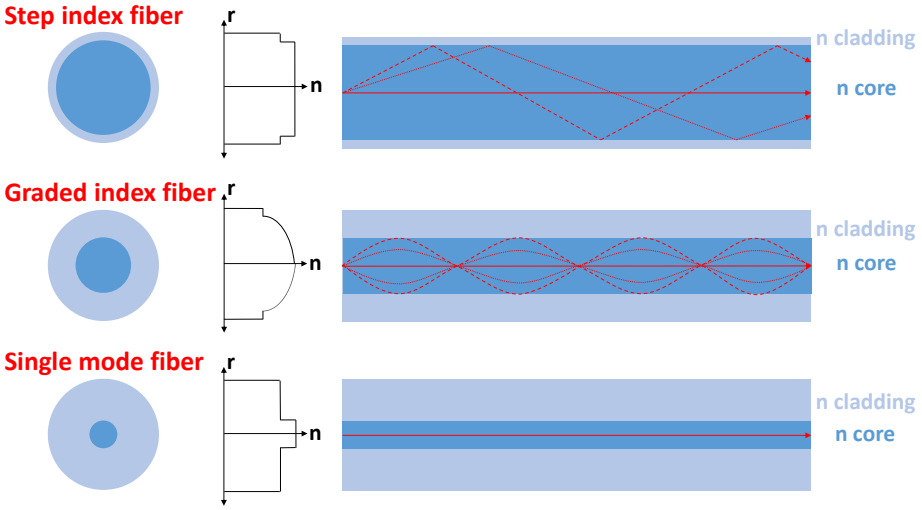

Figure 2.10: Drawing of the most common optical fibers.

2.4.3 Numerical aperture

The *numerical aperture* (NA) is a measure which specifies the acceptance angle of the fiber for collecting the light. The NA is the sine of the acceptance angle. Once the light is coupled into the fiber, it must be reflected from the cladding at an angle $\theta_i > \theta_C$. Since the light is entering the fiber core from another medium (usually the air; n = 1), there is a limit to the entrance angle to the core, such that light propagates through the fiber fulfilling total internal reflection. All the light rays that do not lie within the maximum acceptance angle will strike the cladding at a less angle than the critical angle. Therefore, those rays will be refracted into the cladding and be lost. The numerical aperture of a fiber is defined by its core and cladding refractive index at the wavelength of interest [39]: $\mathrm{NA} = \sin\theta_a = \sqrt{n_2^2 - n_1^2}$. To match the acceptance angle of the fiber θ_a with the input beam, the divergence angle of the beam (Eq. 2.18) must be $\theta \leq \theta_a$.

2.4.4 Losses in optical fibers

An optical fiber may not transmit 100 % of the input power due to several reasons. Some of the most relevant are the following [37]:

Attenuation

The attenuation is the rate at which the signal intensity decreases. Signal attenuation is defined in terms of a logarithmic power ratio measured in *decibels* (dB):

$$Attenuation[dB] \equiv -10 \log \frac{P_{out}}{P_{in}}, \tag{2.33}$$

where P_{in} and P_{out} are the input and output optical powers, respectively. Since the attenuation is measured over distance, the commercial unit of measure used for attenuation is dB/m or dB/km. The attenuation is an exponential loss of power and it is directly proportional to the length of the fiber. The output power drops by half for every incremental length of the fiber; the fiber absorbs energy at an exponential rate. Usually glass fibers have low attenuation at 0.85, 1.3, and 1.55 μm; as low as 2-3.2 dB/km, 0.3-0.9 dB/km, and 0.15-0.6 dB/km, respectively. Due to their low attenuation over distance, glass fibers are preferable for long distance systems.

Absorption losses

Mainly during the manufacturing process, a fiber acquires some impurities that absorb the light transmitted through it. The impurities are ionized molecules such as iron, copper, nickel, and water ions (OH^-). The signal attenuation due to water ions occurs mainly at wavelength 850 nm.

Scattering losses

During the fiber production process, the molecular structure along the fiber may also have some imperfections, which scatter the light while traveling through the fiber, this is called *Rayleigh scattering*. The scattered light is dispersed in the cladding and then lost. These irregularities can also happen in the core-cladding boundary, when the light strikes those imperfections, it gets dissipated in the cladding and lost. Scattering at the core-air boundary due to uneven surface can also cause energy loss either at the input or output fiber tip.

Bending losses

An optical fiber can usually be bent without causing losses. However, when the bending radius reaches a radius so small that the incident angle is smaller than the critical angle, there is no total internal reflection anymore and losses occur. The minimum bending radius depends on the fiber's core and cladding material.

Radiation losses

Light can also travel in the cladding of the fiber, leading to losses in the output energy, this happens mostly in fibers whose core/cladding refractive index change is minimal, like graded index multimode and step index single mode fibers. This can also happen when the light is not correctly coupled inside the core and therefore travels through the cladding.

Fresnel reflection losses

The Fresnel reflection occurs at the core-cladding boundary or at the core-air boundary. In the first case, when the light enters the core at lower angles than the critical one, there is a portion of about 4 % of the refracted light that is reflected into the core. The amount is not sufficient to be carried until the output of the fiber, so it represents a loss instead. On the other hand, when two fibers are connected to each other, there is always a small amount of air in between. When the light travels from the core of the first fiber to the core of the second fiber, the boundary core-air produces a Fresnel reflection into the core of the first fiber. This generates a loss at the connection boundary as well.

Chapter 3

Laser ablation of biological tissue

3.1 Lasers in medicine

The spectral range shown in Table 3.1 corresponds to the classification from the ultraviolet to the infrared wavelengths according to the International Commission of Illumination (CIE) [41]. Lasers have been extensively used in medicine for both diagnostics and therapeutics. The laser light used in medicine lies within a subgroup of the ranges shown in Table 3.1; the biophotonics spectral window: 190 nm to 10.6 μm [22].

Table 3.1: Wavelength ranges for various optical spectrum bands. Based on the CIE classification.

Range	Subgroup name	Short names	Wavelength range
Ultraviolet	Near ultraviolet	NUV, UV-C	100 to 280 nm
	Mid ultraviolet	MUV, UV-B	280 to 315 nm
	Far ultraviolet	FUV, UV-A	315 to 400 nm
Visible	-	VIS	360-400 to 760-830 nm
Infrared	Near infrared	NIR, IR-A	780 to 1400 nm (1.4 μm)
	Mid infrared	MIR, IR-B	1.4 to 3 μm
	Far infrared	FIR, IR-C	3 to 1000 μm

Ophthalmology and dentistry were the first fields where lasers were studied shortly after the invention of the laser in 1960 [42–44]. In ophthalmology, the *helium–neon* (He-Ne) laser ($\lambda = 632.8$ nm) was used in confocal laser scanning to make the topography of the optic nerve, in this way, the laser system is capable of detecting glaucoma [45]. Nowadays, the method is similar but the laser used is a diode laser in the near infrared region ($\lambda = 780 - 790$ nm) [46]. When the retina suffers detachment, lasers can be used to

weld the retina to the underlying tissue, the lasers commonly used for this are the Argon ion at wavelengths 488 and 514 nm [47] and the Nd:YAG second harmonic laser ($\lambda = 532$ nm). Diabetic macular edema in the retina is currently treated with a ($\lambda = 810$ nm) diode laser and a diode yellow laser ($\lambda = 577$ nm) [48]. The UV *argon fluoride* (ArF) excimer laser at wavelength $\lambda = 193$ nm is also commonly used for refractive eye surgery to reshape the curvature of the cornea. This type of surgery reduces or cure vision problems such as myopia, hyperopia, presbyopia, and astigmatism [49]. In dentistry, the main clinical applications are caries removal, endodontics, and implantology. The most commonly lasers used in caries removal are the picosecond *neodymium-doped yttrium lithium fluoride* (Nd:YLF) at $\lambda = 1053$ nm [50] and the Er:YAG at $\lambda = 2.94\,\mu$m [51]. In endodontics, removing infections of the root channel is currently performed using the Nd:YAG and the Er:YAG lasers [52–54]. Low-power pulsed diode GaAs laser at $\lambda = 904$ nm is used for pain relief [55]. In dermatology, port wine stains are usually removed by using Ar^+ laser. For tattoo removal, the *carbon dioxide* (CO_2) [56], Ar^+ [57], and Nd:YAG [58] are the most common lasers used. Skin cancer can be treated using Nd:YAG laser [59, 60]. In other medical fields such as gynecology, gastroenterology, and neurosurgery, the CO_2 laser is widely used. In this thesis, the main focus is the use of lasers in orthopaedics, i.e. *laserosteotomy*, a detail description can be found in Section 3.3.

3.2 Laser-tissue interaction

Laser-tissue interaction is presented in two ways; tissue acting on light and light acting on tissue. The first one is used in medicine for diagnostics, the phenomena involved here are: reflection, refraction, scattering, interference, and absorption. On the other hand, light acting on tissue is used in medicine for therapeutics, and the phenomena involved are: photochemical, photothermal, and photomechanical interactions [61]. In this section we first briefly describe the interactions involved in tissue acting on light, and then the interactions regarding light acting on tissue.

3.2.1 Tissue acting on light

When light interacts with tissue, light suffers changes in direction, intensity, velocity, phase, frequency, and polarization. The changed light generally carries important information about the tissue it had interacted with. To acquire and correctly interpret the information, the concept of tissue acting on light can be broken down into several phenomena. Here, the description of the involved phenomena is focused on the light-tissue interaction for providing diagnostics.

Reflection and refraction

There are two types of reflection; the *specular reflection*, when the surface irregularities are small compared to the wavelength of radiation, and the *diffusive reflection*, when the roughness of the reflecting surface is similar or larger than the wavelength of radiation.

When light strikes a tissue surface and is reflected back due to the difference in refractive index between the incidence medium and the tissue, valuable information of the tissue can be acquired. The most primitive use of light reflected to obtain information of a material is the eye. A more technological, an optical microscope, used to observe objects that the eye cannot observe. The microscope can also be used in transmission mode. The refraction always occurs at the interface of two different media. Due to the difference in refractive index of the two media, when the light is transmitted into the second medium, the wave velocity is changed and therefore the wave is deflected, changing its angle of propagation inside the medium.

Scattering

A scattering event is a collision between two particles (photons, electrons, atoms, molecules). When the collision is between a light wave and a medium, scattering occurs due to the presence of non-uniformities (obstacles) in the medium. Reflection (either diffusive or specular) of light from the surface of a medium is a single scattering event. There exist different types of scattering depending on the wave's wavelength and the obstacles size. The most known scattering type is the *Rayleigh scattering*, it is elastic scattering (wavelength does not change) between a light wave and a particle much smaller than the wavelength, i.e. typically within the nanometer scale or less. In Rayleigh scattering, the scattering intensity I_s is inversely proportional to the fourth power of wavelength: $I_s \sim \lambda^{-4}$ [22]. Therefore, Rayleigh scattering in the ultraviolet region of the electromagnetic spectrum is much stronger than in the infrared region. Another example is the Raman scattering, it is an inelastic scattering event because the vibration and rotation states of the molecules change; the energy of the scattering particles change. Usually the molecules of the medium are excited to higher energy states and have higher energy after the scattering event. Therefore the photon energy of the light is reduced, this is called *Stokes shift*. If the molecules are initially excited, the contrary occurs and the event is called *anti-Stokes shift*. A Raman spectrum of the investigated medium can be obtained with the help of a monochromator. The spectrum provides the energy shifts of the material, providing information about the vibrational modes of the molecules. This information can be used to obtain chemical compositions of materials, to differentiate tissue [62], for cancer diagnosis [63], or for tracking thermal changes in tissue like carbonization [64].

Absorption

Absorption is a transfer of energy from the incident wave to the material where the wave is passing through. For light, the photons *absorbed* by the material transform in another energy type, for instance, heat. In optics, a *transparent* medium is the one which is not absorbing energy from the incident wave, and an *opaque* material is the one which is absorbing energy. The concepts of transparent and opaque are relative to the wavelength of the light wave. The result of having light absorbed is that the intensity of the light is reduced as it travels along the medium. The degree of absorption of a medium depends

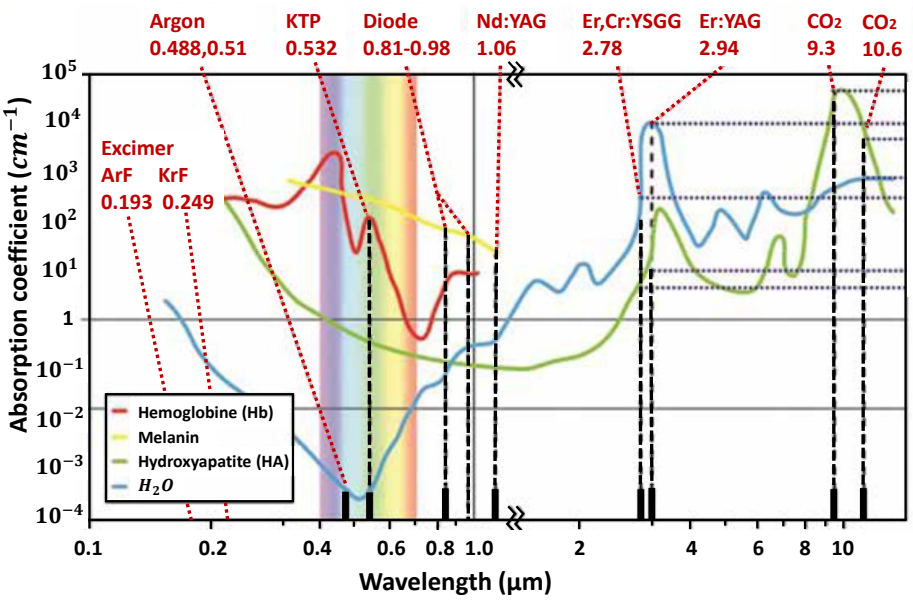

Figure 3.1: Absorption coefficients of several tissue components and some of the existing laser at different wavelengths. Figure adapted and reprinted with permission from [65].

on the electronic constitution of atoms and molecules, concentration of absorbing agents, temperature of the material, thickness of the absorbing layer, and wavelength of the electromagnetic radiation. The *Beer-Lambert's law* describes the attenuation of a light wave after passing through a medium of thickness z:

$$I(z) = I_0 \exp(-\alpha z), \tag{3.1}$$

where $I(z)$ is the intensity of the light after crossing the medium, I_0 is the initial intensity delivered to the medium, and α is the absorption coefficient of the medium at the specific wavelength of the light wave. The inverse of the absorption is known as the *optical penetration depth* $L = 1/\alpha$ if the scattering is neglected. Figure 3.1 shows the absorption coefficient of several biological tissues as water, hemoglobin, melanin, and hydroxyapatite (the main component of bone) as a function of the wavelength.

Examples of medical lasers and their wavelengths are shown in the upper part of the graph. An example of the use of absorption for diagnosis is the pulse oximetry. The arterial oxygen saturation is calculated as the percentage of oxygenated hemoglobin HbO_2 divided by the sum of oxygenated hemoglobin HbO_2 and deoxygenated hemoglobin deoxy-Hb. A pulse oximeter consists of two high-intensity light-emitting diodes (LEDs) working at 660 and 940 nm. The deoxygenated hemoglobin absorbs more at 660 nm and the oxygenated hemoglobin absorbs more at 940 nm, the transmitted light is measured by a silicon photo diode. The device is placed on a finger so the light travels between the finger's nail and the fingerprint side [66].

3.2.2 Light acting on tissue

When light interacts with tissue, not only light suffers changes, tissue can also be affected by the interaction with the light. In this section, the effects of light acting on tissue are discussed, especially from a therapeutics point of view.

The main interactions where light affects tissues are chemical, thermal, and mechanical [61]. Such interactions lead to changing the phase of the tissues, changing their physical properties. In general, the mechanisms are cell killing, heating, coagulation, and ablation.

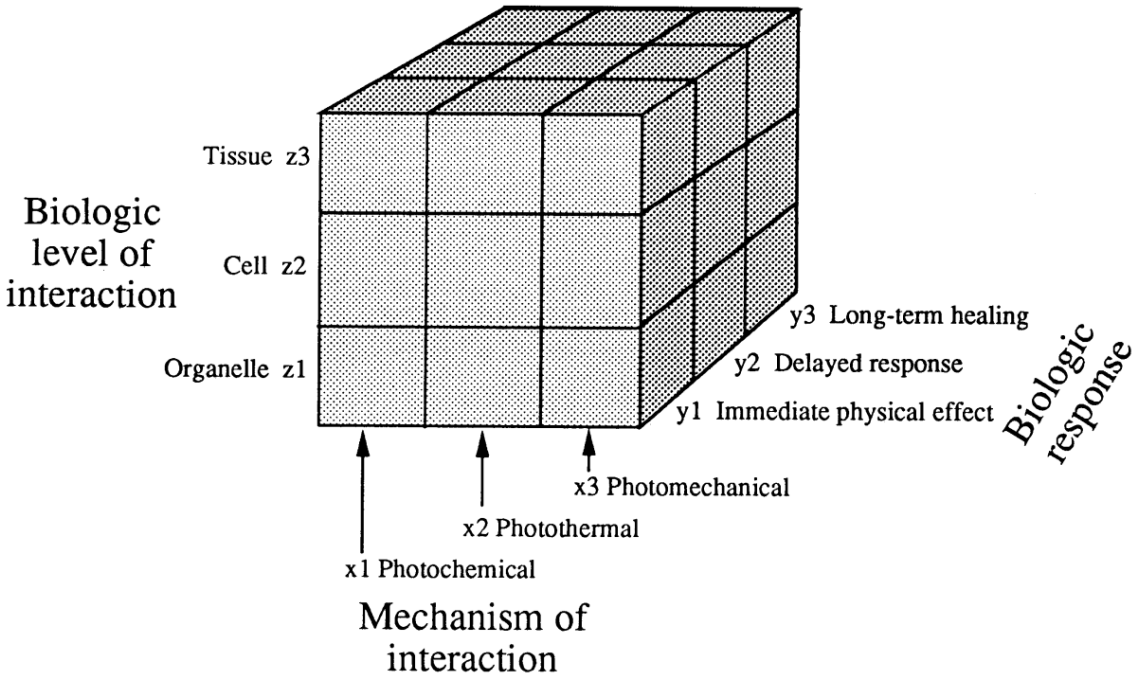

Figure 3.2: Diagram of laser-tissue interactions. In the cube, the mechanisms of interaction are in the axis x, the tissue response in axis y, and the level of biologic structure in axis z. Figure reprinted with permission from [61].

The cube in Fig. 3.2 serves to represent the events that take place when tissue is being irradiated by laser. These interactions can be classified as photochemical (x_1), photothermal (x_2), and photomechanical (x_3). In y axis, the time course of the tissue reaction is represented as immediate physical effect (y_1), delayed response (y_2), and long-term healing (y_3). The tissue structures that can be affected by the interaction with the laser are organelles (z_1), cells (z_2), or tissues (z_3). Since our purpose is investigating laser ablation of bone and how to make it efficient, the laser-tissue interactions will be mainly focused on the immediate physical effects (y_1).

Photochemical interactions

A photochemical interaction is when light can trigger chemical reactions in the molecules of the tissues. The most known application of this type of interaction is the *photodynamic therapy* (PDT), used for treating acne and for destroying cancer cells. In PDT, a photosensitizer is injected into a vein of the patient, it distributes among all soft tissues in the body, except the brain. The photosensitizer is retained longer by the cancer cells, and is activated only by means of light. The most common light sources used are diode lasers, such as the gallium-aluminium-arsenide laser, which produces light in the range 770-850 nm [67]. Once the photosensitizer is activated in the cancer cells, the photosensitizer molecule is excited to the triplet state T^1. There are essentially two types of PDT, the most important one is the type II, where, the energy is transferred to the oxygen molecules directly, then excited oxygen particles (singlet oxygen) are generated, oxidizing the adjacent cancer cells [68].

Photothermal interactions

The photothermal interaction is given when the laser energy is transferred to the tissue in the form of heat, increasing its temperature locally, and undergoing *thermal effects*. The main photothermal interactions are *desiccation* and *thermal injury* [61]. *Desiccation* is the process where the laser energy is removed from the tissue by escaping vapor, i.e. the process of evaporation of water. Here, no thermal injury is created. *Thermal injury* is the irreversible process of thermal denaturation. Coagulation is the immediate damage caused to the tissue, it is a visible thermal effect. While necrosis is the delayed damage observed. These are low-temperature damage processes approximately up to 100 °C, where water vaporization occurs. Tissue ablation by explosive vaporization occurs at higher temperatures, and vaporization of carbon occurs at ca. 3550 °C [61].

Photomechanical interactions

The photomechanical interactions are present when lasers induce stress in the tissues, where the tissues can be deformed or even can break (macroscopic like cracking, or microscopic like microfractures or cellular disruption). Stress is reported in units of pressure, i.e., bars, atmospheres, or pascals: $1\,\text{bar} = 0.987\,\text{atm}$; $1\,\text{bar} = 10^5\,\text{Pa}$. The action of a high-power Er:YAG pulsed laser on hard tissue produces a photomechanical disruption of the hard tissue *extracellular matrix* (ECM) by phase explosion and confined boiling [69]. The concepts and phenomena involved will be discussed in the following sections.

3.3 Ablation of hard tissue with pulsed lasers

Dentistry is the field where hard tissue ablation using lasers have been widely studied and applied in clinics, most of the lasers used in dentistry are the CO_2 laser working at $9.3\,\mu\text{m}$, erbium lasers like Er:YAG at $2.94\,\mu\text{m}$ and the *erbium-chromium-dopped yttrium-scandium-gallium garnet* (Er,Cr:YSGG) at $\lambda = 2.78\,\mu\text{m}$ are used for ablating dentin,

enamel, soft tissue and caries [10–12]. The CO_2 laser is also a good candidate for bone ablation because the absorption coefficient of water at $\lambda = 9.3\,\mu$m is also high compared to other lasers. However, since the ablation mechanism is based on the tissue water phase transitions (this topic will be discussed in Sec. 3.3.2), Er:YAG laser would still work better, additionally, Er:YAG laser is a more compact laser, solid state, easier to handle, and finding appropriate optical fibers is easier than for the CO_2 laser. The *holmium-doped yttrium aluminium garnet* (Ho:YAG) laser working at $2.1\,\mu$m has been also studied in dental tissues, however not yet used in clinics [70]. Other lasers which possess shorter pulse width are also used for hard tissue ablation: Nd:YAG, Nd:YLF, *titanium-doped sapphire* (Ti:Sapphire), and ultrashort pulse lasers.

3.3.1 Bone: properties relevant for laser ablation

The most complex and multicellular animals have four types of tissue in the body, namely *epithelial*, *connective*, *muscle*, and *nervous tissue* [71]. The connective tissue is of our particular interest, since bone is a type of dense connective tissue. Bone is the most resistant tissue to bending and torsion, providing the body protection and support. There are two types of bones, depending on the distribution and orientation of the collagen fibers: lamellar bone (*cortical bone*) and non lamellar (*cancellous bone*). The cortical or compact bone is the outer surface of the bone, is the most dense type of bone, therefore provides protection to the skeleton, the cortical bone is about 80 % of the total mass of the skeleton. The cancellous or trabecular bone, also known as spongy bone is the inner tissue of the bone, it is a porous tissue, it is less dense than the cortical bone, therefore more flexible. Tissue composition, optical, thermal, and mechanical properties, are relevant for laser ablation. Tissue ECM is the structure that provides stability, the most abundant fibrous protein present in the ECM is the collagen, therefore, collagen content is directly correlated to the strength of the tissue ECM. Cortical bone ECM is composed approximately of 27 % collagen, 13 % water, and 60 % mineral in the form of hydroxyapatite crystallites; a compound form of calcium phosphate [72]. Enamel, the external tissue of the teeth is the hardest tissue in the body, 95 to 98 % of it is composed of inorganic material (hydroxyapatite crystallites) [73]. Figure 3.1 shows the absorption coefficient for different tissue components at different wavelengths, corresponding to some existing lasers. The absorption coefficient found for cortical bone at the Er:YAG wavelength $\lambda = 2.94\,\mu$m is $\alpha = 2413\,\mathrm{cm}^{-1}$ [74], and the penetration depth, given by the reciprocal of the absorption coefficient (see Eq. 3.1) is $L \approx 4\,\mu$m, which is the characteristic depth of laser energy deposition. Given the composition of cortical bone, its absorption coefficient at the Er:YAG wavelength is probably the highest (therefore the lowest penetration depth) within the spectrum shown in Fig. 3.1, these optical properties suggest very efficient and precise bone ablation achieved by the Er:YAG laser.

The mechanical properties of the tissue strongly strongly the tissue water phase transitions during laser ablation. Figure. 3.3 shows the stress-strain curves for some soft biological tissues. The *ultimate tensile strength* (UTS) is the maximum stress that tissue

can withstand while being elongated or compressed before it brakes. In Fig. 3.3, the dot symbol represents the UTS of the biological tissues shown, including that of cortical bone [75]. The response of the tissues is mainly nonlinear and possess a concave shape. The strain rates at which the tissues are loaded to acquire the curves in the figure are very low; about the order of $10^{-3}\mathrm{s}^{-1}$. However studies at rapid deformation: strain rates in the range 0.3-170 s^{-1} have shown that the UTS increases in proportion to the logarithm of the strain rate [76–78]. According to the UTS data found in these studies, it is very likely that at higher strain rates, like the ones produced during pulsed laser ablation (10^5-$10^7\,\mathrm{s}^{-1}$) the tissue UTS increases even further compared to the quasi-static loading conditions [69].

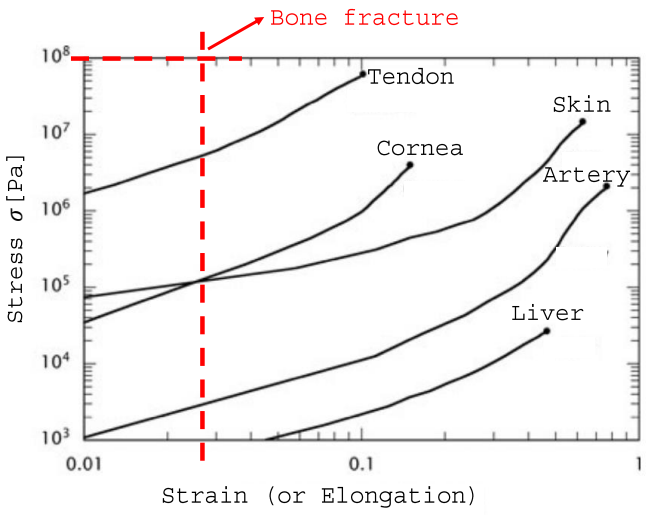

Figure 3.3: Stress-strain (elongation) curves of some soft tissues, and their UTS marked with dot symbol. The bone UTS reported as 148 MPa (1.48×10^8 Pa) at elongation 0.028 [75] is also marked in the diagram. Figure adapted and reprinted with permission from [69].

Some tissues like liver have a very weak ECM due to the low collagen content of ca. 8 % [79], while the UTS of bone is very high compared to soft tissues because its ECM is stronger, it has a large amount of collagen (ca. 27 %), which is similar for skin (collagen content: 25-33 %). When the laser interacts with the tissue, enough pressure should be generated until reaching the UTS of the tissue to be able to brake it. The phase transitions under laser action that tissues with strong ECM undergo are different than those with weaker ECM [69].

3.3.2 Phase transitions during laser ablation

In principle, an ablation process gives rise to the fracture of chemical bonds in the material, which produces the removal of molecules, molecular fragments, and molecular

clusters. The fracture of chemical bonds during laser ablation produces formation of voids, which are bubbles or cracks that allow the removal of the material in fragments. The phase transitions involved in vaporization, molecular fragmentation, and void formation processes can be explained by photochemical, photothermal, and photomechanical mechanisms. Nevertheless, we focus our study in photothermal and photomechanical mechanisms to explain the laser ablation process of biological tissues, especially cortical bone. The laser ablation mechanism in biological tissues is governed by the phase transitions of the tissue water and their modification in the presence of the ECM. The diagram of pressure vs. temperature (p-T) in Fig. 3.4 shows a projection of the phase diagram in liquid and gaseous water. The point A is called the *triple point*, where the solid, liquid and vapor phases coexist in thermodynamic equilibrium. Point C is called the *critical point*, it is the temperature and pressure at which there is no thermodynamic distinction between liquid and gas. Along curve A-C the liquid and vapor phases are in equilibrium with each other, this curve is named the *binodal*. Along the curve B-C (called the *spinodal*) the liquid is superheated, which means that the liquid is above its boiling temperature (point 2 in the phase diagram) without vaporization, the states along this curve are unstable. Point 1 in the phase diagram represents the liquid at temperature below its vaporization point; for instance water at atmospheric pressure (1 atm) below 100 ° (point 2). *Surface vaporization* is the equilibrium vaporization at the liquid-vapor interface, this occurs at any point in the curve A-C. During laser ablation, the vapor formation rates are usually higher than the rate of equilibrium vaporization, therefore, the removal process becomes volumetric, providing efficient ablation. *Normal boiling* is a volumetric process where the vapor formation depends on the presence of nuclei of vapor within the liquid. These nuclei trigger the nucleation and growth of vapor bubbles, producing partial vaporization of a liquid volume. The vapor-liquid layer where the transition between saturated liquid and saturated vapor occurs has a thickness that is comparable to the optical penetration depth L of the incident laser light. Normal boiling is unlikely to happen in pulsed laser ablation of tissue, because the presence of the extracellular matrix inhibits the mobility of the vapor bubbles [69]. Nevertheless, the presence of the ECM modifies the phase transition occurring during laser ablation, which will be explained in Sec. 3.3.3.

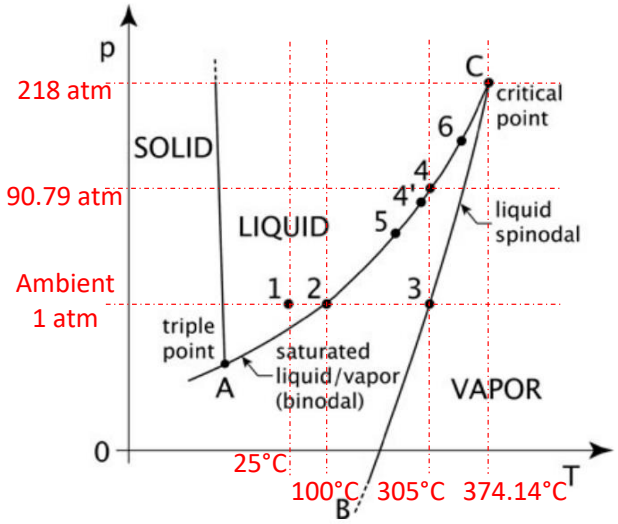

Figure 3.4: Projection pressure vs. temperature of the thermodynamic phase diagram. The points represent some states of interest for the current study: (1) the liquid at ambient temperature and pressure, as an example, water at ambient conditions, i.e., pressure 1 atm and temperature 25° C, its boiling temperature at ambient pressure is 100° C, located at point (2), (3) spinodal temperature at ambient pressure; 305° C for water, (4) saturated pressure (90.97 atm for water) at ambient spinodal temperature, and the critical point for water is achieved at 374.14° C and 218 atm. Points (4') and (5) will be explained in Sec. 3.3.3. Figure adapted and reprinted with permission from [69].

3.3.3 Photomechanical ablation by phase explosion and confined boiling

Phase explosion

When the rate at which the volumetric laser energy is deposited in the tissue is higher than the rate at which this energy is consumed by vaporization and normal boiling, the tissue water goes from point 1 to 2 (see Fig. 3.4), and its temperature continues growing in the region between 2 and 3, where it is in a metastable superheated state. Once it reaches point 3, the liquid is in an unstable state and spontaneously relaxes towards equilibrium (a state in the binodal A-C), this process is known as *spinodal decomposition*. In spinodal decomposition, the liquid separates into an equilibrium state where the saturated liquid phase is mixed with the saturated vapor phase, this separation process involves a high pressure rise via an isovolumetric transition from point 3 to point 4' in Fig. 3.4. Here, vapor bubble formation (nucleation) occurs too, it has been proved that there is a strong dependence on the nucleation rate and the increase of the superheat temperature in the liquid while it undergoes spinodal decomposition. Therefore, spinodal decomposition is accompanied by bubble nucleation and this combined phase transition process is called *phase explosion* [69, 80].

Confined boiling

In the presence of ECM, in addition to the surface tension, the vapor pressure needed to start bubble nucleation has to overcome the elasticity of the ECM as well [81], meaning that the pressure needed for bubble growth in tissue is much higher than in liquids. Therefore, the boiling temperature also increases. The process in which the vapor pressure (and temperature) increases until exceeding the ultimate tensile strength (UTS) of the tissue is called *confined boiling*. When this occurs, the tissue undergoes explosive ablation. In Fig. 3.4, the explosive tissue ablation by confined boiling corresponds to the path 1-2-6, the path 2-6 coincides with the binodal, assuming that point 6 is the UTS of the tissue, the process terminates there. When the tissue possess a weak ECM, e.g., liver, the ablation enthalpy (energy needed to ablate the tissue) is often smaller than the vaporization enthalpy (energy needed to reach the boiling temperature) of water. Nevertheless, for stronger tissues, e.g., skin, temperature as high as 700 °C are required to start ablation, so the ablation enthalpy is typically higher than the vaporization enthalpy of water. This phenomena occurs in both continuous and pulsed laser irradiation [69,82,83].

There are mainly three reasons why some tissues with strong ECM require several hundreds of degrees and therefore several tenths of megapascals to be ejected during pulsed laser ablation. First, as discussed in Sec. 3.3.1, the ultimate tensile strength of the tissue increases in proportion to the logarithm of the strain rate, which suggests much higher UTS for tissues while being hit by a pulsed laser. Second, when the thermal energy overcomes the weak hydrogen bonds and the van der Waals interactions that stabilizes the helical configuration of the three α-chains in the collagen molecule, thermal denaturation occurs. Denaturation of the collagen molecule takes place at 75 °C when heated for several minutes [84]. However, for thermal exposures in the nanosecond or microsecond regime, the temperature required to destabilize the collagen molecules greatly exceeds 100°C [85]. Third, since the collagen fibrils are immersed in the surrounding tissue, denaturation occurs first in the covalent bonds that maintain the stability of the collagen molecules, delaying the mechanical failure of the fibrillar tissue, therefore requiring higher temperatures for collagen denaturation [69]. In the case of bone, since it has a stronger ECM, it is expected that the temperature needed to remove the tissue by a pulsed laser is higher than that for skin, i.e., higher than 700°C. The temperatures and pressures associated to bone ablation with pulsed laser have not been reported yet.

The volumetric energy deposition rate is defined as $S = \alpha\Phi/t_p$, where α is the material's absorption coefficient, Φ the laser fluence, and t_p the laser pulse duration. For very low volumetric energy deposition rates and a high density of bubble formation, the laser energy heats the tissue under equilibrium conditions at constant pressure from point 1 to 2 in Fig. 3.4, then it continues on the binodal until reaching the UTS of the tissue, where explosive material removal occurs. For pulsed laser ablation and/or small density of bubble formation, the tissue water undergoes a transition to a metastable state following the path 1-2-3, once the spinodal limit 3 is reached, the phase explosion starts by going to point 4' and then goes to point 5. Here, the upcoming phenomena depends on the

mechanical properties of the tissue ECM. If the ECM is weak, immediate tissue ejection will happen. For a stronger tissue ECM, the material ejection is not driven by the phase explosion only, the tissue will undergo confined boiling by following the path 5-6 where 6 is the UTS of the tissue. Hence, when the tissue ECM is strong enough, as in the case of skin and bone, the tissue ejection with a pulsed laser is driven by the combination of a phase explosion finalizing with confined boiling until reaching the tissue UTS at point 6 [69].

3.3.4 The effects of laser parameters in photomechanical ablation

The effect of pulse duration

Ideally, to efficiently ablate tissue, two main conditions should be fulfilled: (1) *thermal confinement*, where the temperature is confined within the volume the radiation is absorbed, given by the optical penetration depth L and the beam radius w. (2) *stress confinement*, where the thermoelastic stress wave is confined within the heated volume. When both conditions are fulfilled, the ablation is efficient and does not produce any collateral effects to the adjacent tissues.

The thermal confinement is given when the pulse duration of the laser t_p is shorter than the thermal diffusion time τ_t; $t_p < \tau_t$, defined as [61, 69]:

$$\tau_t = \frac{L^2}{\xi}, \tag{3.2}$$

where ξ is the thermal diffusivity is defined as

$$\xi = \frac{\beta}{\rho c_{hc}}. \tag{3.3}$$

The thermal diffusivity ξ of cortical bone can be calculated with the values of thermal conductivity β, tissue density ρ, and specific heat capacity c_{hc} found in [86]; $\xi = 0.226\,\mathrm{mm}^2/\mathrm{s}$. The absorption coefficient for cortical bone at $\lambda = 2.94\,\mu\mathrm{m}$ is $\alpha = 2413\,\mathrm{cm}^{-1}$ [74]. The thermal relaxation time is $\tau_t = 70.8\,\mu\mathrm{s}$.

The stress confinement is given when the pulse duration t_p is shorter than the characteristic time required for a stress wave to cross the heated volume ($t_p < \tau_m$), this time τ_m is related to the absorption coefficient of the tissue α and the propagation speed of sound in the tissue c_a as

$$\tau_m = \frac{1}{\alpha c_a}, \tag{3.4}$$

the speed of sound in bone is 4080m/s [87], therefore, the stress confinement time for bone at $\lambda = 2.94\,\mu$m is $\tau_m = 1$ ns. Figure 3.5 shows the zones of stress confinement, thermal confinement, and non confinement for optical penetration depth vs. pulse duration.

The typical pulse duration of mid-infrared lasers is in the microseconds regime, meaning that neither the thermal nor the stress confinement in cortical bone can be fulfilled for these lasers. This leads to damage like denaturation, necrosis, carbonization, cracking, etc. Therefore, a proper water cooling system might be used. Since the water cooling might cause reduction of ablation rate because the water absorption is high for mid-infrared lasers, the water cooling system must be optimized to apply the correct amount of water directly to the ablation zone. The influence of water cooling for bone ablation with Er:YAG laser will be discussed in Chapter 4, and an optimization is described in Chapter 5.

Shortening the pulse duration of CO_2 from ms to few μs and Er:YAG from μs to ns showed a reduction in the thermal damage zone of different tissue types [88, 89].

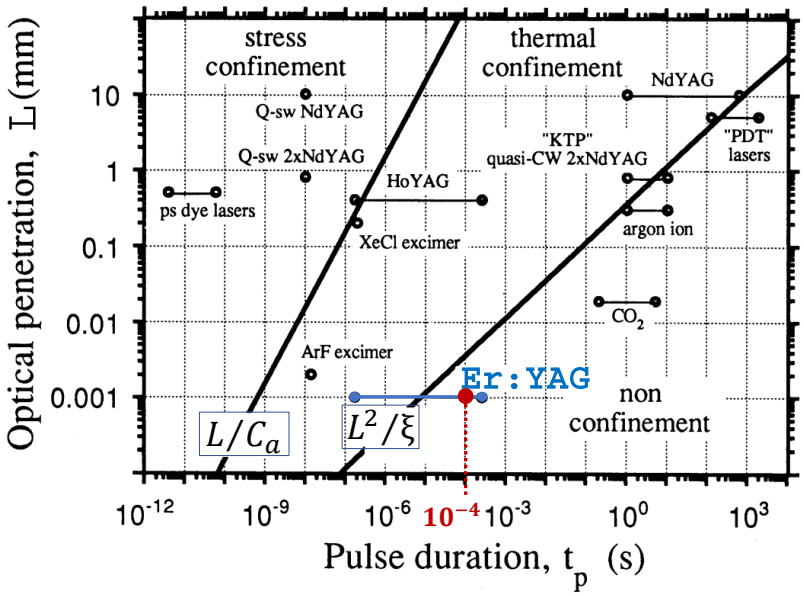

Figure 3.5: Illustration of the laser-tissue parameters to achieve either stress confinement, thermal confinement, or non confinement. The parameters are optical penetration depth L, and the laser pulse duration t_p. A microseconds Er:YAG laser is in the non confinement zone, however, a nanoseconds Er:YAG laser is already in the thermal confinement zone. Figure adapted and reprinted with permission from [61].

The effect of energy and spot size

There are two important parameters to understand the effect of the energy in the ablation process. The pulse energy E_p and the peak power P_{peak}. The two parameters are related to each other by a third parameter, the pulse duration t_p [18]:

$$P_{peak} = \frac{E_p}{t_p}, \tag{3.5}$$

The fourth parameter is the spot size of the laser beam, which determines the peak power density. Together, these four parameters determine the type of interaction the laser light has with the tissue. Most of the lasers used in medicine have a Gaussian distribution (Sec. 2.3.3), their divergence and collimated region depend on the spot size and wavelength. When the spot size is too small, the divergence is high, and therefore, the energy density is reduced too fast (short depth of focus), stopping the ablation process. On the contrary, if the spot size is too large (large depth of focus), the energy density is too low, so an effective ablation is not possible neither.

The energy determines the amount of tissue removed. Usually, the greater the energy, the more tissue removed. However, the relation is not linear.

There are two fundamental models for laser ablation; the *Blow-off model* and the *Steady-state model* [69, 80], in both models, a threshold fluence Φ_{th} is required to start ablation of the material. The *Blow-off model* assumes that the distribution of absorbed energy in the tissue is governed by the Lambert-Beer law $T = \frac{\Phi}{\Phi_i} = e^{-\mu_a l}$, where T is the optical transmission, Φ is the fluence transmitted after the incident fluence Φ_i has traveled through an optical path length l, and μ_a is the absorption coefficient of the material. In this model, material removal starts only after a laser pulse has finished. Additionally, thermal confinement must be fulfilled. These conditions are fulfilled for lasers with pulse durations of $\tau_p = 100\,\text{ns}$ or less. In this model, there is a semi-logarithmic relationship between ablation depth l and the incident energy density Φ_0:

$$l = \frac{1}{\alpha} \ln\left(\frac{\Phi_0}{\Phi_{th}}\right). \tag{3.6}$$

Ablation with lasers in the microsecond regime or longer is usually governed by the *Steady-state model*, where a fixed energy density is required to ablate a unit mass of tissue. Contrary to the previous one, in this model (and given that the threshold radiant exposure of the tissue is deposited), ablation starts right after the laser pulse begins. Well above the threshold, the *Steady-state model* predicts a linear dependence between ablation depth and incident fluence. The model that best describes ablation might change depending on the fluence range of the data set. In this model, there is a linear relationship between ablation depth and the incident energy density:

$$l = \frac{\Phi_0 - \Phi_{th}}{\rho h_{abl}}, \tag{3.7}$$

where the ablation threshold Φ_{th} and the absorption coefficient of the tissue α are related to the ablation enthalpy as $\Phi_{th} = \rho h_{abl}/\alpha$.

The effect of repetition rate

The most efficient ablation of tissue takes place when the ablation is fast and the surrounding tissue is preserved. The faster the laser is pulsed, the faster the ablation is. However, pulsing the laser too fast might lead to thermal damage of the adjacent tissue. It takes around 10 times the thermal relaxation time τ_t for the tissue to reduce its temperature to the initial temperature before ablation started [90–93]. For making decision about the repetition rate R_r, it is more accurate to calculate the thermal diffusion time using the thickness of tissue damage rather than the penetration depth (Eq. 3.2). Thus, $R_r < (10 \cdot \tau_t)^{-1}$, with $\tau_t = D_z^2/\xi$ and D_z the thickness of the damage zone [69].

The effect of beam quality

As described in Sec. 2.3.3, the depth of focus (DoF) of a Gaussian beam is twice the Rayleigh length of the beam. It defines the region along the propagation direction of the beam where the beam is considered to be collimated and its intensity is more concentrated. The smallest spot size located in the middle of the DoF region defines the divergence of the beam. The concepts presented in Sec. 2.3.3 are for an ideal Gaussian beam TEM_{00}, which in practice does not exist. The quality factor M^2 defines how different a beam diverges compared to the ideal TEM_{00}. The collimation length of a real Gaussian beam is reduced M^2 times compared to an ideal one with same wavelength and same waist size, see Eq. 2.24. As the beam divergence and Rayleigh length are affected by the beam quality, also the propagation is affected. As discussed previously, the spot size is of great importance in the ablation processes because it changes the radiant exposure of the beam. As the beam quality reduces when M^2 gets higher, the divergence of the beam increases, therefore, the beam reduces its radiant exposure inside the tissue faster than a beam with better beam quality. Additionally, since the energy is not well distributed (neither flat-top nor TEM_{00} shape), the energy of the laser cannot be well focused into the desired area, leading to a reduction of the ablation efficiency. Given a Gaussian beam with a poor beam quality, the laser loses potential to be used in applications where deep ablation is required. Although the M^2 of Er:YAG laser is typically too high: $15 < M^2 < 30$, Er:YAG laser is proven to be one of the best lasers for bone ablation, even for deep bone ablation, this will be discussed in Sec. 5.

On the other hand, a flat-top (or top-hat) beam would ideally improve the ablation depth due to the constant intensity distribution along the beam. The semi- and flat-top beams can be described by the super-Gaussian function, where the lower order describes the ideal Gaussian beam, and the higher the order the flatter the intensity profile gets. Due to diffraction, the intensity distribution of such beams gets distorted when propagating even a short distance. When the order of the super-Gaussian increases, the

depth of focus decreases [94, 95]. Therefore, such beams are not ideal for deep ablation applications.

The effect of water cooling

Water is the natural coolant during almost any kind of surgery, besides cooling, water provides recuperation of the tissue by re-hydrating it. However, when using infrared lasers, the water used during the surgery will absorb part of the energy of the laser if not controlled properly. This leads to waste of energy, water and time.

The effect of dynamic changes in optical absorption

Optical absorption of tissue has shown to be affected by the temperature increase. Particularly for wavelengths close to the highest absorption peak of water at $3\,\mu$m, like the Er:YAG laser at $\lambda = 2.94\,\mu$m, the absorption coefficient reduces more drastically than the absorption coefficient of water at $\lambda = 2.79\,\mu$m (Er:YSGG laser) [80].

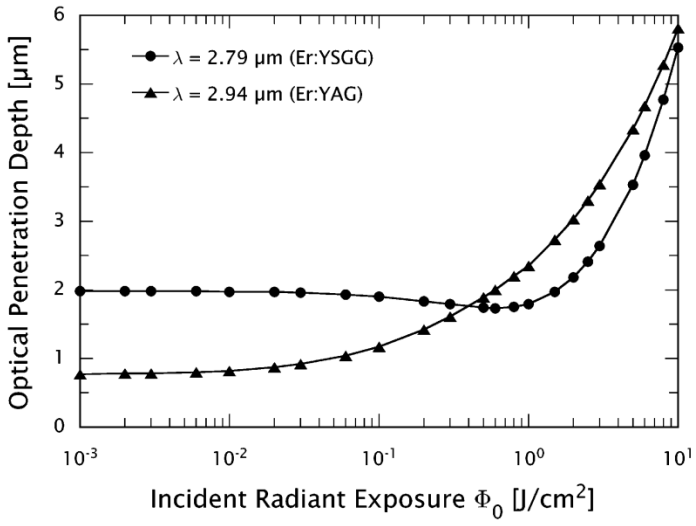

Figure 3.6: Graph showing the dynamic changes of the optical penetration depth for Er:YAG at $\lambda = 2.94\mu m$ and Er:YSGG at $\lambda = 2.79\mu m$ laser irradiation. Image reprinted with permission from [69].

Figure 3.6 shows the effects of the temperature on the penetration depth of water when being exposed to two different wavelengths. The penetration depth becomes higher after $0.5\,\mathrm{J/cm^2}$ for Er:YAG laser, where the absorption coefficient of water drops one order of magnitude when the volumetric energy density increases by two orders of magnitude [69, 80]. The high optical penetration depth observed in Fig. 3.6 can be also understood for soft and hard tissue, although the curves will not appear the same, one can suggest

that when the tissue dehydrates, the effect should be visible in a similar graph. For instance, in hard tissue, when the tissue dehydrates, the ablation rate decreases, and this is because the absorption coefficient changed due to temperature. Again, a proper cooling system can help reducing the temperature effects and therefore, the drastic changes in tissue absorption and penetration depth.

Delivering laser light through mid- and far infrared fibers

Along the history of optical fibers, it has been a challenge to find proper materials for fibers to deliver light of wavelengths above 2 μm, and even harder above 3 μm. Most of the existing fibers are glass-based, they are extensively used due to the low attenuation they have mostly in the visible, near infrared, and in part of the mid-infrared up to approximately 2 μm. On the contrary, in the mid- and far infrared spectrum, glass-based fibers typically have high attenuation. Nevertheless, in the past years, researchers have developed different types of biocompatible fibers suitable for transmitting light in the middle and part of the far infrared region, such as special glass-based, hollow-core, and photonic crystal fibers. In these regions, the fibers are usually step-index multimode glass-based fibers, the core sizes are in the range 250-600 μm [37]. The use of optical fibers in hard tissue ablation and suitable for wavelength regions around 3 μm will be discussed more in detail in Chapter 6.

3.3.5 Photomechanical ablation with short and ultrashort pulse lasers

From the visible to the near-infrared wavelengths, water has low absorption coefficient, meaning that water is mainly transparent at those wavelengths. Although this issue is typically not good for ablation due to absorption, if the laser is powerful enough, other types of ablation can occur, which are mechanical mechanisms. For instance, during a ionization process like plasma formation, the cloud of free electrons act as a mechanical tool to ablate the material, then the absorption of the material is not important anymore. This type of ablation can be useful in a water environment, like general surgeries. Then the laser energy is not reduced much by the presence of water. The most common pulsed lasers for photomechanical ablation of hard tissue are the neodymium-doped lasers, like Nd:YAG, *neodymium-doped yttrium orthovanadate* (Nd:YVO_4), Nd:YLF, Ti:Sapphire, all in the nanosecond regime or less. The main difficulties of using such lasers are when the clinical application is in the field of minimally invasive surgeries. The laser must be coupled into an optical fiber, usually they brake due to the plasma. The shielding effect of the plasma-mediated ablation impedes efficient ablation, reducing the ablation rates. Additionally, from a practical point of view, plasma-mediated ablation is usually very noisy, sometimes deafening.

Clean ablation has been achieved with picosecond Nd:YAG lasers for cutting bone, for instance under water [96]. A Nd:YVO_4 of 25 ps pulse duration and $\lambda = 532$ nm, provided non-thermal ablation of the bone [97]. A study using a Ti:Sapphire *Chirped Pulse Amplifier* (CPA) system, $\lambda = 1.05\,\mu$m and variable pulse duration; 350 fs and 1 ns

pulse regimes were studied. The authors show reduced thermal damage for the fs regime compared to the ns regime [98]. Enamel and dentin have been also ablated with Nd:YLF laser at $\lambda = 1.05\,\mu$m and 30 ps pulses for tooth preparation, the results were not superior to conventional mechanical tools [99]. Regarding deep bone ablation, until now, there are no reports found in literature, where, plasma-mediated ablation shows outstanding results compared to the ones achieved by photomechanical ablation by phase explosion and confined boiling, as seen in Sec. 3.3.3.

Chapter 4

Exploring the microsecond Er:YAG laser for bone ablation and the influence of water irrigation on the ablation performance

This chapter contains two publications. The first publication shows the effect of using different water cooling conditions on bone ablated with an Er:YAG laser. We used water sequences with a water jet measuring 500 μm in diameter. Afterwards, neither carbonization nor cracks in the area surrounding the ablation were observed in the SEM images.

Publication 1: Lina M. Beltrán Bernal, Gholamreza Shayeganrad, Gabor Kosa, Marek Zelechowski, Georg Rauter, Niklaus Friederich, Philippe C. Cattin, and Azhar Zam, "Performance of Er:YAG laser ablation of hard bone under different irrigation water conditions", Proc. SPIE 10492, Optical Interactions with Tissue and Cells XXIX, 104920B (13 February 2018).
DOI: https://doi.org/10.1117/12.2290929

In the second publication, we evaluated the lateral speed of line ablation of bone with the Er:YAG laser. We used the water conditions that provided the deepest ablation, as described in the first paper. We found that at a lateral ablation speed of 8 mm/s it is possible to ablate more tissue in less time compared to other speeds. Looking at the OCT images of the ablated bones, we noted that at 8 mm/s, a decent uneven surface is obtained at the bottom of the cut.

Publication 2: Lina M. Beltrán Bernal, Iris T. Schmidt, Nikola Vulin, Jonas Widmer, Jess G. Snedeker, Philippe C. Cattin, Azhar Zam, and Georg Rauter, "Optimizing controlled laser cutting of hard tissue (bone)", at-Automatisierungstechnik 66, no. 12 (2018): 1072-1082.
DOI: https://doi.org/10.1515/auto-2018-0072

Performance of Er:YAG laser ablation of hard bone under different irrigation water cooling conditions

Lina M. Beltrán Bernal, Gholamreza Shayeganrad, Gabor Kosa, Marek Zelechowski, Georg Rauter, et al.

Lina M. Beltrán Bernal, Gholamreza Shayeganrad, Gabor Kosa, Marek Zelechowski, Georg Rauter, Niklaus Friederich, Philippe C. Cattin, Azhar Zam, "Performance of Er:YAG laser ablation of hard bone under different irrigation water cooling conditions," Proc. SPIE 10492, Optical Interactions with Tissue and Cells XXIX, 104920B (13 February 2018); doi: 10.1117/12.2290929

SPIE.

Event: SPIE BiOS, 2018, San Francisco, California, United States

Performance of Er:YAG laser ablation of hard bone under different irrigation water cooling conditions

Lina M. Beltrán Bernal[a], Gholamreza Shayeganrad[a], Gabor Kosa[b], Marek Zelechowski[c], Georg Rauter[b], Niklaus Friederich[d], Philippe C. Cattin[c], and Azhar Zam[a]

[a]Biomedical Laser and Optics Group
[b]Bio-Inspired RObots for MEDicine-Lab
[c]Center for Medical Image Analysis and Navigation
[d]Center of Biomechanics and Biocalorimetry.,

Department of Biomedical Engineering, University of Basel, Gewerbestrasse 14, 4123, Allschwil, Switzerland

ABSTRACT

The biological applicability of the Erbium-doped Yttrium Aluminum Garnet (Er:YAG) laser in surgical processes is so far limited to hard dental tissues. Using the Er:YAG laser for bone ablation is being studied since it has shown good performance for ablating dental hard tissues at the wavelength 2.94 μm, which coincides with the absorption peak of water, one of the main components of hard tissue, like teeth and bone. To obtain a decent performance of the laser in the cutting process, we aim at examining the influence of sequenced water jet irrigation on both, the ablation rate and the prevention of carbonization while performing laser ablation of bone with fixed laser parameters. An Er:YAG laser at 2.94 μm wavelength, 940 mJ energy per pulse, 400 μs pulse width, and 10 Hz repetition rate is used for the ablation of a porcine femur bone under different pulsed water jet irrigation conditions. We used micro-computed tomography (micro-CT) scans to determine the geometry of the ablated areas. In addition, scanning electron microscopy (SEM) is used for qualitative observations for the presence of carbonization and micro-fractures on the ablated surfaces. We evaluate the performance of the laser ablation process for the different water jet conditions in terms of the ablation rate, quantified by the ablated volume per second and the ablation efficiency, calculated as the ablated volume per pulse energy. We provide an optimized system for laser ablation which delivers the appropriate amount of water to the bone and consequently, the bone is ablated in the most efficient way possible without carbonization.

Keywords: Er:YAG laser, water jet irrigation, carbonization, laser ablation of bone, micro-computed tomography, scanning electron microscopy, ablation rate, ablation efficiency

1. INTRODUCTION

Lasers have been widely studied and used in dentistry applications like caries prevention in enamel tissue using a *neodymium yttrium aluminium garnet* (Nd:YAG) laser working at the wavelength $\lambda = 532$nm[1] and for the removal of soft tissue, caries, enamel and dentin using a *carbon dioxide* (CO_2) laser at $\lambda = 10\,\mu$m, an *erbium-dopped yttrium aluminium garnet* (Er:YAG) laser at $\lambda = 2.94\,\mu$m, or an *erbium-chromium-doped yttrium-scandium-gallium garnet* (Er,Cr:YSGG) laser at $\lambda = 2.78\,\mu$m.[2–6] The best lasers known so far for cutting hard dental tissues are the erbium lasers,[7] i.e. Er:YAG and Er,Cr:YSGG, both with pulse durations in the microseconds regime.

Bone and dental tissues are characterized by their mineralized and rigid structure, also their properties and compositions are similar.[8] The amount of water in dentin is around 30% of its total volume, however, the amount of water in bone varies depending on several aspects. For instance, the volume of water in human femur

Further author information: (Send correspondence to Lina M. Beltrán)
Lina M. Beltrán: E-mail: lina.beltran@unibas.ch, Telephone: +41 (0)61 207 54 61
Azhar Zam: E-mail: azhar.zam@unibas.ch, Telephone: +41 (0)61 207 54 60

Optical Interactions with Tissue and Cells XXIX, edited by E. Duco Jansen, Hope Thomas Beier, Proc. of SPIE Vol. 10492, 104920B · © 2018 SPIE · CCC code: 0277-786X/18/$18 · doi: 10.1117/12.2290929

cortical bone varies from 21% to 17% for humans of ages between 5 and 95 years,[9] respectively. In recent studies, the Er:YAG laser has shown better performance for cutting hard dental tissues and cortical bone than the Er,Cr:YSGG laser in terms of the ablation efficiency.[7,10–12] The ablation mechanism involved in the interaction process of the Er:YAG laser (working with pulse durations in microseconds) and the cortical bone is known as photo-thermal ablation,[13] in which the wavelength of the laser coincides with one of the greatest absorption peaks of water, located at $\sim 3\,\mu$m.[14] When the laser impinges the bone surface, the heat transferred to the water molecules present in the bone increases the pressure in the interstitial matrix of the bone, which finally leads to explosion and consequently removal of the tissue. On the other hand, laser ablation also quickly dries out the surrounding tissue that needs to be re-hydrated and cooled down with water, otherwise the heat acquired during ablation might lead to thermal effects like decoloration, dessication or even carbonization of the bone.[3] The water used to rehydrate the tissues will absorb the energy of the Er:YAG laser and as a result, the ablation efficiency decreases.[15] Comparing this effect with the ablation mechanism called photo-thermal ablation,[13] there is a counteracting effect when hydrating and cooling the tissues to prevent thermal damage and at the same time improving the ablation efficiency.

In conventional dental surgeries, the tissues are constantly irrigated with a water spray which disperses the water on the surface of the tissue[7] and therefore, the amount of water on the laser-tissue interaction area is reduced, allowing the laser to cut the material. This method is efficient for surface ablation of tissues. On the contrary, if deeper cuts are needed, the spray cannot penetrate well inside the cuts. As a consequence, thermal damage occurs due to the lack of water leading to stop the ablation process. In this work, we present a method to irrigate the bone tissue while it is being ablated and show the best irrigation conditions found. The irrigation system with a pulsed water jet is directed to the area of interaction with a transversal size similar to the laser beam diameter.

2. MATERIALS AND METHODS

2.1 Laser and irrigation systems

The laser used for ablating the pig femur bones was a dental Er:YAG laser Syneron litetouch LI-FG0001A, working at the wavelength $2.94\,\mu$m, with a repetition rate of 10 Hz, pulse duration of $400\,\mu$s and energy per pulse of 940 mJ. The beam size used for ablation was about $500\,\mu$m, achieved with the help of an uncoated CaF_2 lens with focal length 75 mm, which is followed by a sapphire window used to protect the lens from the particles ejected from the bone while being ablated. The schematic of the experimental setup can be seen in Fig. 1.

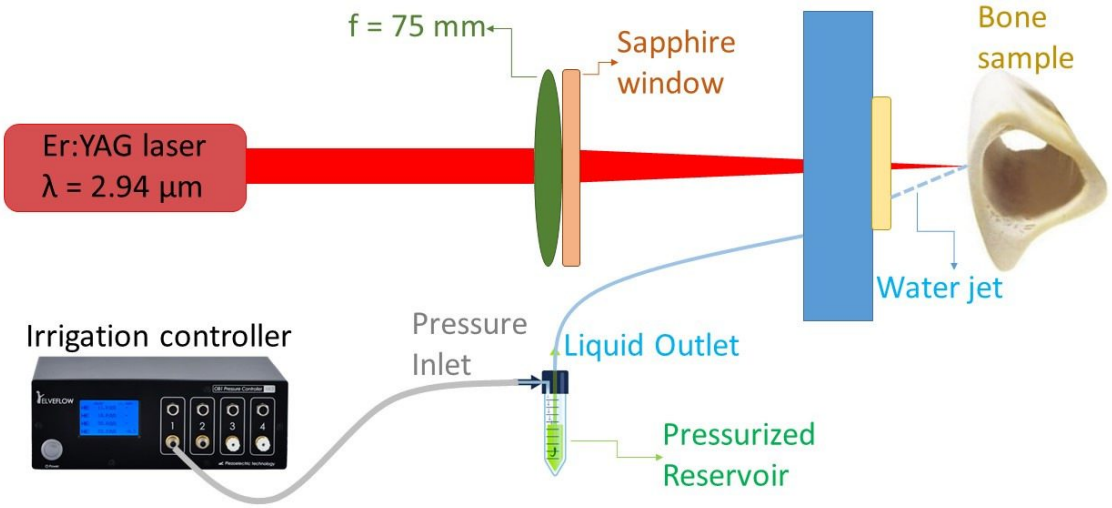

Figure 1. Schematic of the irrigation and Er:YAG laser systems used to ablate the bones. The system consists of a laser source with the optics needed to reach the bone surface and also of an irrigation system needed to rehydrate the bones and avoid carbonization.

The irrigation system used to rehydrate the tissues and also to avoid carbonization is an ESI Elveflow which has a pneumatic pressure controller, a water reservoir of 80 ml capacity and a tygon tubing coil of 500 μm inner diameter. We used the maximum pressure of 2 bar to provide a water flow with the rate of 14 ml/min and a velocity of about 1 m/s. For finding the irrigation conditions that enhance ablation efficiency most while avoiding carbonization for fixed laser parameters, the following procedure was established. The laser was continuously interacting with the bone during 7 seconds at the same time that the water jet was operated in a pulsed way: water ON alternating with water OFF. For the first group (six holes) of experiments, the water ON pulse duration was set to 0.15 s, and the water OFF pulse duration was increased from hole to hole by 0.15 s starting at 0.15 s. For the following group, the water ON pulse duration was prolonged by 0.05 s. This stepwise increase of water ON pulse durations over the groups and the pulse durations for water OFF for the groups of holes were continued (see Fig. 2) until carbonization occurred. The results shown in the following sections are related to the clean holes (those which did not have any carbonization), and for each group of sequences (water ON fixed), the amount of clean holes is different. We obtained 68 clean holes for each pig femur bone, this experiment was repeated another two times, leading to a total of 204 clean holes.

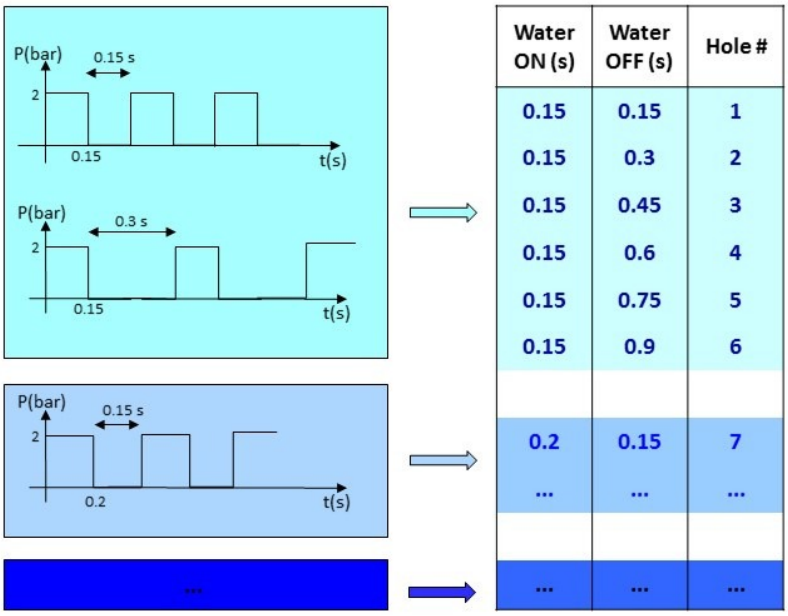

Figure 2. Schematic of the water jet sequences used in laser bone ablation with the ESI Elveflow irrigation system. Each hole made by the laser on the tissue has a different sequence.

2.2 Micro-computed Tomography (micro-CT)

For analyzing the geometry of the ablated areas in the cortical pig femur, we used a micro-computed tomography system from Bruker, reference SkyScan 1275, having a source type Hamamatsu L11871 and an isotropic resolution of 25 μm. We used an average of 3 frames and an angle increment of 0.25°, obtaining 1441 projections for each sample. The artifacts produced in the images by low energy photons, were avoided by using a copper (Cu) beam hardening filter. After the scanning process, all the three dimensional samples were reconstructed using the software provided by Bruker. Based on the 3D-reconstructions, hole depth, diameter, and removed volume were acquired.

2.3 Scanning Electron Microscopy (SEM)

Early carbonization stages are not always visible as the bone color turns darker during the ablation process which does not necessarily mean that the bone is carbonized. Scanning electron microscopy (SEM) is a technique which

is useful to identify the micro-structure of different materials. In our case, we used this technique to determine if the color changes were due to early carbonization or simply decoloration due to tissue dehydration. This is not as harmful for the patient as carbonization because the body can recover a local lack of water after some time. We used a Nova NanoSEM 230 apparatus at different magnifications to determine carbonization in the ablated areas.

3. RESULTS AND DISCUSSION

3.1 Ablation performance using different water jet sequences

Since the ablation performance of the Er:YAG laser system strongly depends on how the tissue is irrigated with water, in our study, we investigate the influence of different water jet sequences on the ablation efficiency. Initial tests with constant water ON (it means water OFF= 0 s) were performed to verify what is already well known, the water absorbs the laser energy and the ablation is not possible.[15] Afterwards, we systematically increased the time the water was OFF in a sequence, from 0.15 to $\sim$ 2 s. In that way, we could study how long the tissue can be preserved during the ablation process without water supply. Also the pulse duration for the water ON was changed from 0.15 to $\sim$ 0.4 s. As shown in Fig. 3, the bone has several holes, each corresponds to one irrigation water jet condition.

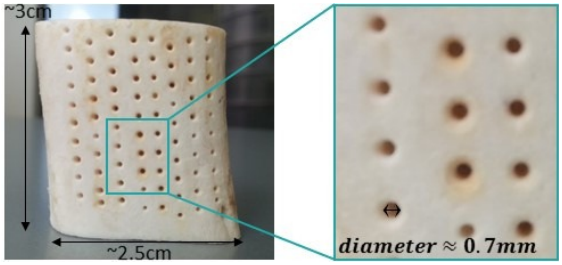

Figure 3. Picture of one bone sample in which each hole was made with the Er:YAG laser using different irrigation water jet conditions.

For each sequence we analyzed the ablated depth and also the ablated volume, as shown in Fig. 4.

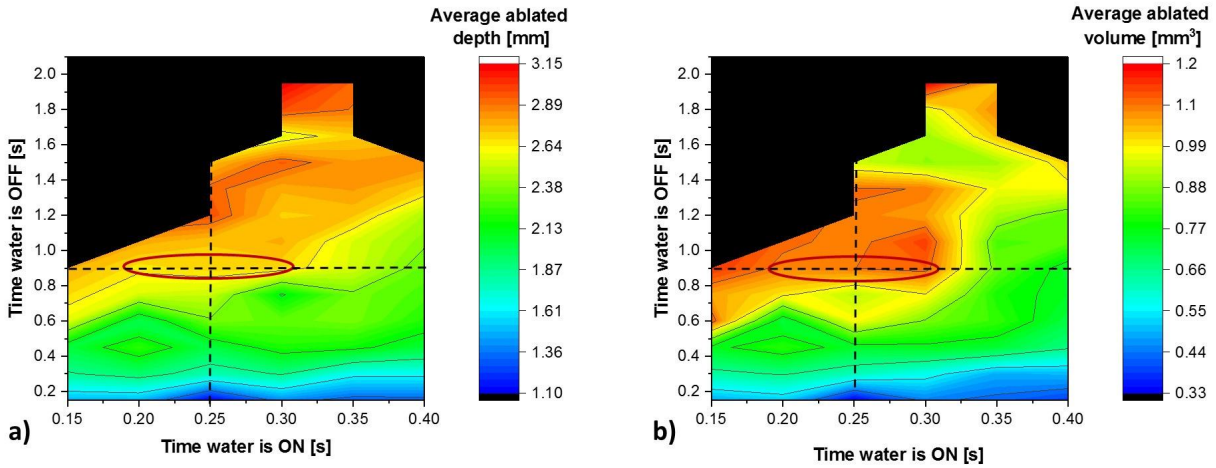

Figure 4. Average ablation depth (a) and average ablation volume (b) at different irrigation conditions. Water ON sequences start at 0.15 s as well as water OFF. The encircled areas show the best and most appropriate water jet sequences found.

In Fig. 4, we visualize the irrigation conditions used to hydrate and cool down the bones while being ablated and the respective ablated depth (color scale in (a)) and volume (color scale in (b)). The black area represents the carbonization region, those water OFF water ON conditions were not sufficient to hydrate and cool down the tissues. The horizontal dashed black line shows that for a certain water OFF time, the ablation efficiency tends to decrease as the water ON time increases, which can be visualized as well by tracing any other horizontal line on the diagram, especially for water OFF times bigger than $\sim 0.6\,\mathrm{s}$, except on the carbonization regions. This effect is due to the high absorption the water has at $2.94\,\mu\mathrm{m}$ wavelength,[14] consequently, it prevents the ablation of the material. On the contrary, the vertical dashed black line shows that as the water OFF time increases, the ablation efficiency increases as well, with the risk of carbonizing the tissue at the highest water OFF times (black areas).

Regarding all those effects, the optimal conditions for the current water jet system we are using to efficiently ablate bone with the Er:YAG laser can be found in a region where the water ON time is such that the ablation efficiency is not decreasing (horizontal direction inside the red ellipse), and the water OFF time is such that the ablation efficiency is high enough (orange or red colors in the scales) without any carbonization. The region which is encircled by a red ellipse shows the water jet conditions which fulfills those requirements. Some other regions can also be chosen because the ablation efficiency is also very high, for instance, the region where water ON is between 0.3 and 0.35 s and water OFF is between 1.6 and 1.9 s. The disadvantage of this region is the high risk of carbonization, the yellow areas around the holes made under those conditions look darker than in the other cases. The water ON time can be set between 0.2 and 0.3 s and the water OFF time can be set between 0.8 and 1 s, see red ellipses on Fig. 4. Those sequences provide an ablation speed of $A_s = 0.4\,\mathrm{mm/s}$ and an ablation rate of $A_r = 0.18\,\mathrm{mm^3/s}$. Therefore, the ablation efficiency is $0.017\,\mathrm{mm^3/pulse}$, which corresponds to $A_e = 0.018\,\mathrm{mm^3/J}$. The chosen water jet conditions are not determinant for the subsequent experiments in our future studies. Conversely, this study provides the starting point for improving the ablation efficiency in future. It has been shown that as soon as line shapes are ablated and not only holes, the ablation process will improve for all water cooling conditions used.[16]

3.2 Carbonization study using SEM

Thermal damage like carbonization is harmful for the tissues and results in a slower[17] healing process or even the complete death of tissue. In our case, while ablating bones with laser, the surrounding of the ablated concentric circle (about 1 mm outside the hole) turned into yellow colors not visible before. This phenomenon occurred mainly on the areas where the water OFF times were longer. This suggests that is the beginning of carbonization or a decoloration process due to rising temperatures and consecutive dehydration of the bone was caused by the laser ablation. To determine if the tissue was subject to early carbonization, we used SEM to analyze the micro-structure of the ablated regions.

In order to compare the different regions where the laser interacted with the bone, we analyzed areas which were untouched by the laser and far from the ablated zones, the surroundings of the laser cuts, and also completely carbonized areas which were created on purpose. In Fig. 5 the SEM pictures of the areas mentioned are shown.

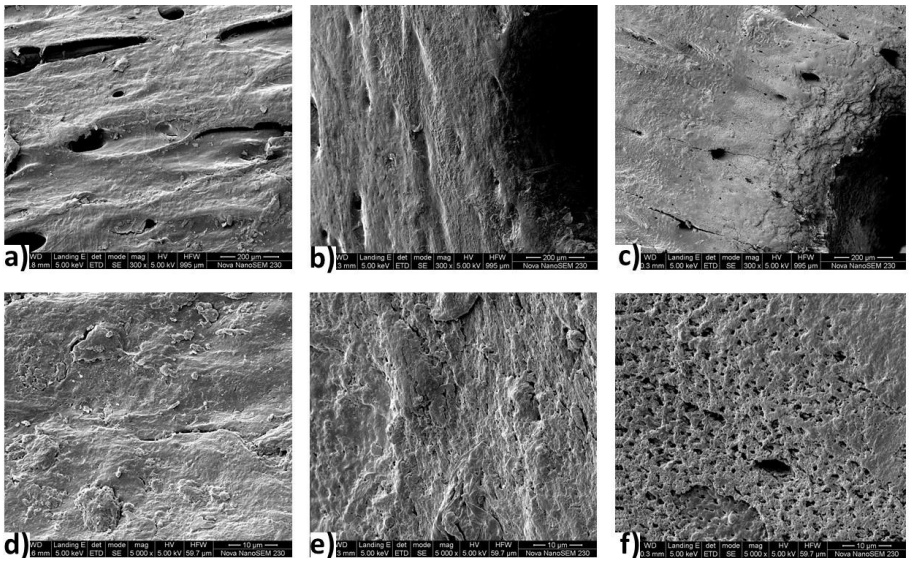

Figure 5. SEM images obtained for: an area of the bone outside the ablation regions with magnifications of 300X (panel a) and 5000X (panel d), the surroundings of an area ablated with the laser, with magnifications of 300X (panel b) and 5000X (panel e)), and the surroundings of a completely carbonized area with magnifications of 300X (panel c) and 5000X (panel f).

As observed in Fig. 5, the surroundings of the ablated hole made with the laser (b) look very similar to the area which was not affected by the laser at all (a) for 300X magnification, the osteocytes and the bone matrix are preserved in (b). Also for the 5000X magnification scan the laser cut (e) looks very similar the bone without ablation (d). Note that the images have different structure directions because the pictures were taken from different positions with respect to the bone structure pattern. On the contrary, pictures (c) and (f) show different structures from (a) and (d), respectively. In (c) and (f), there is a pore formation on the bone matrix, which means that the bone matrix has lost its structure completely, and this is due to the carbonization stage the bone has suffered. From the pictures, the carbonization stage is clear because of the pore formation. However, to identify if the yellow colors are due to a dehydration of the bone or if this is the starting point of carbonization, a different technique from SEM has to be used. Particularly, for studying decoloration changes and to distinguish these from early carbonization stages, another technique should be used like histology.[18]

CONCLUSION

In our study, we showed how the water cooling condition affects the ablation performance of the laser system from constant irrigation (water OFF 0 s) to insufficient amount of water to cool down and hydrate the bone (water OFF $\gg 0$ s), see Fig. 4. This means, from having no ablation at all to completely carbonized bone. Most importantly, we identify the best conditions for efficiently ablating bone through pulsed irrigation (red ellipses in Fig. 4). The irrigation water jet conditions which provided most efficient ablation for each water ON time are, in most of the cases, previous to carbonization of the bones (carbonization border zone in Fig 4), which is reasonable since the less water the more we can ablate the bone, but also this amount should be enough to rehydrate and cool down the tissues to avoid carbonization. Therefore, the best water jet sequences we found are for water ON times between 0.2 and 0.3 s and for water OFF between 0.8 and 1 s. Those sequences provide an ablation speed of $A_s = 0.4\,\mathrm{mm/s}$, an ablation rate of $A_r = 0.18\,\mathrm{mm^3/s}$ and an ablation efficiency of $A_e = 0.018\,\mathrm{mm^3/J}$. With SEM pictures it is possible to determine changes in the structure of the bones due to carbonization (Fig.5 (c) and (f)) but it is not possible to identify if the decoloration was due to an early carbonization stage or the tissue was suffering from a lack of water that can be recovered.

ACKNOWLEDGMENTS

The authors gratefully acknowledge funding of the Werner Siemens Foundation through the MIRACLE project.

REFERENCES

[1] Ana, P., Bachmann, L., and Zezell, D., "Lasers effects on enamel for caries prevention," *Laser Physics* **16**(5), 865–875 (2006).

[2] Stern, R. H. and Sognnaes, R. F., "Laser inhibition of dental caries suggested by first tests in vivo," *The Journal of the American Dental Association* **85**(5), 1087–1090 (1972).

[3] Visuri, S. R., Walsh, J. T., and Wigdor, H. A., "Erbium laser ablation of dental hard tissue: effect of water cooling," *Lasers in surgery and medicine* **18**(3), 294–300 (1996).

[4] Hibst, R. and Keller, U., "Experimental studies of the application of the er: Yag laser on dental hard substances: I. measurement of the ablation rate," *Lasers in Surgery and Medicine* **9**(4), 338–344 (1989).

[5] Keller, U. and Hibst, R., "Experimental studies of the application of the er: Yag laser on dental hard substances: Ii. light microscopic and sem investigations," *Lasers in Surgery and Medicine* **9**(4), 345–351 (1989).

[6] Hossain, M., Nakamura, Y., Yamada, Y., Kimura, Y., Matsumoto, N., and Matsumoto, K., "Effects of er, cr: Ysgg laser irradiation in human enamel and dentin: ablation and morphological studies," *Journal of clinical laser medicine & surgery* **17**(4), 155–159 (1999).

[7] Kuščer, L. and Diaci, J., "Measurements of erbium laser-ablation efficiency in hard dental tissues under different water cooling conditions," *Journal of biomedical optics* **18**(10), 108002–108002 (2013).

[8] Boskey, A. L., "Mineralization of bones and teeth," *Elements* **3**(6), 385–391 (2007).

[9] Timmins, P. and Wall, J., "Bone water," *Calcified Tissue International* **23**(1), 1–5 (1977).

[10] Belikov, A. V., Erofeev, A. V., Shumilin, V. V., and Tkachuk, A. M., "Comparative study of the 3um laser action on different hard tooth tissue samples using free running pulsed er-doped yag, ysgg, yap and ylf lasers," in [*Dental Applications of Lasers*], **2080**, 60–68, International Society for Optics and Photonics (1993).

[11] Stock, K., Hibst, R., and Keller, U., "Comparison of er: Yag and er: Ysgg laser ablation of dental hard tissues," in [*Medical Applications of Lasers in Dermatology, Ophthalmology, Dentistry, and Endoscopy*], **3192**, 88–96, International Society for Optics and Photonics (1997).

[12] Perhavec, T. and Diaci, J., "Comparison of er: Yag and er, cr: Ysgg dental lasers.," *Journal of Oral Laser Applications* **8**(2) (2008).

[13] Tuchin, V. V., "Tissue optics and photonics: Light-tissue interaction ii," *J. of Biomedical Photonics & Eng.* **2**(3) (2016).

[14] Vogel, A. and Venugopalan, V., "Mechanisms of pulsed laser ablation of biological tissues," *Chemical reviews* **103**(2), 577–644 (2003).

[15] Abbasi, H., Beltrán, L., Rauter, G., Guzman, R., Cattin, P. C., and Zam, A., "Effect of cooling water on ablation in er: Yag laserosteotome of hard bone," in [*Third International Conference on Applications of Optics and Photonics*], **10453**, 104531I, International Society for Optics and Photonics (2017).

[16] Burgner, J., [*Robot assisted laser osteotomy*], KIT Scientific Publishing (2010).

[17] Blaskovic, M., Gabrić, D., Coleman, N. J., Slipper, I. J., Mladenov, M., and Gjorgievska, E., "Bone healing following different types of osteotomy: Scanning electron microscopy (sem) and three-dimensional sem analyses," *Microscopy and Microanalysis* **22**(6), 1170–1178 (2016).

[18] Jowett, N., Wöllmer, W., Reimer, R., Zustin, J., Schumacher, U., Wiseman, P. W., Mlynarek, A. M., Böttcher, A., Dalchow, C. V., Lörincz, B. B., et al., "Bone ablation without thermal or acoustic mechanical injury via a novel picosecond infrared laser (pirl)," *Otolaryngology–Head and Neck Surgery* **150**(3), 385–393 (2014).

Applications

Lina M. Beltran Bernal, Iris T. Schmidt, Nikola Vulin, Jonas Widmer, Jess G. Snedeker, Philippe C. Cattin, Azhar Zam and Georg Rauter*

Optimizing controlled laser cutting of hard tissue (bone)

Optimierung von Kontrollierter Laserosteotomie

https://doi.org/10.1515/auto-2018-0072
Received May 17, 2018; accepted August 14, 2018

Abstract: Conventional bone surgery leads to unwanted damage to the surrounding tissues and a slow healing process for the patients. Additionally, physicians are not able to perform free cutting shapes due to the limitations of available systems. These issues can be overcome by robot-assisted contactless laser surgery since it provides less mechanical stress, allows precise functional cuts, and leads to faster healing. The remaining drawback of laser surgery is the low ablation rate that is not yet competitive with conventional mechanical piezo-osteotomes. Therefore, we aim at maximizing the efficiency in hard tissue laser ablation by optimizing the lateral movement speed for different irrigation conditions.

The results of this study show a non-linear relationship between cutting rates, speeds, and depths that should be critically considered for integration in robotic laser surgery.

Keywords: laser osteotomy, cutting bone, automation, laser, irrigation, cutting velocity

Article note: Lina M. Beltran Bernal and Iris T. Schmidt contributed equally to this paper.

***Corresponding author: Georg Rauter,** BIROMED-Lab, Department of Biomedical Engineering, University of Basel, Allschwil and Sensory-Motor Systems Lab, ETH Zurich and Spinal Cord Injury Center, University Hospital Balgrist, Zurich, Switzerland, e-mail: georg.rauter@unibas.ch
Lina M. Beltran Bernal, Iris T. Schmidt, Azhar Zam, BLOG, Department of Biomedical Engineering, University of Basel, Allschwil, Switzerland, e-mails: lina.beltran@unibas.ch, iris.schmidt@unibas.ch, azhar.zam@unibas.ch
Nikola Vulin, Jonas Widmer, Jess G. Snedeker, Department of Orthopaedics, University of Zurich, Institute for Biomechanics, ETH Zurich, Zurich, Switzerland, e-mails: nvulin@student.ethz.ch, jonas.widmer@hest.ethz.ch, jess.snedeker@hest.ethz.ch
Philippe C. Cattin, CIAN, Department of Biomedical Engineering, University of Basel, Allschwil, Switzerland, e-mail: philippe.cattin@unibas.ch

Zusammenfassung: Konventionelle chirurgische Eingriffe am Knochen führen zu ungewollten Schäden im umliegenden Gewebe. Außerdem ziehen diese Eingriffe am Knochen einen langsamen Heilungsprozess für den Patienten nach sich. Auch erlauben es herkömmliche chirurgische Systeme den Ärzten nicht freie Schnittformen zu erzielen. Mit robotergestützter kontaktfreier Laserchirurgie können diese Limitierungen jedoch überwunden werden; Laserchirurgie führt zu geringeren mechanischen Spannungen im Gewebe, erlaubt präzise funktionelle Schnitte und lässt den Knochen schneller heilen. Bleibt allein, dass die Schnittgeschwindigkeit in der Laserchirurgie (Laserosteotomie) bis jetzt nicht mit jener von konventionellen Piezoosteotomen mithalten kann. Aus diesem Grund arbeiten wir daran die Effizienz von Laserosteotomie zu erhöhen indem die laterale Laserbewegung für verschiedene Befeuchtungsparameter optimiert wird.

Die Resultate der vorliegenden Studie zeigen ein nichtlineares Verhältnis von Schnittraten, lateraler Laserbewegung und Schnitttiefe. Diese Erkenntnisse sollten unbedingt berücksichtigt werden, wenn Laserchirurgie in robotergestützten Chirurgiesystemen eingesetzt wird.

Schlagwörter: Laserosteotomie, Knochenschneiden mit Laser, Automatisierung, Laserparameter, Wasserparameter, Schnittgeschwindigkeit

1 Introduction

Laser ablation is an accurate, contactless method for cutting hard tissue in the body. It has been shown that laser osteotomy reduces the healing time of the remaining bone compared to conventional bone cutting with piezoosteotomes. The reason for accelerated healing is that the spongy structure remains intact [1]. Until today, highest ablation rates could be reached using mid-IR laser pulses, such as the erbium-doped yttrium aluminum garnet (Er:YAG) laser, with a wavelength of 2.94 μm. Hereby,

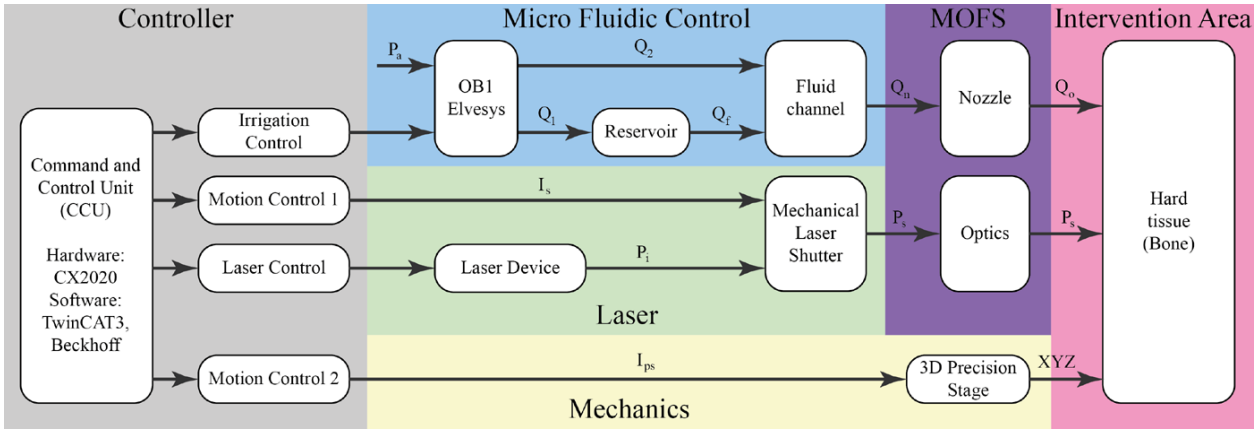

Figure 1: Scheme of the test setup for investigating relative motion between bone and laser on osteotomy performance.

the underlying physical principle of laser ablation is based on thermo-mechanical effects produced by the interaction between the microsecond pulses of the Er:YAG laser working close to one of the highest absorption peaks of water (around 3 μm). Namely, ablation is performed by the rapid evaporation of the water content in hard tissue due to the heat transfer from the microsecond laser to the area of interaction, and consequently the clean removal of the target tissue without significant heat transfer to the surrounding bone [2]. Thermo-mechanical ablation, however, reduces the water content of the bone and in order to rehydrate the tissue and consequently prevent carbonization, the lased area has to be irrigated with water [3]. The standard solution for this problem is continuous spraying of the cutting area with water spray [4]. However, since continuous spraying will not only irrigate the bone, but create a layer of water on its surface, the Er:YAG laser cannot be expected to ablate bone efficiently. Thus, a continuous spray will act as a protection against ablation.

To overcome the limitations of laser ablation efficiency in bone due to continuous spraying, we investigated the effect of different discontinuous/pulsed irrigation conditions on ablation efficiency in a previous study [5]. The focus of this paper is to optimize controlled laser cutting of hard tissue (bone) by varying lateral cutting speeds for different irrigation conditions while the laser parameters remain untouched.

To enable controlled optimized laser ablation for minimal invasive surgery, we are developing an automated closed-loop controlled robotic endoscope for laser ablation of bone (laser osteotome) with a microfluidic system for irrigation. In the current development state, the laser is not yet integrated in the robotic endoscope [6, 7, 8, 9] and therefore experiments are carried out in our optics and laser lab [10, 11, 5]. To investigate the influence of different velocities on the cutting performance, we have developed a test setup mounted on an optical table. This setup allows creating controlled conditions for irrigation, laser, and relative motion between laser and bone (Figure 1). From research of other groups in the field, it is already known that coordinated alternating provision of laser light and irrigation increases the ablation efficiency while carbonization of the hard tissue could be prevented [12]. However, the long waiting time in between the pulses (repetition rate was 0.2 Hz) was not suitable for a real intervention. Moreover, the cutting conditions might change as soon as the laser moves across the bone to create not only single holes in the bone, but also cutting lines. The necessity of optimized parameter settings for laser and irrigation can even be used in an inverted way. Instead of increasing the ablation efficiency, also a desired reduction of the ablation rate can be desirable when the laser cuts get close to delicate tissue such as nerves [13]. However, in this paper, we intend to optimize the lateral cutting speeds for different irrigation settings [5] in order to maximize the ablation efficiency without carbonization of the tissue. We also want to ensure that the ablation has high quality, which means that the bottom of the ablation crater along the lateral cutting direction is smooth and does not consist of single holes leading to perforation rather than continuous cuts.

The achieved cutting depth was measured with an optical coherence tomography (OCT) system, which additionally allowed a visualization of the top and cross-section views of the obtained laser cuts. Using OCT for the evaluation of the ablation crater after performing laser ablation in bone is a very promising approach, since OCT systems can acquire 3-dimensional scans of the light that is reflected and scattered at the bone surface. Typically, these

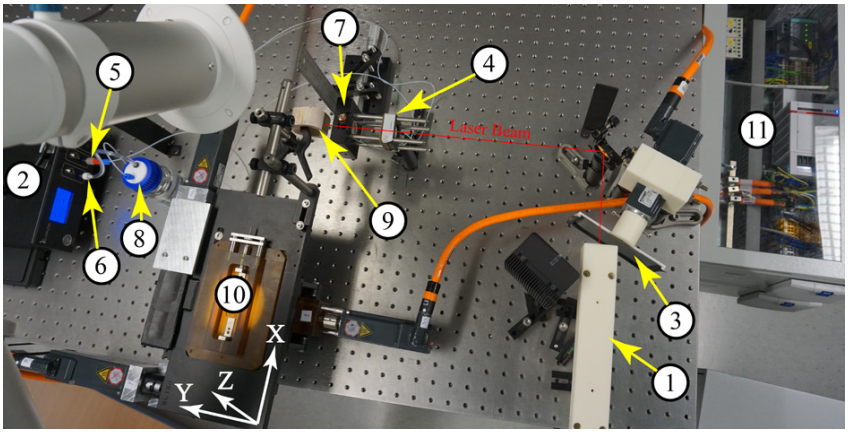

Figure 2: Experimental setup for the laser osteotome.

3-dimensional volumes are in the size of a few millimeters and have a resolution of a few micrometers. That is why, OCT was already used in different studies for measuring laser ablation craters in bone [14, 15, 13, 16]. The non-invasive character of an OCT measurement as well as the possibility to measure the ablated surface in situ and in real-time, makes OCT a smart and promising feedback technique in laser ablation-based osteotomy as other applications in surgery show [17].

2 Methods

Our laser osteotome consists of an Er:YAG laser system (LITETOUCH by Syneron) working at a wavelength of 2.94 μm, a laser spot diameter of 0.5 mm a repetition rate of 10 Hz, an energy per pulse of 940 mJ, and a pulse duration of 400 μs. The laser is controlled by a mechanical shutter operated by an AM8111 motor in TwinCAT3 (Beckhoff Automation AG, Germany) at an update rate of 1 kHz. Similarly, a precision stage for microscopes (Prior Scientific, Germany) was equipped with two AM8111 for actuating the bone in the horizontal plane (X and Y-direction). The absolute position resolution of all motors was set to 20 $\frac{\text{bit}}{\text{revolution}}$ and the stages had a spindle steepness of 0.002 $\frac{\text{m}}{\text{revolution}}$. For actuation of the Z-direction (vertical axis), a lifting table with scissor kinematics was used (L490/M Thorlabs GmbH, Germany) in combination with another AM8111. A bovine femur bone was rigidly connected with a holder to the XYZ-actuation mechanism. For controlled irrigation, a microfluidic control system, OB1 (Elvesys, France) with two channels was installed; a liquid channel and an airflow channel that can be controlled individually. The airflow, Q2 and water flow Qf are guided to the focal spot of the laser on the bone surface. Hereby, the air jet can deflect the water jet to allow laser ablation under dry conditions when the laser pulse is present, and irrigation through a jet of deionized water, when the laser is off (Figure 1).

The experimental setup (Figure 2) operates in the following way: A command computer controls the Er:YAG laser (1) and the pressure source (2). The laser beam is switched on/off by the mechanical shutter (3) and shaped by the optical components (4). The pressure source (2) regulates two airflows, (5) and (6). (5) is guided directly to a nozzle (7). The airflow of (6) is guided into a water reservoir (8) where it is converted into a water flow. The laser, water jet, and air jet are dispensed from the nozzle (7) and focus on the bovine femur bone (9). During the stationary operation of the laser (1) and the pulsed irrigation system (2,5,6,7), the bone can be moved in X-direction at a constant speed with the 3D precision stage (10). After each linear movement in X-direction, the bone can be lowered in Z-position to start a new laser line with a different condition, e. g., different speed in X-direction. In total, the automation system (TwinCAT3, Beckhoff Automation AG, Germany) (11) is set up to realize five different lateral speeds (velocities in X-direction): $v_1 = 0.5\,\frac{\text{mm}}{\text{s}}$, $v_2 = 1\,\frac{\text{mm}}{\text{s}}$, $v_3 = 2\,\frac{\text{mm}}{\text{s}}$, $v_4 = 4\,\frac{\text{mm}}{\text{s}}$, $v_5 = 8\,\frac{\text{mm}}{\text{s}}$. Higher lateral speeds were not of interest in this study, since the laser would start creating single holes only instead of a continuous line. Also, high tool speeds should be avoided in minimal invasive surgeries for safety reasons, e. g., to allow enough reaction time for the surgeon to stop a process.

Based on this experimental setup of laser, XYZ-stage, and irrigation, we performed two different experiments. The goal was to find the optimal lateral speed that results in the highest ablation efficiency for different irrigation settings and a constant set of laser parameters for single and repeated cuts. Therefore, the first experiment was intended to select the best irrigation conditions out of the two best ones from a previous experiment, where single hole cutting was performed [5]. In the second experiment,

single and repeated cuts were performed at different lateral speeds at fixed irrigation settings to investigate the effectiveness of laser ablation also in deeper cuts.

2.1 Experiment 1

In the first experiment, the bone was actuated at 5 different lateral speeds in X-direction, and therefore, line shapes were ablated. Moreover, we used 2 different irrigation settings that summed up to a total of 10 line cuts. The following irrigation settings were employed:

Table 1: Table of irrigation conditions. Sequences used for the pulsed water jet used in experiment 1. For irrigation condition 1, the duration of one irrigation period was 0.9 s and 1.15 s for irrigation condition 2.

Experiment 1	Water ON duration	Water OFF duration	Water pulse speed	Water volume per pulse
Irrigation condition 1	0.15 s	0.75 s	1 $\frac{m}{s}$	30.4 μl
Irrigation condition 2	0.25 s	0.9 s	1 $\frac{m}{s}$	50.7 μl

These irrigation conditions were chosen based on the water jet conditions used in a previous study [5], in which a bovine bone was ablated only in Y-direction, creating single holes. In that study, several irrigation configurations were evaluated in terms of ablated depth and ablated volume in time. Back then when only ablating a hole, the irrigation conditions 1 and 2 provided an ablation rate (ablated bone in depth over time) of 0.37 $\frac{mm}{s}$ and 0.4 $\frac{mm}{s}$, respectively.

2.2 Experiment 2

Based on the results of the first experiment, we chose the irrigation condition that led to highest ablation rates overall: irrigation condition 2. The irrigation settings were then kept the same throughout the entire second experiment. Consequently, line cuts were performed with the same 5 different lateral speeds in X-direction as in the first experiment. In particular, we were interested to understand how the lateral cutting velocities impact cutting efficiency for deeper cuts. To do so, the laser moved over the same lines in a repeated way (1 to 5 times). Additionally, the experiment was performed for all five velocity conditions (v_1 to v_5). Thus, the experiment led to a total of 25 different line cuts in 25 Z-positions.

2.3 Setup for measurement of cutting performance

The cross-sections of the line cut profiles were obtained with a custom-made OCT system, based on an Axsun swept laser source (λ_0 = 1060 nm, $\Delta\lambda$ = 100 nm, sweep rate 100 kHz). The system enables acquiring volumes with a size of up to 7.5 × 1.6 × 7.5 mm^3 at a volume rate of 0.37 $\frac{volumes}{s}$ and preview them at the monitor in real-time. This system has an axial and a lateral resolution of 12 μm. A general description of these parameters can be found in [18].

For analyzing the depth of each line cut, we acquired OCT B-scans with an extent of 1.6 mm in depth and 2.2 mm lateral extension at the middle of each line cut and perpendicular to the cutting direction (see Figure 3 and Figure 7).

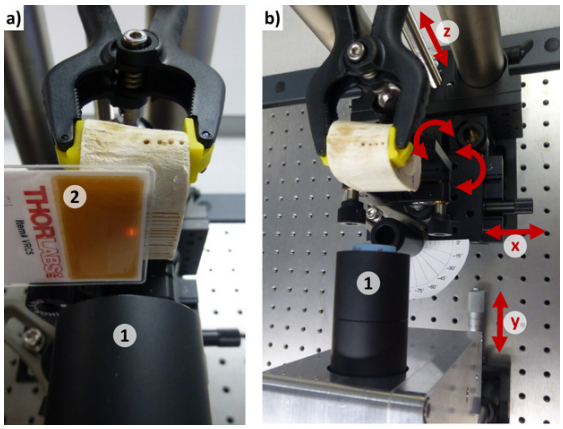

Figure 3: OCT setup: (a) and (b) show how the OCT measurements of the line cuts were set up. The last lens of OCT system (1) focused the beam on the bone surface and scanned a line on the surface. The IR detection card (2) visualized the line scan of the OCT beam (a). The alignment of the bone sample in the focus plane of the OCT system was achieved by using three translation stages (X,Y,Z) and one kinematic mount as indicated with arrows (b).

2.4 Depth measurement

The measurement of the ablation depths of the OCT scans was performed in manual segmentation using ImageJ (see Figure 4). The distance between the deepest point of the cut and the surface of the bone was measured (blue vertical line in Figure 4). We assumed a flat initial bone surface that was the linear connecting surface of the surrounding non-ablated bone regions (yellow horizontal line in Figure 4).

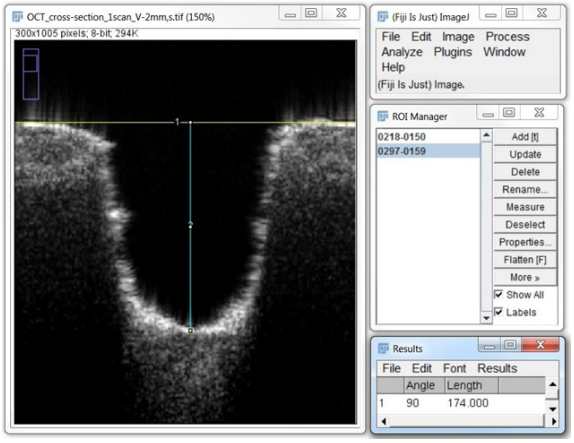

Figure 4: The OCT interface shows an example of the manual depth measurement using ImageJ. In this example, the cutting depth (indicated by the blue vertical line) was measured to be 174 pixels in length that equals to 252 μm.

3 Results

3.1 Experiment 1

The study in [5] evaluated different water jet cooling conditions for ablating bone by creating single holes. In our study, we used two of those conditions in experiment 1 to create continuous ablations of straight lines. The influence of these two irrigation conditions are evaluated by measuring the ablated depth for the velocities v_1 to v_5. Figure 5 shows a photograph of the laser cuts for the five different velocities and Figure 6 shows the OCT cross-section and top view images of those ablated areas.

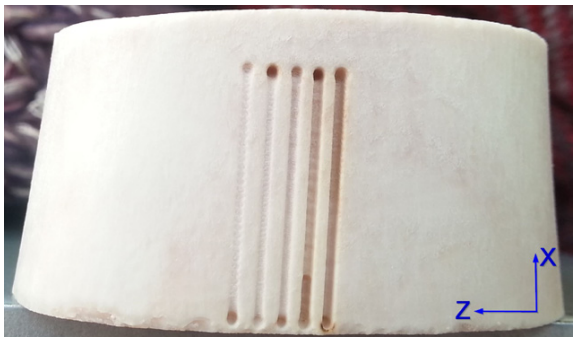

Figure 5: Picture of the resulting laser cuts at 5 different lateral speeds between laser and bone in experiment 1. Each cut line in Z-direction was generated with another constant speed in X-direction (decreasing velocities from left to right). In experiment 2 (not visualized here), new cutting lines were made for the different cutting iterations (1 to 5) at different velocities (v_1 to v_5), therefore, 25 cuts were made in total.

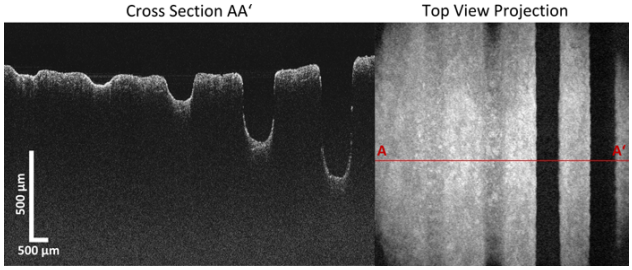

Figure 6: OCT images of the five laser cuts from Figure 5 with different lateral movement speeds (decreasing speed from left to right). Cross section (left image) and top view (right image).

In Table 2, the achieved ablated depths are summarized for the two irrigation conditions and the five speed conditions. The ratios between the ablated depths provide the relative influence of the irrigation conditions on the ablation process. This ratio was calculated by dividing the depth of irrigation condition 2 at a respective velocity (D_2) by the corresponding depth value of the irrigation condition 1 (D_1). The ratio reports the advantage of ablation depth for irrigation condition 2 for values larger than 1 (and vice versa for values smaller than 1). This ratio was calculated for each lateral speed, as well as an overall performance (average of the depth ratio).

Table 2: Table for comparison of irrigation conditions.

Velocity condition [$\frac{mm}{s}$]	Cutting depth irrigation condition 1 [μm]	Cutting depth irrigation condition 2 [μm]	Depth ratio [1]
$v_1 = 0.5$	640	637	0.99
$v_2 = 1$	388	372	0.96
$v_3 = 2$	146	252	1.72
$v_4 = 4$	58	90	1.55
$v_5 = 8$	38	72	1.90
Average of depth ratio			1.43

3.2 Experiment 2

Figure 7 compares the B-scans (cross-sections) perpendicular to the cutting direction for the four most different ablation settings (1 cutting iteration at v_1, 5 iterations at v_1, 1 iteration at v_5, and 5 iterations at v_5). Additionally, we acquired B-scans of the same size at the middle of each line cut showing the bottom of the cut profile along the cutting direction. These B-scans are presented in Figure 7 (e-h) and show that the surface of the cut profile along the cutting direction has some regular unevenness in height (ripples).

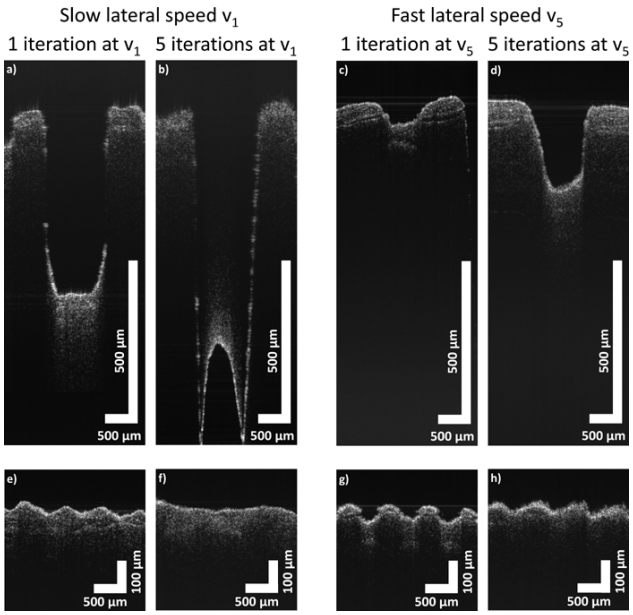

Figure 7: The OCT image shows the comparison of the cut profiles of the four most different ablation settings. Fig. (a-d) show the cut profiles at the middle of each line cut and perpendicular to the lateral cutting direction (YZ-plane). Based on these cross-sections, the cutting depth was determined. Due to the limited depth range of the OCT system, we needed to use both sides of the zero delay to acquire the profile of the deepest cut. As a consequence, the cut profile appears "folded" in the cross-section view (b). However, this has no negative effect on the evaluation of the cutting depth. Fig. (e-h) show the bottom of the ablation crater in the OCT cross-sections at the middle of each line cut along the lateral cutting direction (XY-plane).

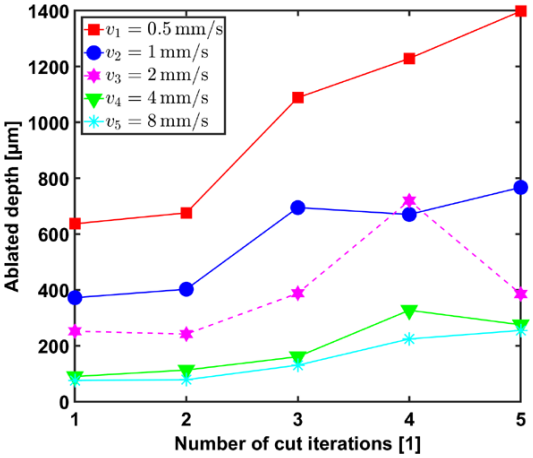

Figure 8: The ablation vs. iteration relation shows the final ablation depths achieved by using different lateral speeds and different number of repetitive line cuts at the same location.

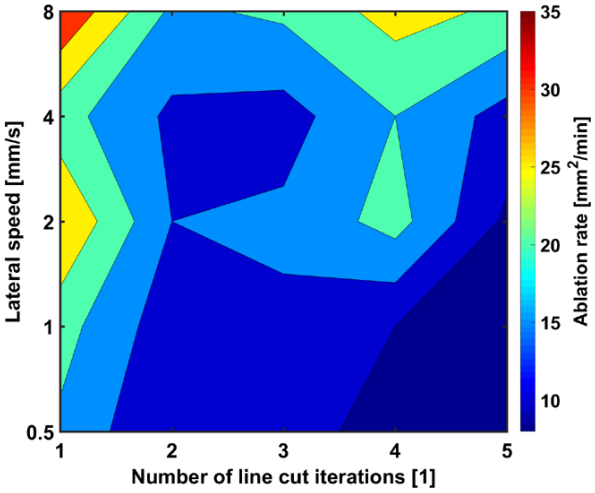

Figure 9: The color-map shows the ablated area in the cross-section perpendicular to the cutting direction over time.

In order to obtain comparable measurements for the following evaluation of the cutting depths, we chose the cross-sections (B-scans) perpendicular to the lateral cutting direction containing the deepest ripple.

The crater depths created with the laser system and then measured with OCT are depicted in Figure 8. For each lateral speed, the ablation efficiency changes as the laser is ablating deeper layers (line cut iterations) of the bone.

The ablation area rate is a measure of how efficient the ablation is over time and is given by

$$\text{ablation area rate} = \frac{\text{ablation depth} * \text{lateral speed}}{\text{number of line cut iterations}}. \quad (1)$$

This formula calculates the size of the area that was ablated in 1 second. This area is located in the XY-plane along the lateral cutting direction in the middle of the cut. Figure 9 shows a 3-dimensional contour color map of the ablation area rate for different lateral speeds and up to five line cut iterations.

4 Discussion

4.1 Experiment 1

In the first experiment of our study, we aimed to investigate the influence of two different irrigation conditions (shown in Table 1) on the ablation rate of our laser system when ablating bovine femur bone. In a previous study [5], irrigation condition 2 already enabled the best cutting depth (ablation rate) when creating only single holes. In our study on line cutting, we compared two of the irrigation conditions that were used in the previous study among which the best condition was employed again (condition 2). For irrigation condition 1, we achieved the fastest depth increase at the

lateral speed of $v_2 = 1\,\frac{\text{mm}}{\text{s}}$, which led to an ablation area rate of 23.28 $\frac{\text{mm}^2}{\text{min}}$ (see equation 1). In comparison, for irrigation condition 2, we achieved the fastest depth increase at the lateral speed of $v_5 = 8\,\frac{\text{mm}}{\text{s}}$, which corresponds to an ablation area rate of 34.73 $\frac{\text{mm}^2}{\text{min}}$. From these results and the ones presented in Table 2, we concluded that irrigation condition 2 provides in total a higher ablation depth than irrigation condition 1. Therefore, we used irrigation condition 2 in experiment 2.

4.2 Experiment 2

The goal of experiment 2 was to investigate the ablation efficiency for deeper cuts and also to observe the quality of the surface after ablation that will result when the laser is moved several times over the same cutting line at different speeds. To limit the number of possible combinations, the best irrigation condition of experiment 1 was employed throughout experiment 2: irrigation condition 2. A maximum of up to 5 repetitions per line cut at the 5 lateral speeds v_1 to v_5 were performed. To ensure a line cut and not several holes separated along the cutting line, we had to limit our lateral speeds to a maximum of $v_5 = 8\,\frac{\text{mm}}{\text{s}}$ for the current laser settings (see Figure 7g and 7h). Figure 8 shows, as already demonstrated before for single hole ablation [14], that the ablation depth increases non-linearly as the number of line cuts increases at the same Z-position. This nonlinear behavior is observed for all lateral speeds.

Figure 9 shows that the highest ablation efficiency was obtained with the highest lateral speed and a single line cut; in this case, the achieved ablation area rate was 34.73 $\frac{\text{mm}^2}{\text{min}}$ (calculated by equation 1). Furthermore, Figure 9 illustrates that, within the scope of our experiment, it was most efficient to perform a single line cut and to increase the lateral speed until the maximum lateral speed of 8 $\frac{\text{mm}}{\text{s}}$. As soon as the maximum lateral speed was reached, we could increase the number of line cut iterations while preserving a high ablation area rate.

Figure 8 shows directly which lateral speed and number of line cut iterations need to be set in order to achieve the desired ablation depth. In the next step, the found pair of values can be compared using Figure 9 to ascertain which combination enables the highest ablation area rate. Thus, these figures can be used as a kind of look-up table for finding the best parameter settings in terms of high ablation rate, which is especially useful in feed-forward control, but also for model-based feedback control.

Besides the efficiency and the ablation depth, there might also be other performance criteria that are important for the user such as the smoothness of the surface. Imagine we want to obtain a line cut with a depth around 380 μm. Figure 8 shows that this cutting depth can be achieved with two different settings; either we perform a single line cut at lateral speed $v_2 = 1\,\frac{\text{mm}}{\text{s}}$ or three cutting iterations using scan velocity $v_3 = 2\,\frac{\text{mm}}{\text{s}}$. Focusing on the ablation efficiency only (see Figure 9), one single line cut at $v_2 = 1\,\frac{\text{mm}}{\text{s}}$ is faster and thereby better setting for this task. Additionally, aiming for a smooth residual cutting surface, Figures 7a and 7g show that using only a single cut iteration leads to a rippled cutting surface for all evaluated lateral speeds v_1–v_5. Therefore, more than one cutting iteration is necessary for a smoother surface and this implies that three cutting iterations at the lateral speed $v_3 = 2\,\frac{\text{mm}}{\text{s}}$ are the best setting in this case. In short, if a smooth cutting surface is desired, then it is not only the ablation efficiency that matters.

In the depth measurement process, we assumed a flat initial bone surface that was the linear connecting surface between the surrounding non-ablated bone regions. However, the bone surface of every femur is always curved to some extent and has surface irregularities (e. g., little bumps). Thus, if the laser ablation is performed at the valley of a little bump, then the depth of this valley will add up to the cutting depth caused by the laser ablation and in total result in a deeper cut than expected. Moreover, the bone was not well realigned to every new line cut. Thus, the curviness of the bone might cause that the bone surface is not always mounted perpendicularly to the incoming ablation beam. In these cases, it is difficult to define the correct depth offset position of the initial surface, which might cause an inaccuracy in the depth measurement. These reasons could have caused the clearly higher depth (of 719 μm) measured for the line cut created in four cutting iterations with a lateral speed of $v_3 = 2\,\frac{\text{mm}}{\text{s}}$.

4.3 Limitations of the system

To increase the reliability of our results, the experiments should be repeated many times using different bones to enable strict statistical analysis. Additionally, in our study, we controlled the laser ablation in feed-forward mode, laser and irrigation system were not yet synchronized. Measurement outliers as described above might be avoided by using real-time feedback from the OCT system for a closed-loop control of the laser ablation process. However, the implementation of a real-time feedback is a challenging task, since the OCT data processing needs to be speeded-up (usually using the high processing power of

graphics processing units and reducing the region of interest). As an additional constraint for enabling a closed-loop control of the laser ablation system, the data packages and data rates transferred to and in the control loop must allow sufficiently high data rates [19]. Although we are working on the synchronization of the ablation laser, the irrigation system, the OCT system, and the lateral movement of the bone, this synchronization process is not completed yet. Besides the OCT system, additional feedback should be integrated to our system to ensure the proper performance of the complete laser ablation system. This will be particularly important to control the cutting depth online since bones have complex geometric shapes that will require different cutting depths for each spot, e. g., to completely cut through bone.

In a surgery, there are additional parameters that should be taken into consideration. For example, blood is an opaque medium and can absorb the energy of OCT and ablation beams. In order to overcome this issue, bleeding can be removed by an irrigation and suction system. We plan to optimize the timing of the ablation pulse, the irrigation and suction system, as well as the OCT measurement, so that the OCT system measures at the time we expect the least blood content in the cutting area. Moreover, to prevent carbonization of the tissues, the body temperature should be monitored by feedback mechanisms like infrared cameras and the structure of the bone can be monitored by the OCT system.

5 Outlook

In future, we plan to combine the laser ablation beam with the probing beam of the OCT system by a coaxial setup. An important improvement of this combination will be that the location of the bone surface can be measured before any ablation is performed and can be tracked during the ablation process. Measuring the bone surface not only after but also before an ablation will make the estimation of the initial bone surface unnecessary. Thereby, the depth measurement errors arousing from curvy and uneven bone surfaces will be eliminated. Additionally, we are currently working on an algorithm for an automatic depth measurement from the cross-sections of the cut profile (as shown in Figure 7). Furthermore, the coordination and synchronization of the different devices involved in laser osteotomy is a challenging task and will be an important part of our future work.

To provide an outlook on our complete system (within the scope of the MIRACLE project) for minimally invasive robot-assisted computer guided laser osteotomy, a control chart is provided that depicts the different system components and also indicates how we plan to close control loops (Figure 10). To find out more about the different system components and their state of development please refer to: [6, 7, 8] for the robotic endoscope tip, [9] for the robotic endoscope, [20] for angle sensors, [21] for shape sensing, and [22, 23, 24] for force sensing of the robotic endoscope,

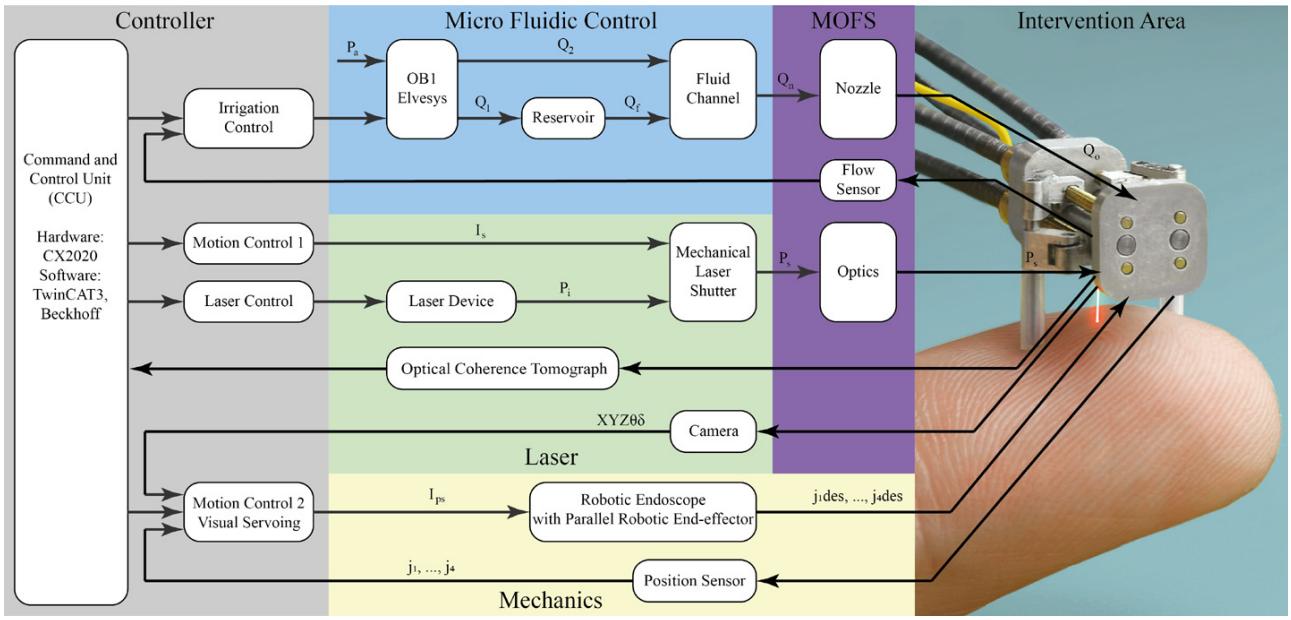

Figure 10: Scheme of the future closed-loop setup for in minimally invasive osteotomy.

[25, 26] laser-induced break down spectroscopy or [27, 28] Mach-Zehnder Interferometry for feedback on tissue types.

6 Conclusion

The current test setup allows a controlled and coordinated testing of different parameters (laser, 3D precision stage, irrigation) for generating continuous cuts in free space experiments. The resulting cutting depth strongly depends on several parameters: the setting of the irrigation system, the lateral speed between the laser and the bone, and the number of line cut iterations at the same location. In experiments, we investigated two irrigation conditions and five different relative speeds between bone and laser (ranging from 0.5 $\frac{\text{mm}}{\text{s}}$ to 8 $\frac{\text{mm}}{\text{s}}$). We performed additional line cuts on top of the previous one (in total up to five line cuts) at the same Z-position. We could confirm previous work that showed non-linear behaviour of repeated laser cuts at the same spot and expanded this knowledge also to cutting of lines. With the best conditions for the irrigation parameters and constant laser parameters, we obtained the highest ablation area rate of 34.73 $\frac{\text{mm}^2}{\text{min}}$ with a lateral speed of 8 $\frac{\text{mm}}{\text{s}}$ and a single line cut. Additionally, we obtained a mapping of parameter settings for desired ablation depths, cutting speeds, and repetitions that can be used in feed-forward and closed-loop control of laser ablation. Furthermore, we could give a qualitative impression of what influence these parameters have on the residual surface smoothness.

Acknowledgment: Also, the authors would like to thank Dr. Gabor Kosa, and Dr. Gholamreza Shayeganrad for their support in the planning phase of this paper. In addition, the authors acknowledge Manuela Eugster, Lorin Fasel, and Reinhard Wendler for providing us the robot image used in Figure 10.

Funding: The authors would like to thank the Werner-Siemens foundation for their generous support of this study within the MIRACLE project.

References

1. K.-w. Baek, W. Deibel, D. Marinov, M. Griessen, M. Dard, A. Bruno, H.-F. Zeilhofer, P. Cattin and P. Juergens, "A comparative investigation of bone surface after cutting with mechanical tools and er: Yag laser," *Lasers in surgery and medicine*, vol. 47, no. 5, pp. 426–432, 2015.
2. V. V. Tuchin, "Tissue optics and photonics: Light-tissue interaction ii," *J. of Biomedical Photonics & Eng*, vol. 2, no. 3, 2016.
3. G. Rajitha Gunaratne, R. Khan, D. Fick, B. Robertson, N. Dahotre and C. Ironside, "A review of the physiological and histological effects of laser osteotomy," *Journal of medical engineering & technology*, vol. 41, no. 1, pp. 1–12, 2017.
4. S. R. Visuri, J. T. Walsh and H. A. Wigdor, "Erbium laser ablation of dental hard tissue: effect of water cooling," *Lasers in surgery and medicine*, vol. 18, no. 3, pp. 294–300, 1996.
5. L. M. B. Bernal, G. Shayeganrad, G. Kosa, M. Zelechowski, G. Rauter, N. Friederich, P. C. Cattin and A. Zam, "Performance of er: Yag laser ablation of hard bone under different irrigation water cooling conditions," in *Optical Interactions with Tissue and Cells XXIX*, vol. 10492. International Society for Optics and Photonics, 2018, p. 104920B.
6. M. Eugster, P. Weber, P. Cattin, A. Zam, G. Kosa and G. Rauter, "Positioning and stabilization of a minimally invasive laser osteotome," in *Proceedings of The Hamlyn Symposium on Medical Robotics*. Imperial College London and the Royal Geographical Society, 2017, pp. 21–22.
7. M. Eugster, P. Weber and G. Rauter, "Medical endodevice," Switzerland patenteu European Patent Application EP 17 177 760.0, 6 26, 2017.
8. M. Eugster, E. I. Zoller, L. Fasel, P. C. Cattin, N. F. Friederich, A. Zam and G. Rauter, "Contact force estimation for minimally invasive robot-assisted laser osteotomy in the human knee," in *8th Joint Workshop on New Technologies for Computer/Robot Assisted Surgery, London, 14.–15. September 2018*, Sep. 2018.
9. M. Ahmadi, R. Haji Hassani, G. Kosa, A. Zam, R. Guzman, P. C. Cattin and G. Rauter, "Endocat: An ethercat-based articulated rear view endoscope for single port surgery," in *Biomedical Robotics and Biomechatronics (BioRob), 2018 7th IEEE RAS and EMBS International Conference on*. IEEE, 2018, accepted.
10. H. Abbasi, L. Beltrán, G. Rauter, R. Guzman, P. C. Cattin and A. Zam, "Effect of cooling water on ablation in er: Yag laserosteotome of hard bone," in *Third International Conference on Applications of Optics and Photonics*, vol. 10453. International Society for Optics and Photonics, 2017, p. 104531I.
11. L. Beltrán, H. Abbasi, G. Rauter, N. Friederich, P. Cattin and A. Zam, "Effect of laser pulse duration on ablation efficiency of hard bone in microseconds regime," in *Third International Conference on Applications of Optics and Photonics*, vol. 0453. International Society for Optics and Photonics, 2017, p. 104531S.
12. L. Kuscer and J. Diaci, "Measurements of erbium laser-ablation efficiency in hard dental tissues under different water cooling conditions," *Journal of biomedical optics*, vol. 18, no. 10, p. 108002, 2013.
13. A. Fuchs, L. Kahrs and T. Ortmaier, "Optimizing laser ablation parameters and setup for robot-assisted bone cutting and drilling," *Hanover, Germany: Ortmaier Institute of Mechatronic Systems, Leibniz Universität Hannover*, p. 30167, 2014.
14. C.-A. Tulea, J. Caron, N. Geh-lich, A. Lenenbach, R. Noll and P. Loosen, "Laser cutting of bone tissue under bulk water with a pulsed ps-laser at 532 nm," *Journal of biomedical optics*, vol. 20, no. 10, p. 105007, 2015.
15. S. A. Ashforth, M. C. Simpson, O.-e. Bodley and R. Oosterbeek, "Ultrashort pulse laser interactions with cortical bone tissue for

applications in orthopaedic surgery," in *Frontiers in Ultrafast Optics: Biomedical, Scientific, and Industrial Applications Xv*, vol. 9355. International Society for Optics and Photonics, 2015, p. 935508.
16. A. Fuchs, M. Schultz, A. Krüger, D. Kundrat, J. D. Diaz and T. Ortmaier, "Online measurement and evaluation of the er: Yag laser ablation process using an integrated oct system," *Biomedical Engineering/Biomedizinische Technik*, vol. 57, no. SI-1 Track-H, pp. 434–437, 2012.
17. O. M. Carrasco-Zevallos, C. Viehland, B. Keller, M. Draelos, A. N. Kuo, C. A. Toth and J. A. Izatt, "Review of intraoperative optical coherence tomography: technology and applications," *Biomedical optics express*, vol. 8, no. 3, pp. 1607–1637, 2017.
18. M. Wojtkowski, "High-speed optical coherence tomography: basics and applications," *Applied optics*, vol. 49, no. 16, pp. D30–D61, 2010.
19. Y. Zhang, T. Pfeiffer, M. Weller, W. Wieser, R. Huber, J. Raczkowsky, J. Schipper, H. Wörn and T. Klenzner, "Optical coherence tomography guided laser cochleostomy: Towards the accuracy on tens of micrometer scale," *BioMed research international*, vol. 2014, 2014.
20. L. Iafolla, L. Witthauer, A. Zam, G. Rauter and P. C. Cattin, "Proof of principle of a novel angular sensor concept for tracking systems," *Sensors and Actuators A: Physical*, 2018. [Online]. Available: http://www.sciencedirect.com/science/article/pii/S0924424718302462.
21. S. M. Roodsari, L. Witthauer, L. Iafolla, G. Rauter, A. Zam and P. C. Cattin, "Temperature-compensated fbg-based 3d shape sensor using single-mode fibers," in *Specialty Optical Fibers*. Optical Society of America, 2018, pp. JTu6C–1.
22. I. Susic, P. Cattin, A. Zam and G. Rauter, "Versatile, force range-adjustable, tri-axial force sensor with integrated micro camera for the tip of endoscopic devices," in *Proceedings of The Hamlyn Symposium on Medical Robotics*. Imperial College London and the Royal Geographical Society, 2018, pp. 21–22.
23. I. Susic, A. Zam, P. Cattin and G. Rauter, "Enabling minimal invasive palpation in flexible robotic endoscopes," in *International Workshop on Medical and Service Robots*. Springer, 2018, pp. 64–71.
24. I. Susic and G. Rauter, "Tri-axial force sensor," Switzerland patent Swiss Patent Application LSP P5572EP00, 6 22, 2018.
25. H. Abbasi, G. Rauter, R. Guzman, P. C. Cattin and A. Zam, "Laser-induced breakdown spectroscopy as a potential tool for autocarbonization detection in laserosteotomy," *Journal of biomedical optics*, vol. 23, no. 7, p. 071206, 2018.
26. H. Abbasi, G. Rauter, R. Guzman, P. C. Cattin and A. Zam, "Differentiation of femur bone from surrounding soft tissue using laser induced breakdown spectroscopy as a feedback system for smart laserosteotomy," in *Biophotonics: Photonic Solutions for Better Health Care VI*, vol. 10685. International Society for Optics and Photonics, 2018, p. 1068519.
27. H. N. Kenhagho, G. Rauter, R. Guzman, P. C. Cattin and A. Zam, "Comparison of acoustic shock waves generated by micro and nanosecond lasers for a smart laser surgery system," in *Advanced Biomedical and Clinical Diagnostic and Surgical Guidance Systems XVI*, vol. 10484. International Society for Optics and Photonics, 2018, p. 104840P.
28. H. N. Kenhagho, G. Rauter, R. Guzman, P. C. Cattin and A. Zam, "Optoacoustic tissue differentiation using a Mach-Zehnder interferometer: Preliminary results," in *accepted to be published in IEEE International Ultrasonics Symposium (IUS)*. IEEE Ultrasonics, Ferroelectrics, and Frequency Control Society, 2018.

Bionotes

Lina M. Beltran Bernal
BLOG, Department of Biomedical Engineering, University of Basel, Allschwil, Switzerland
lina.beltran@unibas.ch

Lina Beltrán is a PhD student, her current project is the optimization of the laser system for ablating bone and the fiber system that should be used to achieve endoscopic laser surgery. The optimization also includes the irrigation conditions to improve ablation efficiency without carbonization.

Iris T. Schmidt
BLOG, Department of Biomedical Engineering, University of Basel, Allschwil, Switzerland
iris.schmidt@unibas.ch

Iris Schmidt graduated in Physical Energy and Measurement Technology from Vienna University of Technology in 2016. She is a PhD student in the BLOG, at the DBE, University of Basel. Her main research interest is in developing an optical coherence tomography system for a smart laser surgery system.

Nikola Vulin
Department of Orthopaedics, University of Zurich, Institute for Biomechanics, ETH Zurich, Zurich, Switzerland
nvulin@student.ethz.ch

Nikola Vulin finished his bachelor studies in Mechanical Engineering and continues studying Robotics, System and Control. Nikola is interested in challenging, multidisciplinary topics, where engineering meets biomedical research.

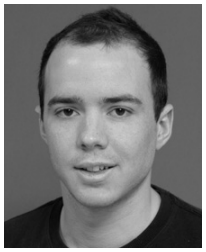

Jonas Widmer
Department of Orthopaedics, University of Zurich, Institute for Biomechanics, ETH Zurich, Zurich, Switzerland
jonas.widmer@hest.ethz.ch

Jonas Widmer is PhD student with a mechanical engineering background working in the field of spine surgery. Currently working on the development of a fully automatic pipeline to perform biomechanical simulations of spine interventions.

Jess G. Snedeker
Department of Orthopaedics, University of Zurich, Institute for Biomechanics, ETH Zurich, Zurich, Switzerland
jess.snedeker@hest.ethz.ch

Jess G. Snedeker was born in the USA. He studied Mechanical and Bioengineering in the USA, and obtained his PhD in Mechanical Engineering from ETH Zurich. In 2006 he became Asst. Prof. and Assoc. Prof. of Orthopedic Biomechanics at ETH Zurich and the University of Zurich, Zurich, Switzerland in 2011.

Philippe C. Cattin
CIAN, Department of Biomedical Engineering, University of Basel, Allschwil, Switzerland
philippe.cattin@unibas.ch

Philippe C. Cattin was born in Switzerland and received his Ph.D. degree 2003 in robotics from ETH Zurich. In 2007 he became an Asst. Professor at the University of Basel and was promoted Assoc. Professor in 2015. Currently he heads the Department of Biomedical Engineering at the University of Basel.

Azhar Zam
BLOG, Department of Biomedical Engineering, University of Basel, Allschwil, Switzerland
azhar.zam@unibas.ch

Azhar Zam received his PhD in Advanced Optical Technologies from University of Erlangen-Nuremberg, Germany. He is an Assistant Professor at DBE, University of Basel. His main interests are Smart Laser Surgery and Therapy, Optical Coherence Tomography (OCT) and Biomedical Spectroscopy and Imaging.

Georg Rauter
BIROMED-Lab, Department of Biomedical Engineering, University of Basel, Allschwil and Sensory-Motor Systems Lab, ETH Zurich and Spinal Cord Injury Center, University Hospital Balgrist, Zurich, Switzerland
georg.rauter@unibas.ch

Georg Rauter studied Mechanical Engineering at TU-Graz and Mathematical and Mechanical Modeling at MATMECA, Bordeaux. In 2014 he received his PhD in robotics from ETH Zurich. Since 2016 he heads the BIROMED-Lab as Asst. Prof. for Medical Robotics and Mechatronics at the DBE, University of Basel.

Chapter 5

Optimizing Er:YAG laser for deep bone ablation

The publication in this chapter documents the optimization of our Er:YAG laser, paired with a novel irrigation system consisting of a microjet of water measuring 50 μm in diameter for deep bone ablation. The goal of optimization was to prevent tissue carbonization by using an infrared camera to control the surface temperature of the bone, so that water would irrigate the tissue just before carbonization began. In addition, the accumulation of water and debris inside the ablated area was partially prevented by constantly removing them during ablation by means of pressurized air. We estimated the limitations of our laser system by calculating beam propagation and by using information about the ablation depth obtained from *one pulse ablation*. Calculated this way, the maximum ablation depth would be 30 mm, however we achieved a depth of 21 mm as the feedback system was based on the surface temperature of the bone. Furthermore, accumulated water and debris were not completely removed. Since one of the main limitations of our laser is the beam quality factor M^2, we also calculated a theoretical achievable depth for different M^2 during 300 s, and showed the importance of improving the beam quality. The laser beam parameters, i.e., energy, repetition rate, and beam size, were also evaluated in the course of the optimization process.

Publication: Lina M. Beltrán Bernal, Ferda Canbaz, Antoine Droneau, Niklaus F. Friederich, Philippe C. Cattin, and Azhar Zam, "Optimizing deep bone ablation by means of a microsecond Er:YAG laser and a novel microjet irrigation system", Biomed. Opt. Express 11, 7253-7272 (2020).
DOI: https://doi.org/10.1364/BOE.408914

Research Article | Vol. 11, No. 12 / 1 December 2020 / Biomedical Optics Express 7253
Biomedical Optics EXPRESS

Optimizing deep bone ablation by means of a microsecond Er:YAG laser and a novel water microjet irrigation system

LINA M. BELTRÁN BERNAL,[1,5] FERDA CANBAZ,[1] ANTOINE DRONEAU,[2] NIKLAUS F. FRIEDERICH,[3] PHILIPPE C. CATTIN,[4] AND AZHAR ZAM[1,6]

[1]*Biomedical Laser and Optics Group (BLOG), Department of Biomedical Engineering, University of Basel, CH-4123 Allschwil, Switzerland*
[2]*Grenoble INP; Grenoble Alpes University, Phelma, France*
[3]*Center of Biomechanics and Biocalorimetry (COB), Department of Biomedical Engineering, University of Basel, CH-4123 Allschwil, Switzerland*
[4]*Center for Medical Image Analysis and Navigation (CIAN), Department of Biomedical Engineering, University of Basel, CH-4123 Allschwil, Switzerland*
[5]*lina.beltran@unibas.ch*
[6]*azhar.zam@unibas.ch*

Abstract: The microsecond Er:YAG pulsed laser with a wavelength of $\lambda = 2.94$ μm has been widely used in the medical field, particularly for ablating dental tissues. Since bone and dental tissues have similar compositions, consisting of mineralized and rigid structures, the Er:YAG laser represents a promising tool for laserosteotomy applications. In this study, we explored the use of the Er:YAG laser for deep bone ablation, in an attempt to optimize its performance and identify its limitations. Tissue irrigation and the laser settings were optimized independently. We propose an automated irrigation feedback system capable of recognizing the temperature of the tissue and delivering water accordingly. The irrigation system used consists of a thin 50 μm diameter water jet. The water jet was able to penetrate deep into the crater during ablation, with a laminar flow length of 15 cm, ensuring the irrigation of deeper layers unreachable by conventional spray systems. Once the irrigation was optimized, ablation was considered independently of the irrigation water. In this way, we could better understand and adjust the laser parameters to suit our needs. We obtained line cuts as deep as 21 mm without causing any visible thermal damage to the surrounding tissue. The automated experimental setup proposed here has the potential to support deeper and faster ablation in laserosteotomy applications.

1. Introduction

As in ancient times, present-day bone surgery still depends mainly on mechanical tools, such as different types of oscillating saws or burs [1,2]. The main drawback of using such tools is the extent of mechanical stress they cause, leading to collateral (sometimes irreversible) damage in patients; as a result, the healing process can be delayed or the patient's life may change drastically [3]. Likewise, the bio-compatibility and degree of contamination of conventional tools pose a high risk of infection to patients. Because conventional tools are still made of metal, corrosion and wear resistance have to be evaluated and minimized. Conventional tool use also limits the surgeon's ability to achieve functional cutting shapes. Several studies have shown the value of using lasers to ablate bone, instead of mechanical tools [4–10]. Lasers can make contactless cuts, thereby negating any problems arising from mechanical stress. Furthermore, the laser's contact-free interaction with tissues offers greater safety during surgical procedures. Only the cover structure of the laser needs to be evaluated for bio-compatibility and various materials exist

#408914 https://doi.org/10.1364/BOE.408914
Journal © 2020 Received 1 Sep 2020; revised 3 Nov 2020; accepted 3 Nov 2020; published 19 Nov 2020

Biomedical Optics EXPRESS

which are both 100 % bio-compatible and suitable for enclosing a laser. By controlling the laser with robot-assisted technology, highly precise and functional cuts become possible [11].

Initial studies of laser ablation of hard tissue started in the field of dentistry, in 1965 [12,13]. Since then, dentistry has remained the field best known for ablating hard tissues with lasers, with typical ablation depths of hundreds of micrometers [14–17]. For instance, the frequency-doubled *neodymium yttrium aluminium garnet* (Nd:YAG) laser at $\lambda = 532$ nm has been used for caries prevention in enamel [18]. Lasers like the *carbon dioxide* (CO_2) at $\lambda = 9.3$ μm, *erbium-dopped yttrium aluminium garnet* (Er:YAG) at $\lambda = 2.94$ μm, or *erbium-chromium-doped yttrium-scandium-gallium garnet* (Er,Cr:YSGG) at $\lambda = 2.78$ μm have been used for removing dentin, enamel, caries, and soft tissue [16,19–21]. Several studies have shown that the microsecond Er:YAG pulsed laser is highly efficient for ablating hard tissue, and one of the infrared lasers that produces the least damage to tissues. The Er:YAG laser has shown superior performance over other mid-infrared lasers like Er:YSGG, Nd:YAG, Ho:YSGG, CO_2, and Ho:YAG [5,11,17,22–24]. Studies have shown using Er:YAG to be safe for bone ablation even at very high energies of 1 J, in-vivo human laser osteotomy and histology analyses are in [25], other in vivo studies are in [9,11]. In a previous study using SEM images to detect mechanical damage, no fracture or cracks were found at high energies of 940 mJ and fluence of 433 J/cm^2 [26].

The primary ablation mechanism for microsecond lasers operating in the mid-infrared region is *photothermal ablation [27]*. In photothermal ablation, the water molecules present in the tissue vaporize when the laser interacts with the tissue, leading to high ablation efficiency. Since both water and hydroxyapatite, two of the main components of bone, have one of their highest absorption peaks near 3 μm [18,28], ablation becomes more efficient when using Er:YAG lasers. Considering the variation among animals and persons, and due to age and pathological differences, it is not possible to determine a unique distribution of the biological components of tissues. However, according to studies that have established consistent and functional classification and distribution for some components, bone consists of approximately 13% water, 27% collagen and 60% hydroxyapatite [29,30]. When the laser impinges the surface of the bone, the tissue heats up and a high pressure of several hundred bars is created on the water molecules located in the interstitial matrix of the bone tissue. The pressure leads to localized microexplosions of the material by vaporization [27,31]. To initiate the process, a certain amount of energy must be applied to the tissue surface. This energy level, called the *ablation threshold*, is the minimum fluence (energy per unit area) required for removal of the material [28].

The high temperatures generated during photothermal ablation of bone cause the remaining tissue to dry out. Several heat effects occur in the tissue as its temperature increases. Soon after the bone starts drying out, carbonization will follow, completely damaging the tissue. Therefore, an irrigation system to re-hydrate and cool down the tissue is needed. For living tissues, the most bio-compatible and convenient irrigation fluid is water; more specifically, Ringer's solution or 0.9 % sodium chloride (NaCl). However, since water has an absorption peak around 3 μm, the water used to irrigate tissues will absorb the energy of the Er:YAG laser as well. If the water is not properly delivered to the tissue, the ablation rate may decrease, either because the water accumulates and blocks the energy of the laser, or because the amount of water is insufficient and the tissue carbonizes [4,17,26].

Another challenge to overcome during laser surgery is the laser's inability to selectively ablate a specific tissue. To protect vital tissues that may come into contact with the laser during the ablation process, a differentiation feedback system is needed. Recent studies have shown that optoacoustic feedback or laser-induced breakdown spectroscopy (LIBS) can be used to differentiate hard bone, soft bone, muscle, and fat [32,33]. To maximize the advantages afforded by a smart laser device and its associated feedback systems, the ability to control the system with a robotic device would provide more efficiency, safety, and the possibility of performing complex surgeries, i.e. minimally invasive surgeries [34,35].

Biomedical Optics EXPRESS

Bone ablation implies heating effects, such as carbonization, when the tissue temperature is above 100 °C. Therefore, the tissue surface may be irrigated to avoid damage to the tissues surrounding the ablated area. However, continuous irrigation of the tissue can reduce the amount of material removed as laser energy is absorbed by the water. In dentistry, the solution is to use a continuous spray to disperse the water over the ablated area [17]. This way, the lasers can make superficial cuts, < 2 mm deep. Water cooling has been studied and found to influence the ablation process, depending on the amount of water applied and the type of irrigation system used [4,17,26]. To optimize the ablation rate of the laser system, one must optimize the laser parameters and the irrigation system used. The optimization process is usually not required for superficial cuts (e.g. caries removal). For deeper cuts (in the order of centimeters), however, it is necessary to optimize all parameters, especially if the laser system is to be adapted to real bone surgery in the future.

In this work, we show the process of optimizing the irrigation system and the Er:YAG laser parameters for deep bone ablation. We investigated the effect of constantly cleaning the laser path (irrigated water, debris produced during ablation, and focusing lens) on the ablation process. We explored the laser's limitations in terms of beam quality and settings (beam spot size, energy, repetition rate) and their influence on ablation performance. Based on the results of one-pulse ablation, we estimated the ablation evolution for more pulses. The ablation process was analyzed for both hole and line ablation. Our investigation shows that the key to harnessing and exploiting the laser's capacity for deep bone ablation can be summarized by three main factors: (1) the use of an automated system that senses the need for irrigation; (2) the use of a high-pressure, thin water jet capable of reaching deep into the crater during ablation while avoiding excess water application; and (3) cleaning the laser's path so that the beam can reach the bone surface without encountering additional absorbing material. We propose a system that fulfills all three factors, thereby ensuring optimal ablation process.

2. Materials and methods

2.1. Laser, irrigation systems, and bone samples

A Syneron Litetouch Er:YAG laser with a wavelength of $\lambda = 2.94\ \mu$m was used for the experiments. The pulse duration and repetition rate of this laser are 100-400 μs and 1-50 Hz, respectively. The maximum average power of the laser is 9 W; the pulse energy and peak power are 10-900 mJ and 0.1-2.25 kW, respectively. To determine the divergence of the laser beam, we focused the beam with a calcium fluoride (CaF_2) lens of focal length f = 75 mm. Then, we measured the beam diameter at different positions along the propagation direction (z) by applying the *knife-edge method* [36]. A hyperbolic function fit of the form $d(x) = \sqrt{a + bx + cx^2}$ [37], where $d(x)$ is the beam size, and a, b, and c are the the fitting parameters, was used to determine several geometrical properties of the laser beam, such as the beam quality factor $M^2 = \frac{\pi}{8\lambda}\sqrt{4ac - b^2}$. We determined that $M^2 = 22$, meaning that the beam diverges $\sqrt{M^2} = 4.7$ times more than an ideal Gaussian beam ($M^2 = 1$). We further determined the spot size of the focused beam and its depth of focus (twice the Rayleigh length) to be $d_0 = 526\ \mu$m and DoF = 6.8 mm, respectively.

Several segmented (approximate dimensions 5 x 3 x 3 cm^3) pig femur bones were bought at a local supermarket, where they were kept in the freezer at -18° C post-mortem. The freshness of the bones is unknown, however, the samples were stored in the freezer at -18° C after purchase, and used within 48 hours. We performed three measurements for each experiment, so the reported results are the corresponding mean values.

Figure 1 shows the schematic of the ablation setup. The Er:YAG laser beam was sent in a horizontal z-direction and focused on the bone surface by means of a CaF_2 lens with focal length f = 75 mm. The bone sample was connected to a holder attached to an xyz-actuation mechanism. Manual yz-actuation was realized using regular micrometer stages (PT1/M - Thorlabs) mounted

Biomedical Optics EXPRESS

perpendicular to each other, while x-actuation was achieved with a motorized stage (DDSM100 - Thorlabs). All stages were kept static for hole ablation experiments; the motorized stage was activated for line ablation experiments only. An irrigation system was used to cool the tissue during ablation, while pressurized air was used to blow debris off of the bone surface. Irrigation feedback was provided by means of an infrared camera; this system will be described in detail in Section 2.3.

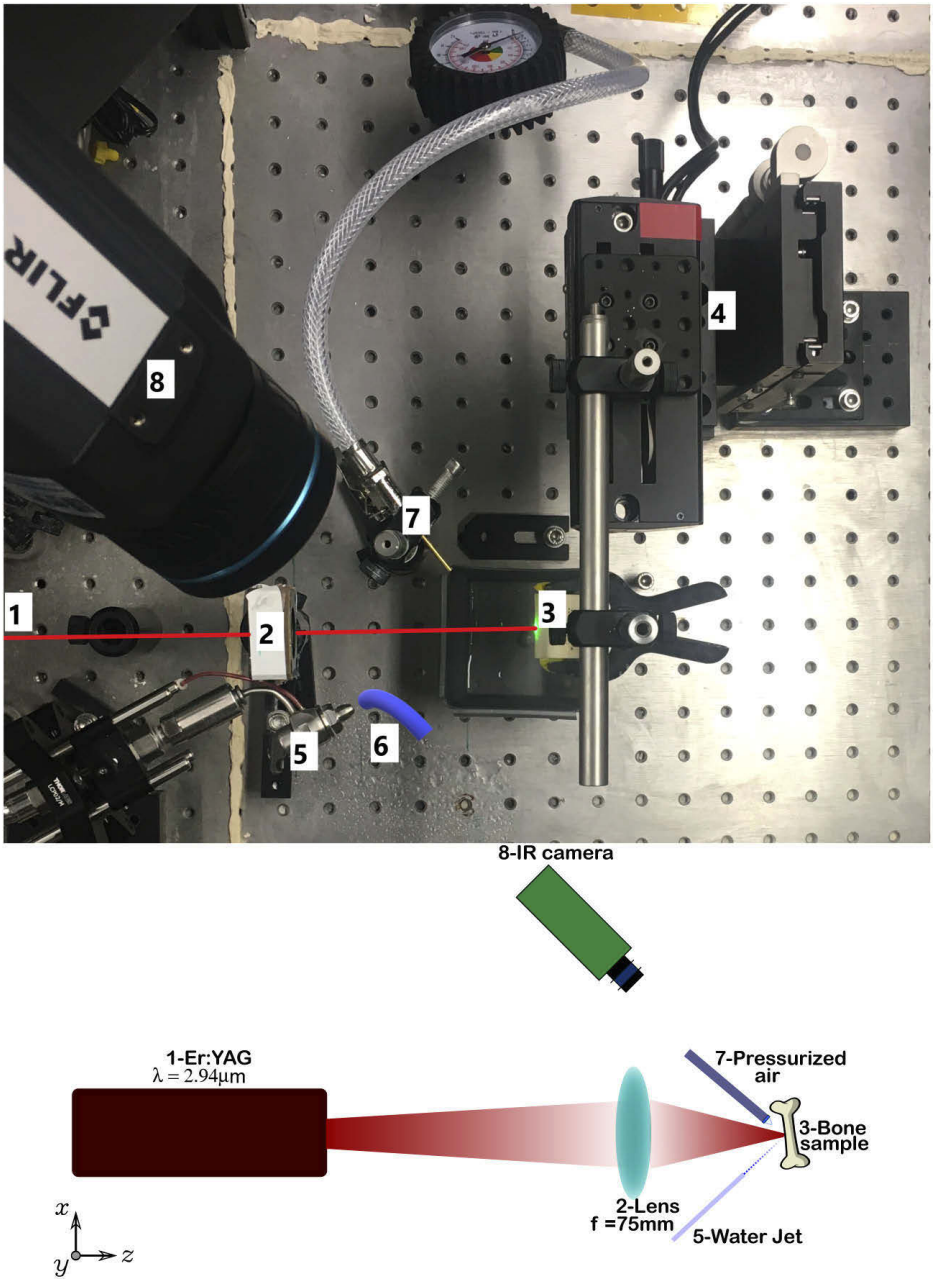

Fig. 1. Photograph (top) and sketch (bottom) of the setup used to ablate bone samples with an Er:YAG laser (1). A lens (2) was used to focus the beam on the sample (3). The sample was mounted on an xyz-actuation mechanism (4). Tubes for the water jet irrigation system (5); for air deviation (6) and for pressurized air (7) are depicted. An IR camera (8) was placed to provide feedback about the sample's superficial temperature.

We compared the performance of two different irrigation systems during the ablation process. The first system was an ESI Elveflow microfluidic system, consisting of a pneumatic pressure

Biomedical Optics EXPRESS

controller and a channel that pumps air to the water reservoir (80 ml capacity). Water is delivered through a tygon tubing coil with an inner diameter of 500 μm, a maximum pressure of 2 bar, and a laminar flow regime of 1 cm long. This system offers the possibility of controlling water delivery through ON and OFF sequences with a time resolution of 0.15 s. At faster switching sequences, the system is unable to deliver water. At constant irrigation, the water flow rate is 14 ml/min. The tygon tube was placed along the *xz*-plane, as close to the bone surface as possible (5 mm, forming 45° angle with the bone surface). The second irrigation system incorporated a novel, specially designed nozzle from Synova Laser MicroJet Technology, which produces a water jet 50 μm in diameter, with 10-800 bar pressure, and a laminar flow regime of length approximately 15 cm. A pump, the Maximator Schweiz AG Pressure Unit 690 bar, ref No. MP030066, was used to deliver water through the nozzle. The pump can continuously deliver pressurized distilled water, up to 690 bar. The Maximator pressure unit has a 10 liter reservoir tank. The water flow rate at 30 bar is 4.8 ml/min. At 30 bar, the thin water jet is very gentle on the soft tissue, and poses no risk of injury. Unlike the ESI system, the Maximator does not possess automated sequence control. To block water delivery, we used air ((6) in Fig. 1) to divert the water jet just enough to keep it away from the ablation area. Here we employed the ESI system to deliver the air at 2 bar by changing its operational modality. The air was delivered whenever irrigation needed to be stopped. To do this, the ESI air tube was placed above the Synova jet so that the air crossed the Synova water jet almost perpendicularly.

We also investigated the effect of using pressurized air to clean the ablated surface and to stop the accumulation of water inside the crater. For this, we applied constant pressurized air to the ablated area at 3 bar in the *xz*-plane (5 mm, forming a 45° angle with the bone surface), opposite to the irrigation system.

2.2. One pulse ablation

Fundamental models for laser ablation using only one laser pulse, such as the *Blow-off model* or the *Steady-state model* are well described by A. Vogel [28]. For the *Blow-off model*, four main conditions must be upheld. First, the distribution of absorbed energy in the tissue should be governed by the Lambert-Beer law $T = \frac{\Phi}{\Phi_i} = e^{-\mu_a l}$, where T is the optical transmission, Φ is the fluence transmitted after the incident fluence Φ_i has traveled through an optical path length l, and μ_a is the absorption coefficient of the material. Second, a threshold fluence Φ_{th} is required to start ablation of the material; fluence values below Φ_{th} only serve to heat the material. Third, material removal starts only after a laser pulse has finished. Fourth, thermal confinement must be fulfilled, which means that the laser's pulse duration τ_p must be smaller than the tissue's thermal diffusion time τ_d. In this way, the energy is confined to the volume that absorbs the radiation. If the energy is distributed over a larger volume, tissue damage may occur. These conditions are fulfilled for lasers with pulse durations of τ_p=100 ns or less. For the *Steady-state model*, three conditions must be upheld. First, a fixed energy density is required to ablate a unit mass of tissue. Second, ablation starts right after the laser pulse begins. Third, a threshold fluence is required to start ablation of the material, just as in the *Blow-off model*. Well above the threshold, the *Steady-state model* predicts a linear dependence between ablation depth and incident fluence; the model is valid for microsecond pulse durations or longer. Some studies [28,38] clearly state that the applicability of either model to a data set of removed material may not be straightforward. For instance, the model that best describes ablation might change depending on the fluence range of the data set. Also, several effects are produced by the debris generated during ablation, such as shielding. This debris affects the absorption coefficient of the material, and is known as plume absorption. In our experiments, we used pressurized air on the surface of the sample to counteract the effect of the debris on the ablation process.

Investigating ablation with one pulse is the first step to analyzing laser ablation. Both *Blow-off* and *Steady-state* models were developed based on a one-pulse ablation process. Ablation with

Biomedical Optics EXPRESS

one pulse provides an understanding of the initial stage of the ablation process. To see the effect of plume formation (debris from the ablation process) on ablation rate [28], we ablated samples both with and without applying pressurized air to the ablation spot. We did not use high-speed photography to observe plume formation, therefore, the extent to which debris was suppressed is unknown. However, we set a 3 bar pressure which allowed for bone ablation without diverting the water jet from the target position.

2.3. Automated feedback system using an IR camera

As a testing method and proof of concept, we monitored the superficial temperature of the sample by means of an IR camera, FLIR A655sc. The camera provides up to 50 fps at full frame 640 x 480 resolution, a spectral range of 7.5 to 14 μm, and an operating temperature range of -40 to 150° C. The camera was placed above the setup forming an angle of approximately 45° to not interfere with other components on the laser ablation path. We used the camera to register temperatures at 50 fps during the ablation process to determine whether the tissue needed irrigation or not. For both hole- and line-ablated shapes, the imaging depth of the camera was very limited, because the size of the craters (<1 mm diameter or width) and due to the position of the camera with respect to the ablation area. Thus, feedback was based on the superficial temperatures measured by the camera, mainly from the tissue surrounding the ablation spot.

While running the Er:YAG laser, the Maximator-Synova system, and the pressurized air (at 3 bar) mechanism on the sample during the experiments, we used LabView to control and synchronize the laser's optical beam shutter (SH1/M - Thorlabs), the ESI pump, the camera recording, and the translation stage movement in x-direction when ablating line shapes.

As a first step in the optimization process, we implemented a mechanism to detect the tissue's superficial temperature and to use this information to control tissue irrigation. To increase the ablation depth, the optimization process was done only in order to avoiding early carbonization. Nevertheless, other important heat effects, like the denaturation of proteins and collagen, occur above 60 °C. Those effects also depend on the exposure time. For instance, in the case of denaturation above 60 °C, the damage becomes irreversible if the exposure time is higher than 6 s [27]. During ablation with a pulsed laser, the tissue undergoes dramatic changes in temperature when irrigation is used in combination with the laser. The heat effects of ablation with pulsed lasers plus irrigation on the tissues are not currently well known and depend on the specific conditions of each experiment [8,39], where, most of the time, damage is detected through histology or scanning electron microscopy (SEM) images. To increase the ablation rate without creating carbonization on the surrounding tissue, we performed several experiments while setting a temperature threshold on the camera. Whenever the tissue temperature reached the threshold value, the irrigation system was activated.

In order to evaluate the automated feedback system and comparing it to other systems, the parameters of the Er:YAG laser were kept constant for all experiments in this section. The energy per pulse was 830 mJ and the repetition rate was 10 Hz. We performed different experiments as follows:

(a) **Automated feedback with jet $\phi = 50\,\mu$m and pressurized air:** we used the Maximator-Synova irrigation system (nozzle diameter $\phi = 50\,\mu$m, at pressure P = 30 bar) as an automated feedback system with the IR camera. We applied constant pressurized air to the sample at 3 bar to clean debris and to blow off the remaining water. An additional air pump of 2 bar was used to divert the jet when irrigation was not needed.

(b) **Automated feedback with jet $\phi = 50\,\mu$m and without pressurized air:** we used the same system as (c) but we did not apply pressurized air to the sample target.

(c) **ON/OFF sequence with jet $\phi = 50\,\mu$m and pressurized air:** we used the ESI irrigation system with the condition (ON and OFF sequence) that we found to be the best in our

Biomedical Optics EXPRESS

previous study [26]. The water cycle sequence had a water ON duration of 0.25 s and a water OFF duration of 0.9 s, giving a total period of 1.15 s. For this experiment, we used the Maximator pump and the Synova nozzle with diameter $\phi = 50\ \mu$m. Since the water pump could not be controlled by ON and OFF sequences, we used 2 bar air from the ESI pump to divert the thin water jet when it had to be OFF. Additionally, we applied constant pressurized air to the sample at 3 bar to clean debris and to blow off the remaining water.

(d) **ON/OFF sequence with jet $\phi = 50\ \mu$m and without pressurized air:** we used the same system as (c) but we did not apply pressurized air to the sample target.

(e) **ON/OFF sequence with ESI jet $\phi = 500\ \mu$m and without pressurized air:** we used the ESI irrigation system with tube diameter $\phi = 500\ \mu$m at pressure P = 2 bar and using the best ON and OFF sequence we identified in [26].

For the ON/OFF sequence with the ESI irrigation system we did not apply pressurized air to the sample surface. Compared to the ESI system's pressure capacity of 2 bar, the available pressurized air was either insufficient for blowing off excess water and debris or too high to divert the entire jet, and therefore exposed the target area to carbonization.

We investigated the performance of the irrigation systems and conditions described above while ablating bone. Line ablation was performed using an optimized lateral speed for ablation according to the results of our previous study [40]. Hence, the motorized stage ran at 8 mm/s along the x-direction during ablation. We made up to 800 iterative line cuts at several y-positions.

2.4. Optical coherence tomography (OCT)

To obtain cross-section images of the ablated holes and lines, we used an optical coherence tomography (OCT) system built in our laboratory. The OCT system has an Axsun swept laser

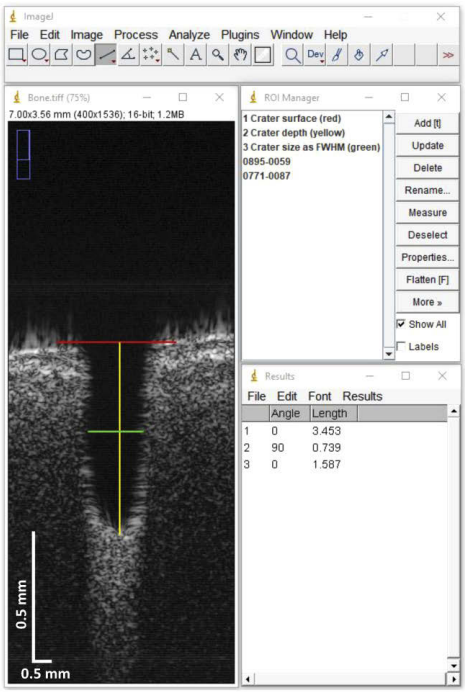

Fig. 2. Example showing manual measurement of the crater depth (yellow vertical line from the crater's deepest point to the surface, depicted with a red horizontal line) and width as the FWHM (green horizontal line) from the OCT image using ImageJ software. In this example, the depth and width were measured as 0.74 and 1.59 mm, respectively.

Biomedical Optics EXPRESS

source with central wavelength $\lambda_0 = 1060$ nm, bandwidth $\Delta\lambda = 100$ nm, and swept rate 100 kHz. The acquired volume size is 7 x 3.56 x 7 mm^3, and the volume rate is 0.37 $\frac{volumes}{s}$. The axial and lateral resolution of the OCT are 11 and 40 μm, respectively. We acquired B-scans with a field of view of 7 mm and imaging depth of 3.56 mm in air. For image analysis, ablation depths and widths were measured by manual segmentation using ImageJ. The measured depth was the distance from the deepest point of the cut to the surface of the sample, and the diameter (width) was the full width at half maximum (FWHM) of the cut. Due to range of depth limitations of the OCT (max. 3.56 mm), the cut profile of deeper craters appears folded in the OCT image. To measure the entire depth of such cuts, we moved the sample in the vertical direction using the translation stage as often as needed until reaching the deepest point of the cut within the image axial range. This procedure did not affect the final depth measurement because the medium was still air inside the crater. Figure 2 shows an example of manual depth measurement of the crater.

3. Results

3.1. One pulse ablation

Figure 3 shows the depth values obtained with only one laser pulse as a function of incident peak fluence. The continuous and the dashed linear fits refer to ablation with constant pressurized air and without air, respectively. The graph shows the results obtained after averaging over 10 measurements for each incident peak fluence, the error bars correspond to the standard deviation for each data point.

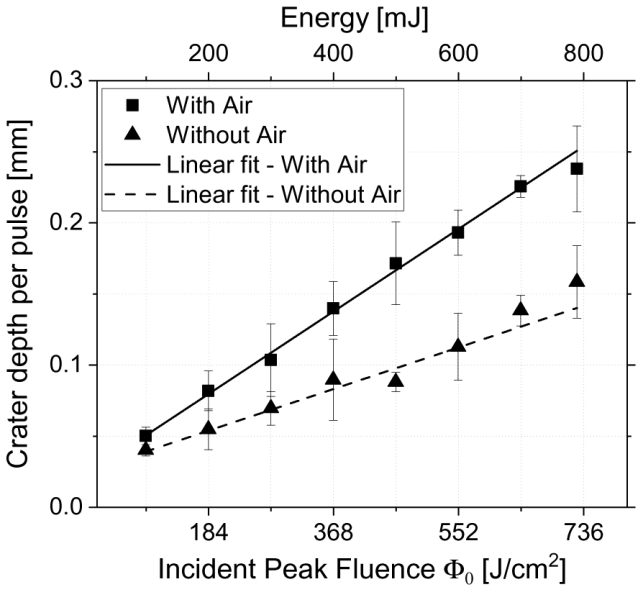

Fig. 3. Variation of depth values as a function of incident peak fluence in one-pulse ablation. The craters were imaged by means of an optical coherence tomography (OCT) system with a lateral and axial resolution of 40 and 11 μm, respectively.

In Fig. 3 the ablation was deeper when pressurized air was applied, meaning that the debris were at least partially blown off. The fitting parameters for the ablated depth l using pressurized air gives the following equation for linear fit:

$$l = \frac{dl}{d\Phi_0}\Phi_0 + c, \tag{1}$$

where Φ_0 is the incident peak fluence and c is the intersection value on the vertical axis. The linear dependence shows a constant ablation efficiency regime ($dl/d\Phi_0$). Based on the experimental

Biomedical Optics EXPRESS

data, the fitting parameters are $dl/d\Phi_0 = 0.0316\,\mathrm{mm}^3/\mathrm{J}$ and $c = 0.02\,\mathrm{mm}$. Equation (1) and its fitting parameters are valid only for the fluence range used. Whenever the fluence range changes, probably other model will describe the phenomena better. Because our measurements are in the high fluence regime and ablation efficiency is constant (linear fit) for one pulse ablation, a *Steady-state model* [28] would predict the ablation evolution when more pulses are applied in the specified fluence regime. Additionally, to estimate the maximum obtainable depth not only in the middle of the cut (as shown in fitting Eq. (1)), but also along the crater at each depth (in the *xy*-plane, *r* in cylindrical coordinates), the fluence applied to the entire *xy*-plane should be estimated. A detailed analysis is presented in Section 3.2.1.

3.2. Automated irrigation feedback system using an IR camera

To automate the irrigation on the ablated tissue, we set a threshold value for which the camera would register the temperature; this was done in a LabView program. To establish a temperature threshold that both provides a high ablation rate and also prevents tissue carbonization, we tested different values in the temperature range of 30-150 °C. The deepest ablation without any visible sign of carbonization was obtained at 104 °C, just above the vaporization temperature of water. At slightly higher threshold temperatures, we observed yellow tones in the areas surrounding the ablated spot, and the ablation was also deeper. For threshold temperatures above 110 °C, the tissue was carbonized (brown and black tones) and the ablation depth decreased as well. The yellowish marks on the tissue indicated an early carbonization stage [26]. Hence, we considered temperatures above 104 °C unsafe for the tissue and set $T_{th} = 104\,^\circ\mathrm{C}$ as the temperature threshold for the experiments (a) and (b), where we utilized an IR camera for feedback (Section 2.3).

3.2.1. Hole ablation

For the experiments (a)-(e), we used different irrigation systems and conditions as described in Section 2.3. The ablation times were in the range of 5-300 s (50-3000 laser pulses). For experiments (c) to (e), we used the sequence of water ON = 0.25 s and OFF = 0.9 s. The *Predicted ablation* as given in Fig. 4(a) was calculated for hole ablation based on the initial depth in fitting Eq. (1), and extended in time according to the number of pulses used. Figure 4(b) shows a comparison of ablation depths from the automated system (experiment (a)) and the calculated cases where the beam quality is improved by lowering its M^2 value. The M^2 values used were 15, 10, 5 and 1, the latter being the ideal Gaussian beam. The beam shape of the Er:YAG laser we used is unknown. Therefore, to calculate the propagation of the beam in *z*-direction, we used the fundamental Gaussian mode TEM_{00} but included the divergence of our beam through its M^2 value, $M^2 = 22$. The fluence distribution $\Phi(r, z)$ along the beam (*r*-direction on the *xy*-plane) is [41]

$$\Phi(r,z) = \Phi_0 \left(\frac{w_0}{w(z)}\right)^2 exp\left(\frac{-2r^2}{w(z)^2}\right), \tag{2}$$

where Φ_0 is the peak fluence of the beam,

$$\Phi_0 = \frac{2E_p}{\pi w_0^2}, \tag{3}$$

w_0 is the beam waist radius at the focal plane, in our case $w_0 = d_0/2 = 263\,\mu\mathrm{m}$, E_p is the pulse energy and

$$w(z) = w_0\sqrt{1 + \left(\frac{z\lambda M^2}{\pi w_0^2}\right)^2} \tag{4}$$

is the beam waist radius of the beam with wavelength $\lambda = 2.94\,\mu\mathrm{m}$ along its propagation direction *z*.

Biomedical Optics EXPRESS

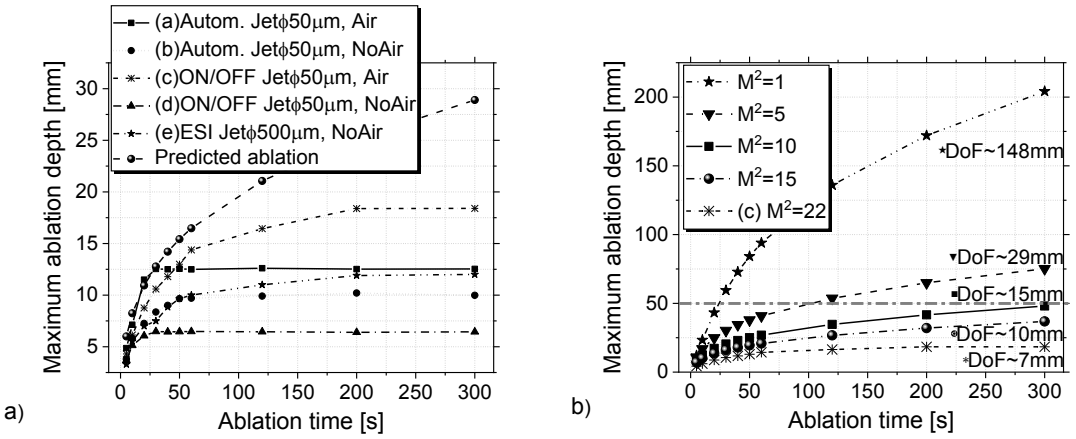

Fig. 4. a) Variation of depth over time for different irrigation systems and conditions. b) Estimated depth variation as beam quality changed from 1 to 15, compared to the ON/OFF condition in a), where the beam quality is 22. The corresponding depth of focus (DoF) decreases from 148 to 7 mm, and is written next to each curve.

After applying the fitting Eq. (1), we obtained an ablated depth for the first pulse with pressurized air at 830 mJ (peak fluence 764 J/cm^2). When replacing Eqs. (4) and (3) in (2), and then in (1), and adding the depth obtained by the first pulse, we obtained the ablated depth for the second pulse, and so on. Hence, the *Predicted ablation* in Fig. 4(a) shows calculations for bone ablation with up to 3000 laser pulses (300 s), based on the first pulse ablation. Registered depth is that of the middle of the cut (the deepest one). Likewise, the ablation evolution shown in Fig. 4(b) was estimated by replacing the different M^2 values in Eq. (4). Hence, the ablation calculation is also based on the first pulse ablation. In Fig. 4(b), the ablation evolution is shown for several M^2 values and compared to the ablation evolution obtained in our experiment using the ON/OFF sequence system for irrigation and pressurized air on the target sample (experiment (c)).

In Fig. 4(a), the *Predicted ablation* overlaps the ablation using the automated feedback system (experiment (a)), up to 30 s ablation, giving a depth of almost 13 mm ± 1 mm. Among the experiments, the automated feedback with air (experiment (a)) yielded the best performance, with up to 13 mm depth. After 50 s, the best performance was achieved by the ON/OFF sequence using the Synova 50 μm diameter nozzle (experiment (c)), the depth at 50 s was 13 mm. The diameter as the FWHM of the cut was approximately constant over time for each experiment. The diameters were greater when pressurized air was used. The smallest one was obtained with experiment (d) as 490 μm ± 30 μm, and the greatest one with experiment (a) as 890 μm ± 20 μm. Figure 4(b) shows an important improvement in ablation depth when beam quality is improved, i.e for M^2 as low as possible. For instance, for a cut 50 mm deep (gray dashed horizontal line), the ideal laser ($M^2 = 1$) would take only 25 s to ablate it, while a laser with $M^2 = 5$ would take 123 s, and a laser with M^2 =10 would take 300 s. Our current laser (M^2 =22) would never reach a deep cut of 50 mm.

3.2.2. Line ablation

In real surgeries, surgeons desire flexible cut shapes (instead of deep holes) that meet the specific requirements of each type of surgery. Hence, experiments with line ablation provide a more realistic situation. To simplify the experiments, we ablated line shapes with a fixed length of 10 mm. We chose the four best performing experiments from the hole ablation investigation; those were (a), (b), (c) and (d). The deepest line ablation achieved was 21 mm ± 2 mm, and it was achieved with the automated feedback system with additional pressurized air on the target sample (experiment (a)). This experiment performed best along the entire range of # lines made

Biomedical Optics EXPRESS

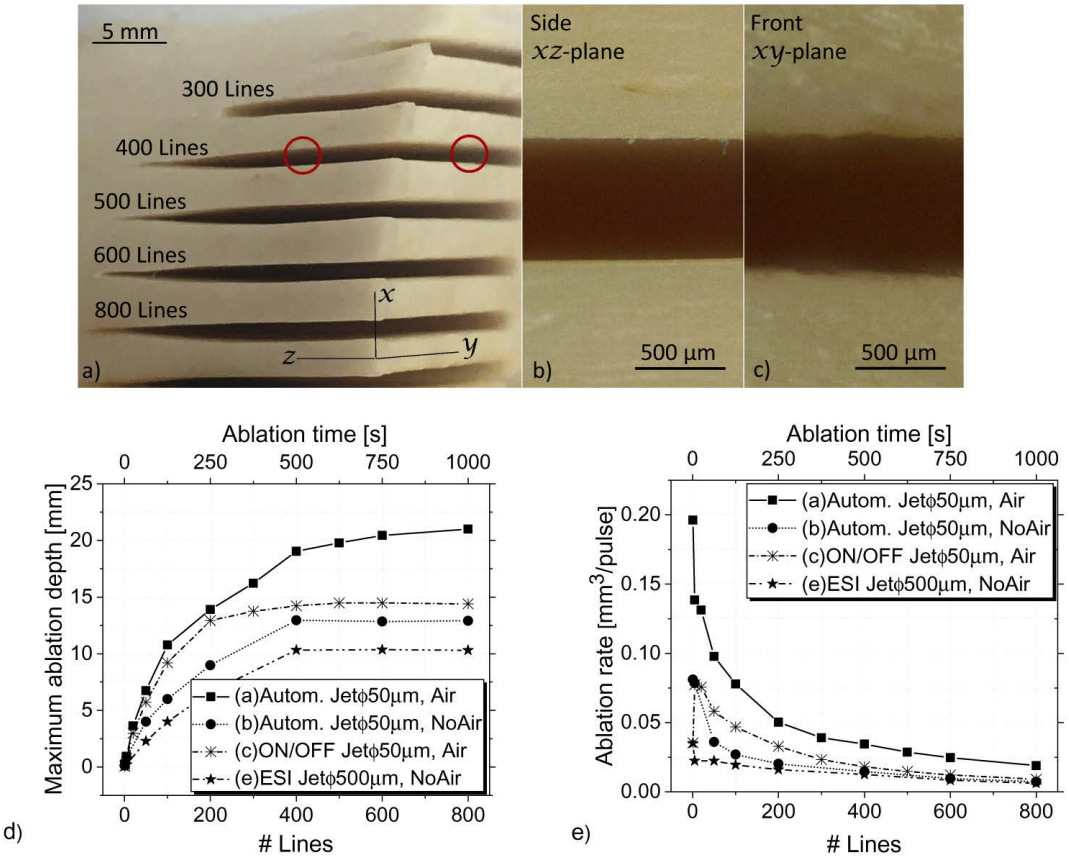

Fig. 5. a) Photograph of a bone showing ablated lines, using the automated irrigation condition for 300-800 iterations. b), c) Microscope images at 189 X, the areas from where they were taken are in red circles in (a). d) Variation of ablated depth over different numbers of repetitive line cuts ablated on the bone surface. e) Variation of ablation rate over repetitive line cuts.

on the bone. It is followed by the ON/OFF sequence, using the Synova 50 μm diameter nozzle and pressurized air as well (experiment (c)). As in hole ablation, the greatest width was obtained when using pressurized air (experiment (a)) as 900 μm ± 100 μm, and the smallest one when pressurized air was not used (experiment (e)) as 610 μm ± 30 μm.

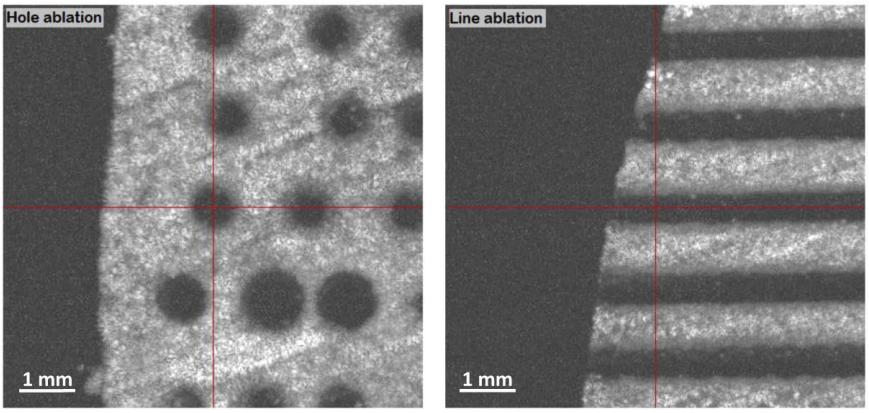

Fig. 6. Example of OCT end-face images of the bone sample for: a) hole ablation and b) line ablation.

Biomedical Optics EXPRESS

The ablation rate was calculated as the ablated volume over the total pulses applied in each number of line cuts (12.5 pulses per line). Since no OCT volumes were acquired, the volume used here is an approximation calculated from the line width as the FWHM of the cut, the total length of the lines (10 mm for all), and the achieved depths for the respective number of line cuts. As seen in Figs. 5(d) and 5(e), the experiments performed without applying pressurized air to the sample show poor ablation performance, while the experiments using the thin Synova nozzle show the best performance.

No fracture or cracks were observed either by eye, OCT, nor microscope, examples can be observed in Figs. 5 and 6.

3.3. Optimal laser settings for bone ablation

Alongside studying beam quality, irrigation system, and conditions for ablating bone, laser parameters, such as pulse energy and average power, should also be optimized. The relation between average power P_{mean}, energy per pulse E_p, and the repetition rate R_r is

$$P_{mean} = E_p \cdot R_r. \tag{5}$$

The beam radius $w_0 = 263\ \mu$m remained constant, the incident peak fluence Φ_0 was estimated using Eq. (3), and the average intensity I_{mean} is

$$I_{mean} = \frac{E_p}{\pi w_0^2} \cdot R_r = \frac{P_{mean}}{\pi w_0^2}, \tag{6}$$

in our experiments, the maximum average intensity was 3.82 kW/cm^2, achieved at pulse energy 830 mJ and repetition rate 10 Hz.

Using the automated feedback system that performed best at fixed laser parameters up to 13 mm depth, we adopted the same temperature threshold determined in Section 3.2 ($T_{th} = 104\ ^\circ$C). We performed two sets of experiments in this section. First, **the number of pulses was fixed at 100**. Second, **ablation duration was fixed at 20 seconds**. For both sets, the laser energy varied in the range of 100-800 mJ (Peak Fluence range 92-736 J/cm^2) at repetition rates of 5, 10 and 20 Hz. These line ablation experiments provide a broader view for understanding the influence of laser parameters, like energy, power, and beam size, on the ablation process. Figure 7 summarizes the results of both sets of experiments.

Figures 7(a) and 7(c) [7(b) and 7(d)] show the variation of depth as a function of energy [average power]. Figures 7(a) and 7(b) show the performance of ablation with 100 pulses. Figures 7(c) and 7(d) show the performance of ablation for a 20 s fixed ablation duration time. Some energy and repetition rate combinations were not possible due to the limitations of the laser, as mentioned in Section 2.1. The maximum average power of the laser is ca. 9 W. The maximum obtainable energy after the optics used is 830 mJ at 10 Hz. For 100 pulses, the minimum ablation depth was 3.2 mm ± 0.4 mm at 100 mJ, and the maximum 7.1 mm ± 0.3 mm at 800 mJ, both at any repetition rate (Fig. 7(a)). For 20 s, the minimum ablation depth was 3.8 mm ± 0.5 mm at 1 W, and the maximum 11.5 mm ± 0.5 mm at 8 W, both at any repetition rate (Fig. 7(d)).

As did the ablation depth, the measured diameters as the FWHM of the cut increased with the energy and average power. The diameter increased from 320 μm ± 10 μm at 100 mJ to 840 μm ± 30 μm at 800 mJ, and from 340 μm ± 40 μm at 1 W to 1000 μm ± 90 μm at 8 W.

Biomedical Optics EXPRESS

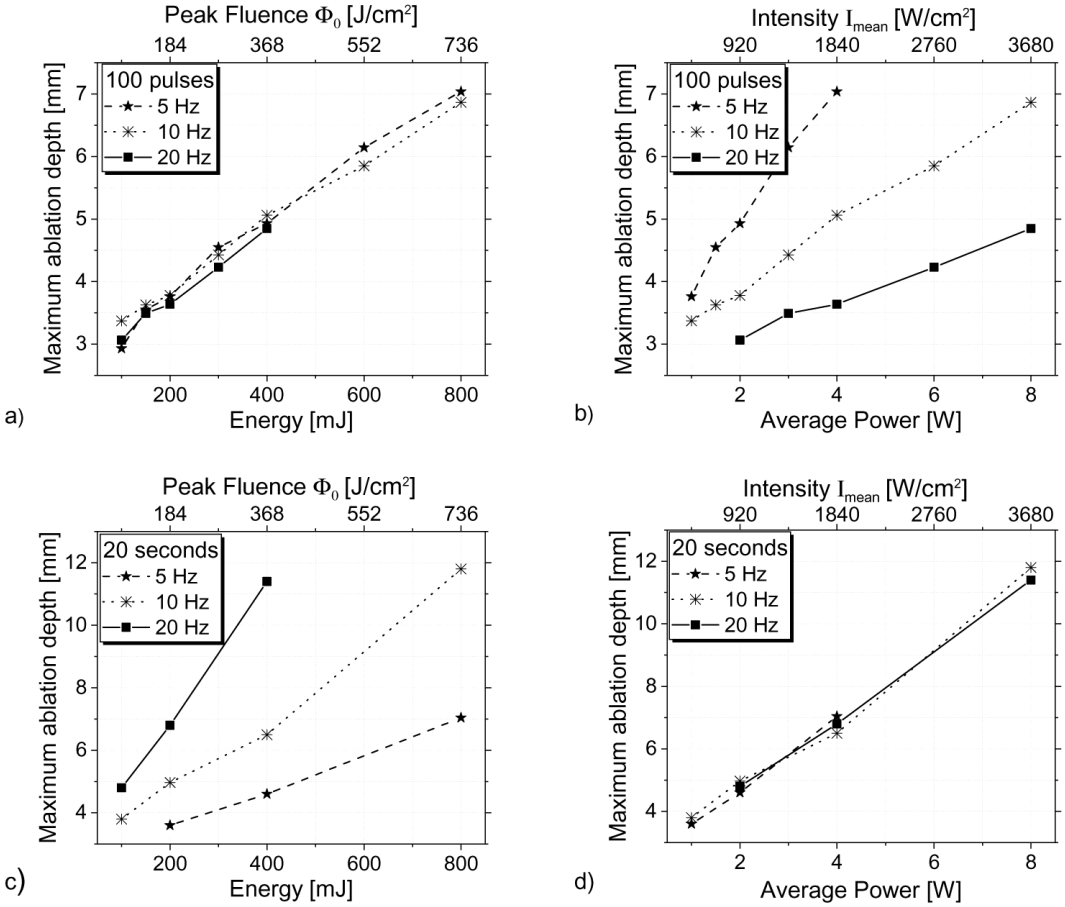

Fig. 7. Variation of depth values measured for: a) 100 pulses, energy range 100-800 mJ, b) 100 pulses, average power range 1-8 W, c) 20-second ablation, energy range 100-800 mJ, and d) 20-second ablation, average power range 1-8 W. For all experiments, repetition rates were 5, 10 and 20 Hz.

4. Discussion

4.1. One pulse ablation

The results from one-pulse ablation experiments can be used to estimate how the ablation will evolve as more pulses are delivered to the tissue. Nevertheless, any prediction must also consider several effects that might affect ablation performance. For instance, during one-pulse ablation, the temperature increase was not considered, though it may affect the absorption characteristics of the tissue. This is part of an accumulative process, where more pulses interact with the tissue. We attempted to compensate for this effect by adding a temperature-based feedback system to properly irrigate the ablated area with water. Another effect that could not be considered during one-pulse ablation was the shielding produced by the debris generated from the ablation process. The shield forms in front of the ablation area, and also absorbs laser energy, thereby disturbing the ablation process. One-pulse ablation was performed both with constant pressurized air at 3 bar and without. As shown in Fig. 3, the air removed at least a portion of the debris, as higher ablation rates were obtained when the pressurized air was applied. Moreover, due to the weakness of the peak fluence as the beam propagates in depth, linear ablation cannot be assumed from the first pulse. Summing up the initial depth several times to calculate the final depth after a certain number of pulses is not accurate. To make the calculation more accurate, we included beam propagation (Eq. (2)) in the z-direction and beam size evolution (Eq. (4)), considering the

Biomedical Optics EXPRESS

divergence of the beam through its M^2 value and the pressurized air case. Still, more can be done to further improve the accuracy of the propagation calculation. For instance, the real intensity distribution of the beam is unknown, and was not considered, so we assumed the fundamental TEM_{00} Gaussian mode in Eq. (2).

The ablation efficiency found from Fig. 3 was obtained for the peak fluence range specified in our experiments. Note that this value can change depending on the fluence range the measurements are, as stated in [28]. Examples of different fluence regimes where other ablation efficiencies are reported are in [42,43]. Additionally, most studies report the measurements calculated using the average fluence, we did it with the peak fluence.

4.2. Automated irrigation feedback system using an IR camera

For ablation optimization, irrigation should be adjusted to each laser setting, like energy or repetition rate. For example, the ON and OFF sequence using the ESI irrigation system in [40] was optimized for energies close to 900 mJ at a 10 Hz repetition rate. This sequence might not work well if it is implemented together with other laser parameters, even if they theoretically yield higher ablation rates. An automated feedback system for irrigating tissue can be easily implemented and adjusted to other laser settings or systems. By maximizing the ablation rate with the automated feedback, the ablation process can therefore be considered independent of irrigation. This process allowed us to proceed with finding the best laser settings, provided that irrigation would adapt to each change in the laser's parameters through temperature detection (see Section 4.3). We determined a temperature threshold value of $T_{th} = 104\,^{\circ}C$; temperatures below T_{th} were considered safe to continue the ablation process without any irrigation on the sample. Temperatures higher than T_{th} were considered unsafe, as the tissue was at risk of carbonization. Hence, once the threshold level was reached, water was delivered to the area of interest to keep the temperature at a safe level.

For this study, the integration time of the camera is 20 ms, much larger than the pulse duration of the laser (max. 400 μs at max. energy per pulse). Therefore, the registered temperature is an average of the real temperature value. For this reason, we do not consider $T_{th} = 104\,^{\circ}C$ as a stated threshold value from now on. This threshold value must depend on the systems used. For using the automated feedback proposed here, a calibration of the system must be always performed to find a proper threshold value.

4.2.1. Hole ablation

When the ON/OFF configuration was used (with both jet sizes 50 and 500 μm), we noticed a yellowish tone in the surrounding areas of the ablated spot, which was also reported by [26]. The pre-carbonized condition (yellowish tone) was present for the ON/OFF sequence because the rising temperature of the bone was never controlled. Since irrigation has a constant delivery rate, it does not adapt to temperature changes of the tissue, making an automated feedback system more important. Furthermore, as mentioned in Section 3.2, for threshold values higher than 104 °C, although the ablation was deeper, the tissue had visible signs of pre-carbonization and carbonization. Therefore, ablation depths can be increased but the drawback is a pre-carbonized area that most likely suffers thermal damage. The severity of the damage is beyond the scope of this work, however, we continued to optimize ablation based on the criterion of not incurring visible damage and ablating as deeply as possible.

As seen in Fig. 4(a), the ablation was always deeper for the conditions using pressurized air, than for the conditions without. We know from Section 3.1 that pressurized air is necessary during one-pulse ablation to blow off the debris. Additionally, when ablating with more pulses, the debris and the irrigation water not only prevent ablation because of the shielding effect, but they also adhere to the lens that focuses the beam. Both phenomena become stronger as ablation progresses, because they are accumulative processes.

Biomedical Optics EXPRESS

The effect of irrigation can be summarized in two stages: less than and more than 40 s ablation. During the first 40 s, the ablation can achieve depths up to 12 mm. As expected, ablation with the automated system (experiment (a)) was deeper than the rest and matched the predicted ablation curve. Similar depths were obtained when using the ON/OFF sequence without pressurized air and the 50 μm nozzle at 30 bar (experiment (d)), and the ESI system with the 500 μm tube at 2 bar (experiment (e)). Nevertheless, after 40 s of ablation, the ON/OFF sequence with the 50 μm nozzle and pressurized air (experiment (c)) yielded deeper holes, but the ablation was saturated. When we observed the samples ablated after 40 s, they were carbonized at the bottom of the cut. This occurred because the camera could only give feedback from the surface of the tissue. Since the irrigation water was frequently running over the surface, its temperature remained below the threshold for longer. Additionally, the pressurized air had already dehydrated the tissue at deeper layers, but there was no feedback about it. This is the main reason why the curve saturates and stops following the predicted ablation curve. In contrast, with automated feedback but no pressurized air on the sample (experiment (b)), carbonization did not occur, but water had accumulated at the bottom of the cut. Both situations describe saturated ablation, see Fig. 4(a) experiments (a) and (b). These results indicate outstanding ablation performance when using an automated feedback system for irrigation. A mechanism for blowing off debris and remaining water, like pressurized air or an extraction system, is necessary. An automated system that can monitor the bone layer by layer during ablation would improve performance further. This information could be provided, for instance, by using phase-sensitive OCT [44].

In Fig. 4(a), the *predicted ablation* and the ablation using the automated feedback (experiment (a)) follow the same tendency up to 30 s ablation. However, there is a discrepancy in the ablation depth. The main reason for this discrepancy is that the real shape of our beam is unknown, and we based our calculation on the ideal Gaussian beam shape. For our laser with $M^2 = 22$, the actual beam should be a combination of different higher order spatial modes. The result is usually a beam with several side lobes that were not considered in our calculation. The accuracy should increase by computing the real shape of the beam.

Figure 4(b) shows the estimated performance of the laser in terms of ablated depth in the case of a well-optimized irrigation system (i.e. no thermal damage and no accumulation of water or debris). We are unable to lower the M^2 value of our laser at present. The best performance of the laser after 30 s (experiment (c) in Fig. 4(b)) is being compared to situations where the quality of the beam would have been improved by changing the M^2 quality factor of the beam, reducing it to $M^2 = 15$, $M^2 = 10$, $M^2 = 5$, and $M^2 = 1$. We observed a great improvement when reducing the quality factor M^2. This information can be used in future to build a more efficient laser capable of ablating deeply and in less time.

4.2.2. Line ablation

Investigating the ablation of shapes is important for evaluating applicability and performance in real bone surgery settings. In our study, we ablated lines using the best four irrigation systems and conditions as determined by the hole ablation experiments, Section 4.2.1. As seen in Fig. 4(a), in the case of line ablation we found that the automated system (experiment (a)) performed best over the entire time window of up to 1000 s. The second best was the ON/OFF sequence condition with pressurized air (experiment (c)). Due to the lack of pressurized air, the automated feedback and the ESI sequential system, experiments (b) and (e), respectively, did not perform as well. Unlike the hole ablation case, the different irrigation systems performed as expected for line ablation. We expected the automated feedback system to communicate with the irrigation system if the tissue was dry or not, and irrigate the bone accordingly. The imaging depth limitation of the camera was present for line ablation as well but the irrigation water was spread and distributed more homogeneously over the line cut during ablation, resulting in a more uniform temperature distribution. Hence, the temperature at the deeper layers of the ablated line was similar to that of

Biomedical Optics EXPRESS

the surface. Temperature information was then processed by the automated system, and irrigation water was delivered accordingly. As shown in Fig. 5(b), we achieved a depth of 19 mm (line length 10 mm) after 400 lines in 500 s (8.33 min). The maximum depth achieved was 21 mm after 800 lines in 1000 s. Of the experimental setups provided, no other irrigation system could improve the laser ablation to reach an equivalent depth. Additionally, as the pressurized air cleaned the laser's path, laser energy was mostly employed for ablation. Far less ablation depth was achieved with the other three irrigation conditions. Their curves achieved a state of saturation, thus, using those systems, deeper ablation could never be reached. Even with the second-best setup (experiment (c)), the laser hardly achieved 15 mm depth after 500 lines and it continued to be saturated. Experiments (b) and (e) reached saturation at 13 and 10 mm, respectively.

During line ablation, the advantages of having a thin water jet of 50 μm at 30 bar pressure instead of the 500 μm at 2 bar jet became clear. The thin jet can reach ablated tissue as deep as 15 cm without losing its compactness, making it ideal for deep ablation. Likewise, its high pressure makes it so robust that it cannot be easily diverted from the ablation area when the pressurized air hits the sample. Only the water that has already been delivered to the tissue is removed by the pressurized air. Therefore, the cooling performance of this thin water jet was exploited to great benefit in this study.

The maximum ablation depth of 21 mm of homogeneous cortical bone reported here exceeds the maximum reported in literature. An Er:YAG laser with average intensity 1.89 kW/cm^2 ablated up to 15 mm depth of combined cortical, cancellous and diseased bone in [25]. An Er:YAG laser was also used for human cadaver mandible osteotomy, reaching a maximum depth of 23 mm of combined cortical and spongy bone [45]. The deepest ablation of cortical bone achieved using a CO_2 laser in [6] was 7.7 mm, with average intensity 83.8 kW/cm^2.

Since the beam gets weaker as it propagates inside the cut, displacing the beam towards the bone might increase the ablation depth. However, for our particular conditions, there is no space available between the pressurized air and the bone, limiting the mobility of the bone towards the beam. Despite displacing the beam can be a solution, in many systems where the displacement in the propagation direction is limited, this would not be possible to do. For instance in endoscopic applications.

A few studies on different optical methods show that carbonization can be detected during the ablation process. For instance, information about thermal expansion of the tissue, detected by phase-sensitive optical coherence tomography (OCT) [44,46], can be used to determine the temperature distribution. In the case of a plasma-generated ablation process, laser-induced breakdown spectroscopy (LIBS) could provide information about the carbonized state [47]. These methods would be potentially more precise for pre-carbonization detection as feedback from the tissue is provided layer-by-layer, not only superficially. These methods, however, demand profound investigation before they could be applied rigorously to our study. Additionally, robust systems would have to be adapted to the current ablation setup.

4.3. Optimal laser settings for bone ablation

Figure 7(a) shows the depth obtained with 100 pulses, while varying the energy of the laser at different repetition rates. At any fixed energy position, the ablation was almost the same, independent of the repetition rate of the laser. In Fig. 7(b), at first, it seems like increasing the average power by increasing the energy and decreasing the repetition rate is enough to provide deeper ablation. However, when the ablation time is fixed, i.e. 20 s, it is possible to determine how the ablation can be increased over time. In Fig. 7(c), at any fixed energy position, ablation is deeper at higher repetition rates. Figure 7(d) shows that at any fixed position of average power, ablation is the same, and only increases when increasing both the energy and the repetition rate.

To the best of our knowledge, the optimal combination of laser parameters (beam quality, beam size, energy, and repetition rate) for deep ablation of bone, has not yet been discussed in

Biomedical Optics EXPRESS

the literature. Some authors report on the performance of lasers for superficial ablation (few mm deep) [6,17,48], and some others report on the thermal damage to tissues [8,39,49]. As suggested by the results of this work, exploring ways to achieve deeper ablation implies a more profound study of irrigation systems and the optimal combination of laser parameters. Energy and average power are often studied separately. For instance, it is well known that increasing the energy at a fixed repetition rate increases ablation. In [15], the maximum ablation depth of enamel and dentin was achieved at a maximum energy of 400 mJ and a repetition rate of 2 Hz (average power 0.8 W). Other studies show that when average power is high (13.8 W), the repetition rate is high (200 Hz) and energy is relatively low (69 mJ) [24], bone ablation depth increases as well. It is not obvious which combination of laser parameters will provide deeper ablation. One reason for this is that the same average power can be obtained by different combinations of energy and repetition rates ($P_{mean} = E_p \cdot R_r$). The second reason is because of the shielding effect provoked by excess water and debris on the beam path. A slower repetition rate results in less accumulation of debris on the beam path between one pulse and another [50]. Nevertheless, we managed to evade the shielding effect up until a certain depth. Thus, it is now possible to study the ablation process dependent on the laser parameters only, when using the automated system with pressurized air up to a depth at which it is considered to work well (12 mm). Ablation now depends on which parameter has a greater impact on the ablation rate: the energy, repetition rate, or average power. According to our results (see Fig. 7), the deepest possible ablation is achieved by increasing the average intensity. Thus, the energy and repetition rate should be increased, while the beam size should be decreased (Eq. (6)). However, increasing the average intensity by decreasing the spot size will result in faster divergence (decrease in depth of focus), leading to superficial ablation only. A careful balance between spot size and depth of focus of the beam is required. The ablation depth will depend on how fast the peak fluence Φ_0 decreases along the depth until it reaches the ablation threshold value Φ_{th}. Φ_0 approaches Φ_{th} faster when the depth of focus (DoF) is shorter. Then, it is also important to calculate ablation depth progress using the geometric parameters of the beam, like beam quality M^2, beam radius w_0 and even beam shape $\Phi(r, x)$ (Eqs. (1)–(4)). Additionally, thermal damage can be avoided by setting the correct repetition rate. The repetition rate of the laser must not exceed approximately $(10 \cdot T_d)^{-1}$, where T_d is the thermal diffusion time; $T_d = D_z^2/4\alpha$ [50], where D_z is the thickness of the damage zone, and α is the thermal diffusivity of the tissue. For human cortical bone, the thermal diffusivity was found to be 0.1461 mm^2/s and for bovine cortical bone 0.2264 mm^2/s [51]. For Er:YAG laser with typical pulse duration of hundred microseconds, the damage zone of bone reported is up to 15 μm [22,39,52]. Thus, the maximum repetition rate that can be set is approximately 260 Hz for human cortical bone and 400 Hz for bovine cortical bone.

5. Conclusion

The study of bone ablation using a microsecond Er:YAG laser was performed by exploring and analyzing different aspects that contribute to optimizing the ablation process. First, the result of the one-pulse ablation experiment was used to estimate the ablation process after the application of several pulses. In this estimation, we also considered the laser's characteristics, such as incident fluence, divergence, and beam spot size. Experimentally obtained ablation results, using different irrigation systems and conditions, were compared to the estimated ones. This comparison was useful for understanding the limitations of the systems used in the experiments. For instance, the ablated depth obtained with the automated system (experiment (a)) and the calculated depth followed the same path until saturation started. Saturation (see Fig. 4) occurred at the point where the bottom of the crater started to carbonize. The carbonization was due to temperatures exceeding the threshold temperature we found $T_{th} = 104\,^{\circ}C$. At this point, the limitation of the IR camera to detect only superficial temperatures was revealed. The need for an appropriate automated system became clear, as well. With further information from experiments focused

Biomedical Optics EXPRESS

on thermal damage to the tissue, the ablation process could be easily adjusted by changing the temperature threshold in the software. However, by implementing a system that is able to detect a pre-carbonized state, layer by layer, and deeper as the ablation progresses, the feedback will be more precise and the ablation will go deeper and faster.

A thin water jet of 50 μm at 30 bar pressure was very convenient for deep ablation. The jet could deliver water deep into the ablated tissue, cooling the entire ablated area. Provided that pressurized air or a suction system is also used to blow off the debris and excess water, the ablation will be optimized. This fact was especially visible for line ablation (see Fig. 5(b)) in our study. The maximum ablation depth was obtained while using the automated feedback system with a thin water jet and applying pressurized air to the sample. The maximum depth obtained was approximately 20 mm, already considered deep ablation for bone. To optimize the laser settings for bone ablation, the automated feedback system was used to ablate within the range where it was working properly (depths below 12 mm). Besides correcting for thermal damage that can occur due to high temperatures on the tissue and other phenomena that could drop the quality of ablation, the most efficient way to optimize the laser parameters is to look at the average intensity of the beam. Increasing the average intensity may guarantee high ablation rate. As observed in Fig. 7(b), for a fixed ablation time, the ablation is the same when the average intensity remains constant and both the repetition rate and the energy of the laser change. Thus, maximizing average intensity using any combination of energy and repetition rate will maximize the ablation rate as well. In principle, the beam size should be decreased. Nevertheless, if the objective is to ablate deep in the bone, there is a trade-off between the size and the average intensity of the beam. If the beam size of the laser is fixed, as it was in our case, the optimization parameter (average intensity) is simplified as the average power of the beam (see Fig. 7(b)). The drawback of choosing very high repetition rates is that the automated irrigation feedback system must be fast enough to detect fast temperature changes on the tissue and that it might lead to thermal damage if not set correctly.

Funding

Werner Siemens Foundation through the Minimally Invasive Robot-Assisted Computer-guided LaserosteotomE (MIRACLE project).

Acknowledgments

The authors gratefully acknowledge Dr. Sara Freund and Mr. Lucas Lang for their great contribution designing and providing us the powerful Maximator pump, Synova S.A. for providing thin water jet nozzle, and Mr. Yakub Bayhaqi for providing support for the use of the OCT system.

Disclosures

The authors declare no conflicts of interest.

References

1. C. Lawrence, "The evolution of surgical instruments: An illustrated history from ancient times to the twentieth century," Bull. Hist. Med. **81**(3), 661–662 (2007).
2. Z. Chen, C. Wang, W. Jiang, N. Tang, and B. Chen, "A review on surgical instruments of knee arthroscopic debridement and total hip arthroplasty," Procedia CIRP **65**, 291–298 (2017).
3. A. R. Eriksson, T. Albrektsson, and B. Albrektsson, "Heat caused by drilling cortical bone: temperature measured in vivo in patients and animals," Acta Orthop. Scand. **55**(6), 629–631 (1984).
4. S. R. Visuri, J. T. Walsh, and H. A. Wigdor, "Erbium laser ablation of dental hard tissue: effect of water cooling," Lasers Surg. Med. **18**(3), 294–300 (1996).

Biomedical Optics EXPRESS

5. K. Stock, R. Hibst, and U. Keller, "Comparison of er:yag and er:ysgg laser ablation of dental hard tissues," in *Medical Applications of Lasers in Dermatology, Ophthalmology, Dentistry, and Endoscopy*, vol. 3192 (International Society for Optics and Photonics, 1997), pp. 88–96.
6. M. Werner, M. Klasing, M. Ivanenko, D. Harbecke, H. Steigerwald, and P. Hering, "Co2 laser free-form processing of hard tissue," in *European Conference on Biomedical Optics* (Optical Society of America, 2007), p. 66321_1.
7. K. Stock, H. Wurm, and F. Hausladen, "Primary investigations on the potential of a novel diode pumped er:yag laser system for middle ear surgery," in *Photonic Therapeutics and Diagnostics XII*, vol. 9689 (International Society for Optics and Photonics, 2016), pp. 96892K.
8. N. Jowett, W. Wöllmer, R. Reimer, J. Zustin, U. Schumacher, P. W. Wiseman, A. M. Mlynarek, A. Böttcher, C. V. Dalchow, and B. B. Lörinczet al., "Bone ablation without thermal or acoustic mechanical injury via a novel picosecond infrared laser (pirl)," Otolaryngol.–Head Neck Surg. **150**(3), 385–393 (2014).
9. K.-w. Baek, W. Deibel, D. Marinov, M. Griessen, M. Dard, A. Bruno, H.-F. Zeilhofer, P. Cattin, and P. Juergens, "A comparative investigation of bone surface after cutting with mechanical tools and er:yag laser," Lasers Surg. Med. **47**(5), 426–432 (2015).
10. M. Papadaki, A. Doukas, W. A. Farinelli, L. Kaban, and M. Troulis, "Vertical ramus osteotomy with er:yag laser: a feasibility study," Int. J. Oral Surg. **36**(12), 1193–1197 (2007).
11. K.-W. Baek, W. Deibel, D. Marinov, M. Griessen, A. Bruno, H.-F. Zeilhofer, P. Cattin, and P. Juergens, "Clinical applicability of robot-guided contact-free laser osteotomy in cranio-maxillo-facial surgery: in-vitro simulation and in-vivo surgery in minipig mandibles," Br. J. Oral. Maxillofac. Surg. **53**(10), 976–981 (2015).
12. R. Taylor, G. Shklar, and F. Roeber, "The effects of laser radiation on teeth, dental pulp, and oral mucosa of experimental animals," Oral Surg., Oral Med., Oral Pathol. **19**(6), 786–795 (1965).
13. L. Goldman, J. A. Gray, J. Goldman, B. Goldman, and R. Meyer, "Effect of laser beam impacts on teeth," J. Am. Dent. Assoc., JADA **70**(3), 601–606 (1965).
14. R. H. Stern and R. F. Sognnaes, "Laser inhibition of dental caries suggested by first tests in vivo," J. Am. Dent. Assoc., JADA **85**(5), 1087–1090 (1972).
15. M. Hossain, Y. Nakamura, Y. Yamada, Y. Kimura, G. Yuichi, and K. Matsumoto, "Ablation depths and morphological changes in human enamel and dentin after er:yag laser irradiation with or without water mist," Photomed. Laser Surg. **17**(3), 105–109 (1999).
16. S. Assa, S. Meyer, and D. Fried, "Ablation of dental hard tissues with a microsecond pulsed carbon dioxide laser operating at 9.3-μm with an integrated scanner," in *Lasers in dentistry XIV*, vol. 6843 (International Society for Optics and Photonics, 2008), pp. 684308.
17. L. Kuščer and J. Diaci, "Measurements of erbium laser-ablation efficiency in hard dental tissues under different water cooling conditions," J. Biomed. Opt. **18**(10), 108002 (2013).
18. P. Ana, L. Bachmann, and D. Zezell, "Lasers effects on enamel for caries prevention," Laser Phys. **16**(5), 865–875 (2006).
19. R. Hibst and U. Keller, "Experimental studies of the application of the er:yag laser on dental hard substances: I. measurement of the ablation rate," Lasers Surg. Med. **9**(4), 338–344 (1989).
20. U. Keller and R. Hibst, "Experimental studies of the application of the er:yag laser on dental hard substances: Ii. light microscopic and sem investigations," Lasers Surg. Med. **9**(4), 345–351 (1989).
21. M. Hossain, Y. Nakamura, Y. Yamada, Y. Kimura, N. Matsumoto, and K. Matsumoto, "Effects of er, cr:ysgg laser irradiation in human enamel and dentin: ablation and morphological studies," Photomed. Laser Surg. **17**(4), 155–159 (1999).
22. R. C. Nuss, R. L. Fabian, R. Sarkar, and C. A. Puliafito, "Infrared laser bone ablation," Lasers Surg. Med. **8**(4), 381–391 (1988).
23. A. Charlton, M. Dickinson, T. King, and A. Freemont, "Erbium-yag and holmium-yag laser ablation of bone," Lasers Med. Sci. **5**(4), 365–373 (1990).
24. K. Stock, R. Diebolder, F. Hausladen, and R. Hibst, "Efficient bone cutting with the novel diode pumped er:yag laser system: in vitro investigation and optimization of the treatment parameters," in *Photonic Therapeutics and Diagnostics X*, vol. 8926 (International Society for Optics and Photonics, 2014), p. 89263P.
25. S. Stübinger, S. Ghanaati, B. Saldamli, C. Kirkpatrick, and R. Sader, "Er:yag laser osteotomy: preliminary clinical and histological results of a new technique for contact-free bone surgery," Eur. Surg. Res. **42**(3), 150–156 (2009).
26. L. M. Beltrán, G. Shayeganrad, G. Kosa, M. Zelechowski, G. Rauter, N. Friederich, P. C. Cattin, and A. Zam, "Performance of er:yag laser ablation of hard bone under different irrigation water cooling conditions," in *Optical Interactions with Tissue and Cells XXIX*, vol. 10492 (International Society for Optics and Photonics, 2018), p. 104920B.
27. M. H. Niemzet al., *Laser-tissue interactions: Fundamentals and applications*, 4th Edition (Springer Nature Switzerland AG, 2019).
28. A. Vogel and V. Venugopalan, "Mechanisms of pulsed laser ablation of biological tissues," Chem. Rev. **103**(2), 577–644 (2003).
29. H. C. W. Skinner, J. Albright, and R. Brand, *The Scientific Basics of Orthopaedics* (Appleton and Lange Press Norwalk Connecticut, 1987).
30. M. Forrer, M. Frenz, V. Romano, H. Altermatt, H. Weber, A. Silenok, M. Istomyn, and V. Konov, "Bone-ablation mechanism using co2 lasers of different pulse duration and wavelength," Appl. Phys. B **56**(2), 104–112 (1993).

Biomedical Optics EXPRESS

31. V. V. Tuchin, "Tissue optics and photonics: Light-tissue interaction ii," J. Biomed. Photonics Eng. **2**(3), 030201 (2016).
32. H. N. Kenhagho, G. Rauter, R. Guzman, P. Cattin, and A. Zam, "Optoacoustic tissue differentiation using a mach-zehnder interferometer: Preliminary results," in *2018 IEEE International Ultrasonics Symposium (IUS)* (IEEE, 2018), pp. 1–9.
33. H. Abbasi, G. Rauter, R. Guzman, P. C. Cattin, and A. Zam, "Differentiation of femur bone from surrounding soft tissue using laser-induced breakdown spectroscopy as a feedback system for smart laserosteotomy," in *Biophotonics: Photonic Solutions for Better Health Care VI*, vol. 10685 (International Society for Optics and Photonics, 2018), pp. 1068519.
34. M. Eugster, P. C. Cattin, A. Zam, and G. Rauter, "A parallel robotic mechanism for the stabilization and guidance of an endoscope tip in laser osteotomy," in *2018 IEEE/RSJ International Conference on Intelligent Robots and Systems (IROS)*, (IEEE, 2018), pp. 1306–1311.
35. M. Eugster, E. Zoller, L. Fasel, P. C. Cattin, N. Friederich, A. Zam, and G. Rauter, "Contact force estimation for minimally invasive robot-assisted laser osteotomy in the human knee," in *CRAS 2018 Proceedings of the 8th Joint Workshop on New Technologies for Computer/Robot Assisted Surgery*, (Queen Mary University of London, 2018).
36. J. M. Khosrofian and B. A. Garetz, "Measurement of a gaussian laser beam diameter through the direct inversion of knife-edge data," Appl. Opt. **22**(21), 3406–3410 (1983).
37. ISO11146-1, *Test methods for laser beam widths, divergence angles and beam propagation ratios. Part 1: Astigmatic and simple astigmatic beams* (ISO, 2005).
38. J. T. Walsh and T. F. Deutsch, "Pulsed co2 laser tissue ablation: measurement of the ablation rate," Lasers Surg. Med. **8**(3), 264–275 (1988).
39. J. T. Walsh, T. J. Flotte, and T. F. Deutsch, "Er:yag laser ablation of tissue: effect of pulse duration and tissue type on thermal damage," Lasers Surg. Med. **9**(4), 314–326 (1989).
40. L. M. Beltrán, I. T. Schmidt, N. Vulin, J. Widmer, J. G. Snedeker, P. C. Cattin, A. Zam, and G. Rauter, "Optimizing controlled laser cutting of hard tissue (bone)," at-Automatisierungstechnik **66**(12), 1072–1082 (2018).
41. O. Svelto and D. C. Hanna, *Principles of lasers*, vol. 1 (Springer, 2010).
42. Z.-Z. Li, L. Reinisch, and W. P. Van de Merwe, "Bone ablation with er: Yag and co2 laser: study of thermal and acoustic effects," Lasers Surg. Med. **12**(1), 79–85 (1992).
43. M. Stanislawki, J. Meister, T. Mitra, M. Ivanenko, K. Zanger, and P. Hering, "Hard tissue ablation with a free running er: Yag and a q-switched co 2 laser: a comparative study," Appl. Phys. B **72**(1), 115–120 (2001).
44. A. Hamidi, Y. A. Bayhaqi, F. Canbaz, A. Navarini, P. C. Cattin, and A. Zam, "Imaging photothermal-induced expansion of bone during laser osteotomy by phase-sensitive oct: preliminary results," in *Biomedical Spectroscopy, Microscopy, and Imaging*, vol. 11359 (International Society for Optics and Photonics, 2020), p. 113590K.
45. M. Augello, C. Baetscher, M. Segesser, H.-F. Zeilhofer, P. Cattin, and P. Juergens, "Performing partial mandibular resection, fibula free flap reconstruction and midfacial osteotomies with a cold ablation and robot-guided er: Yag laser osteotome (carlo®)–a study on applicability and effectiveness in human cadavers," J. Craniomaxillofac. Surg. **46**(10), 1850–1855 (2018).
46. H. H. Müller, L. Ptaszynski, K. Schlott, C. Debbeler, M. Bever, S. Koinzer, R. Birngruber, R. Brinkmann, and G. Hüttmann, "Imaging thermal expansion and retinal tissue changes during photocoagulation by high speed oct," Biomed. Opt. Express **3**(5), 1025–1046 (2012).
47. H. Abbasi, G. Rauter, R. Guzman, P. C. Cattin, and A. Zam, "Laser-induced breakdown spectroscopy as a potential tool for autocarbonization detection in laserosteotomy," J. Biomed. Opt. **23**(07), 1 (2018).
48. J. T. Walsh Jr and T. F. Deutsch, "Er:yag laser ablation of tissue: measurement of ablation rates," Lasers Surg. Med. **9**(4), 327–337 (1989).
49. T. Barton, H.-J. Foth, M. Christ, and K. Hörmann, "Interaction of holmium laser radiation and cortical bone: ablation and thermal damage in a turbid medium," Appl. Opt. **36**(1), 32–43 (1997).
50. A. J. Welch and M. J. Van Gemertet al., *Optical-thermal Response of Laser-irradiated Tissue*, vol. 2 (Springer, 2011).
51. I. I. Chen and S. Saha, "Thermal analysis of the bone surface induced by laser radiation," Ann. Biomed. Eng. **15**(5), 457–466 (1987).
52. J. S. Nelson, L. Yow, L.-H. Liaw, L. Macleay, R. B. Zavar, A. Orenstein, W. H. Wright, J. J. Andrews, and M. W. Berns, "Ablation of bone and methacrylate by a prototype mid-infrared erbium:yag laser," Lasers Surg. Med. **8**(5), 494–500 (1988).

Chapter 6

Coupling laser light and optimization of bone ablation through optical fibers

The publication presented in this chapter shows how different optical fibers performed when the Er:YAG laser was coupled to them. The fibers used were *germanium oxide* (GeO_2), *sapphire* (Al_2O_3), *zirconium fluoride* (ZrF), and *hollow-core silica waveguide* (HSW). The main objective was to find a suitable fiber for use in a robotic endoscopic device for minimally-invasive deep-bone ablation. We evaluated the transmission efficiency stability of the fibers at different input energies, the transmission stability over time at the highest achievable energy of the laser, and the transmission stability over time at different bending radii. Based on the optimization results from Chapter 5, we used the same water jet irrigation and feedback systems during bone ablation through the optical fiber. For this purpose, the best performing fiber (which was the GeO_2), was used for bone ablation, and we designed a refocusing system for placement after the fiber end tip. With the fiber system, we obtained maximum depths of 6.8 mm in a sheep tibia at 370 mJ at a repetition rate of 10 Hz, and 10 mm in pig bone at 450 J, the latter is not presented in this publication due to lack of repetitive experiments. A histology study for bone ablated through the optical fiber is also presented, the images indicate that no damage to the tissue adjacent to the cuts.

Publication: Lina M. Beltrán Bernal, Ferda Canbaz, Salim E. Darwiche, Katja M. R. Nuss, Niklaus F. Friederich, Philippe C. Cattin, and Azhar Zam, "Optical fibers for endoscopic high-power Er:YAG laserosteotomy", J. Biomed. Opt. 26(9) 095002 (13 September 2021).
DOI: https://doi.org/10.1117/1.JBO.26.9.095002

Optical fibers for endoscopic high-power Er:YAG laserosteotomy

Lina M. Beltrán Bernal,[a,*] **Ferda Canbaz**,[a] **Salim E. Darwiche**,[b,c] **Katja M. R. Nuss**,[b,c] **Niklaus F. Friederich**,[d] **Philippe C. Cattin**,[e] **and Azhar Zam**[a,*]

[a]University of Basel, Department of Biomedical Engineering, Faculty of Medicine, Biomedical Laser and Optics Group, Allschwil, Switzerland
[b]University of Zürich, Musculoskeletal Research Unit, Zürich, Switzerland
[c]University of Zürich, Center for Applied Biotechnology and Molecular Medicine, Zürich, Switzerland
[d]University of Basel, Department of Biomedical Engineering, Faculty of Medicine, Center of Biomechanics and Biocalorimetry, Allschwil, Switzerland
[e]University of Basel, Department of Biomedical Engineering, Faculty of Medicine, Center for medical Image Analysis and Navigation, Allschwil, Switzerland

Abstract

Significance: The highest absorption peaks of the main components of bone are in the mid-infrared region, making Er:YAG and CO_2 lasers the most efficient lasers for cutting bone. Yet, studies of deep bone ablation in minimally invasive settings are very limited, as finding suitable materials for coupling high-power laser light with low attenuation beyond 2 μm is not trivial.

Aim: The first aim of this study was to compare the performance of different optical fibers in terms of transmitting Er:YAG laser light with a 2.94-μm wavelength at high pulse energy close to 1 J. The second aim was to achieve deep bone ablation using the best-performing fiber, as determined by our experiments.

Approach: In our study, various optical fibers with low attenuation ($\lambda = 2.94$ μm) were used to couple the Er:YAG laser. The fibers were made of germanium oxide, sapphire, zirconium fluoride, and hollow-core silica, respectively. We compared the fibers in terms of transmission efficiency, resistance to high Er:YAG laser energy, and bending flexibility. The best-performing fiber was used to achieve deep bone ablation in a minimally invasive setting. To do this, we adapted the optimal settings for free-space deep bone ablation with an Er:YAG laser found in a previous study.

Results: Three of the fibers endured energy per pulse as high as 820 mJ at a repetition rate of 10 Hz. The best-performing fiber, made of germanium oxide, provided higher transmission efficiency and greater bending flexibility than the other fibers. With an output energy of 370 mJ per pulse at 10 Hz repetition rate, we reached a cutting depth of 6.82 ± 0.99 mm in sheep bone. Histology image analysis was performed on the bone tissue adjacent to the laser ablation crater; the images did not show any structural damage.

Conclusions: The findings suggest that our prototype could be used in future generations of endoscopic devices for minimally invasive laserosteotomy.

 [DOI: 10.1117/1.JBO.26.9.095002]

Keywords: laser ablation of bone; Er:YAG laser; optical fiber; germanium oxide fiber; sapphire fiber; zirconium fluoride fiber; hollow-core silica waveguide; deep bone ablation; minimally invasive laserosteotomy.

Paper 210145R received May 1, 2021; accepted for publication Aug. 16, 2021; published online Sep. 13, 2021.

*Address all correspondence to Lina M. Beltrán Bernal, lina.beltran@unibas.ch; Azhar Zam, azhar.zam@unibas.ch

1 Introduction

In the field of osteotomy, the use of lasers has been studied for several years;[1–8] however, some early clinical studies showed severe collateral damage and a prolonged healing process.[9] In response, efforts have been made to optimize laser systems intended for laserosteotomy. For example, modern Er:YAG laser systems have been used to remove intraoral hard tissue in humans, without showing damage in subsequent histological analyses.[10] More recent studies have shown how the use of new irrigation and temperature feedback detection systems for Er:YAG laserosteotomy can help achieve safe, deep bone ablation.[11] Other results from a robotic free-space laser device, CARLO®, based on an Er:YAG laser, show potential for use in osteotomy applications. The CARLO laser device was used for the first clinical bone surgery worldwide, where the functionality of the patient's jaw was improved. After years of investigation in the field, the device was used in July 2019 for an *in vivo* mid-face osteotomy at the Department of Oral Maxillofacial Surgery, University Hospital Basel, Switzerland.[7,12,13]

Several aspects make lasers attractive for tissue ablation. It is a safer procedure with respect to preventing bacterial and viral infection during surgery because of the contactless nature of the laser–tissue interaction. Lasers also make it easier to achieve the flexible cuts (various shapes and curves) desired during surgery, especially for cutting hard tissue. Although surgery with conventional mechanical tools has evolved to be as minimally invasive as possible, the flexibility provided by these tools remains limited.[14] Endoscopic devices have emerged for use in minimally invasive procedures. These devices provide solutions for diagnosis and microsurgeries inside the body where other tools cannot reach.[15,16] For endoscopic laser surgery involving hard tissues, some studies have shown the benefits of using fiber-coupled or fiber-based lasers.[17,18] Lasers working from 600 nm up to 2 μm can be easily coupled in low-OH silica fibers due to their low attenuation in this wavelength region. For instance, a Ho:YAG laser at a wavelength of 2.12 μm has been widely used for lithotripsy;[19] it can be used in endoscopic applications by means of silica fibers, as can the thulium laser at a wavelength of 1.908 μm.[20] For endoscopic surgical applications requiring deeper hard-tissue ablation, such as a typical maxillofacial surgery on the jaw or during knee surgery, a laser delivering more energy per pulse through the optical fiber is needed. We return to the Er:YAG laser, which has shown outstanding results for deep bone ablation.[10,11] Throughout the history of fiber research, finding materials for coupling laser light with low attenuation around 3 μm has not been trivial. Today, however, some materials, such as sapphire, fluoride,[18] and germanium oxide fibers,[17] show encouraging results regarding the transmission of infrared (IR) light close to 3 μm. The main purpose of this study was to investigate some of the fibers known to efficiently transmit Er:YAG laser energy at a wavelength of 2.94 μm. For this study, we chose four different fibers to couple an Er:YAG laser. Transmission efficiency, resistance to high-power laser energy, and bending flexibility are the key criteria to consider when selecting a fiber for endoscopic laserosteotomy, especially for deep bone ablation.

2 Materials and Methods

2.1 *Laser Source and Optical Fibers*

The laser source used in this study was a microsecond high-power Er:YAG laser (Syneron Litetouch) with wavelength $\lambda = 2.94$ μm. The energy per pulse of the laser could be set within the range 100 to 820 mJ, with a repetition rate range of 1 to 50 Hz and a pulse duration range of 100 to 400 μs. We studied the performance of four different fibers in terms of (1) the transmission efficiency and its stability over time; (2) the input tip temperature; and (3) the bending stability of the fibers over time. The fibers chosen for our study are known to have high transmission in the mid-IR wavelength range. To compare performance, we used fibers with similar core sizes and a 1-m length. The glass-based fibers were made of germanium oxide (GeO_2), sapphire (Al_2O_3), zirconium fluoride glass (ZrF_4), and a hollow-core silica waveguide, respectively. Table 1 displays the main properties of the fibers used.

"Germanium" fibers consist of a germanium oxide (GeO_2) glass core, a glass cladding, a polyamide coating, and a thermoplastic coating in the external layer. "Sapphire" (Al_2O_3) fibers

Table 1 Properties of the optical fibers used.

	Germanium (GeO_2)	Sapphire (Al_2O_3)	Fluoride (ZrF_4)	Hollow-core silica
Core size (μm)	450	425	400	500
NA	0.25	0.12	0.2	0.025
Attenuation (dB/m)	0.5	0.25	0.015	1.5
Min. bending rad (cm)	4	8	4.5	15
Manufacturer	Infrared Fiber Systems	Laser Components	Le Verre Fluoré	Laser Components

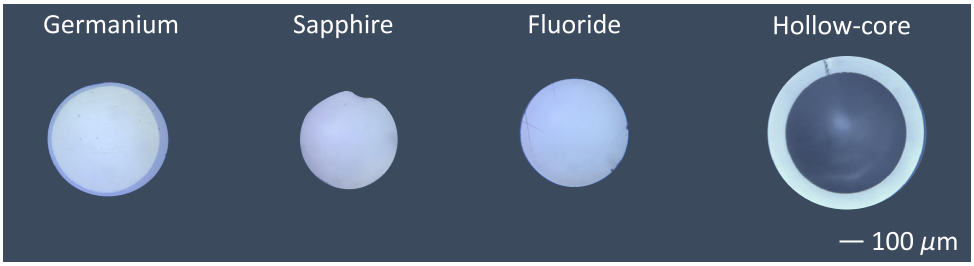

Fig. 1 Microscopic images of the fibers' polished surfaces.

have neither cladding nor sheathing. "Fluoride" fibers are made of a zirconium fluoride (ZrF_4) glass core and have a double cladding. The second cladding is made of low index resin. It has an external polyacrylate sheathing and germanate end caps. End-capping is a technology in which a different material is spliced into the fiber tip to reduce the power density at the end tips, thereby decreasing the heat as well. The inner wall of "hollow-core" fiber is made of a silver iodide (AgI) reflector, covered by a silica tube and an external acrylate buffer. All of the fibers are commercially available, except for the fluoride one. Currently, fluoride fibers are in a testing phase. Figure 1 shows the end tips of the fibers when they are polished. The end tips were observed with a fiber inspection scope (Thorlabs, FS200) and images were taken using a mobile phone camera.

2.2 *Coupling the Laser into the Fibers*

Figure 2 shows a diagram of the setup used for our study. The setup diagram is divided into four parts, representing the sequence of steps performed during our experiments. The coupling process corresponds to steps (1a) and (1b). Two coupling mirrors M_1 and M_2 (1a) were used to optimize the coupling process. In (1b), a calcium fluoride (CaF_2) focusing lens with 25.4-mm focal length was mounted to an XY translating lens mount. The optical fiber was inserted in a fiber chuck for bare fibers (Newport, FPH-DJ), placed on a Z translating mount and an $XYZ\theta_x\theta_y$ fiber optic positioner (Newport, FP-2A). With a laser M^2 of 22, the lens provided a beam size of 292 μm at the focal plane. The divergence of the beam was $\theta = 0.14$ rad, which fulfilled the requirements of the germanium and the fluoride fibers; it was a little high for the sapphire fiber whose numerical aperture (NA) was 0.12, and too high for the hollow-core fiber (NA = 0.025). In previous experiment,[21] a beam size of 328 μm and a suitable beam divergence of 0.12 rad for the sapphire fiber was used; however, the fiber could not withstand more than 300 mJ. According to the following equation for calculating the beam size D_0,

$$D_0 = \frac{2\lambda M^2}{\pi\theta}, \tag{1}$$

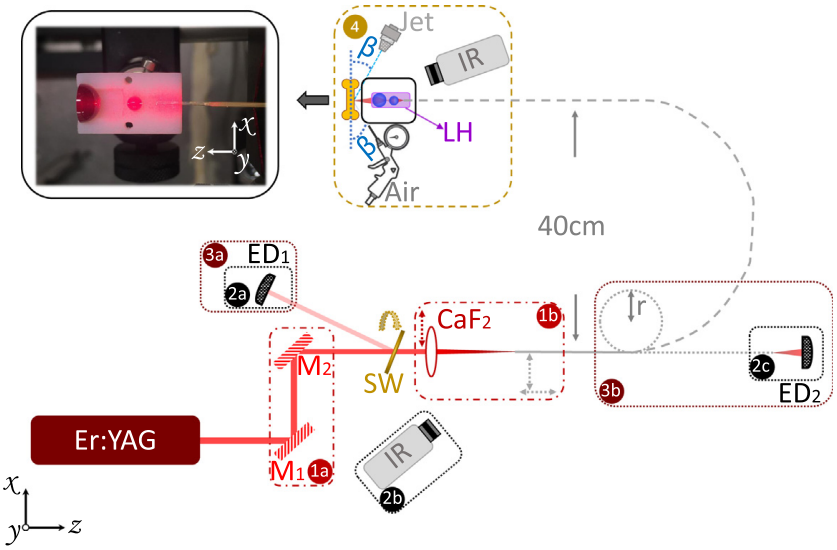

Fig. 2 Schematic of the setup used for studying the performance of several glass fibers for transmitting Er:YAG laser light. The laser was coupled to an optical fiber by means of two coupling mirrors (1a) and a coupling CaF_2 lens (1b). A portion of the initial energy was measured with an energy meter ED_1 (2a). The transmitted energy was measured with an energy meter ED_2 (2c). While the reflected and the transmitted energy were being measured, an IR camera recorded the temperature of the fiber input face (2b). The bending stability of the fibers was tested by bending the fibers to different radii r (3b), the transmission efficiency was also determined by the reflected energy measured with ED_1 (3a), and the transmitted energy measured with ED_2 (3b). The ablation performance of the laser through one of the fibers was studied (4). An IR camera was used as a temperature feedback system to automatically control a water jet irrigation system. The water jet (diameter 50 μm) was placed at an angle ($\beta = 30$ deg) in the upper right quadrant of the XZ-plane. A pressurized air gun was placed at an angle ($\beta = 30$ deg) in the lower right quadrant of the XZ-plane. The photograph next to (4) presents the final lenses and holder design used for ablation.

to satisfy $\theta \leq \mathrm{NA}$ for the hollow-core fiber with the current laser, the beam size at the tip of the fiber had to be $\geq$1.6 mm, exceeding the size of its 500-μm hollow core. These facts regarding the sapphire and the hollow-core fibers were taken into account in the subsequent experiments.

2.3 *Transmission Efficiency over Energy*

In this section, we describe the transmission efficiency over energy for each fiber for 100 pulses at 5 and 10 Hz. To determine the ratio of transmitted energy over input energy, we used two energy meters ED_1 and ED_2, depicted in Fig. 2. To determine the input energy, we used a sapphire window (SW) to reflect a small percentage of the beam into the first energy detector ED_1, step (2a). The reflected percentage from the SW was about 0.5%. The transmitted energy was measured directly with the second energy detector ED_2, step (2c).

2.4 *Transmission Stability over Time and Temperature Monitoring*

At the maximum level of energy transmitted by each fiber at 5 and 10 Hz, we studied the stability of the transmission over 5 min. While measuring the reflected and transmitted energies [Fig. 2, steps (2a) and (2c), respectively], we monitored the temperature at the fiber input tip, using an IR camera, FLIR A655sc at 50 fps, step (2b).

2.5 *Bending Stability*

Fiber flexibility and transmission efficiency were studied by bending the fiber to different radii r, as depicted in Fig. 2, until reaching the minimum bending radius reported by the manufacturer

for each fiber (Table 1). The two detectors, ED_1 in step (3a) and ED_2 in step (3b), were used to determine the transmission efficiency of the bent fiber over time. The measurement was performed for 5 min at each bending radius.

2.6 *Miniaturized Focusing System for Appropriate Ablation through Fiber*

The ablation of bone in free space, using our Er:YAG laser, had already been optimized for a beam size of 526 μm.[11] We designed a lens system capable of focusing the beam in a manner similar to that of the previous study's free-space setup.[11] Since beam propagation differs depending on the type of fiber it passes through (due to different output NA), the lens was designed for the fiber that we considered most suitable for endoscopic laser surgeries, based on the experimental findings. Figure 2, step (4) shows a picture of the lens design used for the ablation experiments. The design is described in more detail in Sec. 3.4.

2.7 *Bone Ablation Performance in Minimally Invasive Settings*

Figure 2, step (4) depicts the bone ablation process. The samples used were sheep tibia cortical bone from the Musculoskeletal Research Unit at the University of Zürich. The cadaveric sheep bones were obtained from an animal euthanized in the context of an experiment unrelated to the study reported herein. The cadaveric samples were used within 84 h after the animal was euthanized, and kept moist at all times before ablation. Three ablation lines, 10-mm long, were each created over a 4-min period. The irrigation system was composed of a Maximator pump ref No. MP030066 and a nozzle from Synova Laser MicroJet Technology. The nozzle produced a water jet with a diameter of 50 μm. For the experiments, the pump ran at 30 bar pressure. Pressurized air of 2 bar was used to blow off the debris and the remaining water from the ablated area. The IR camera described in Sec. 2.4 was used to monitor the superficial temperature of the bone. Immediately after ablation, the samples were preserved in 4% formalin. One week later, the samples were taken out for a short time to measure the depth and width of the ablated areas. This measurement was performed using an optical coherence tomography (OCT) system available in our laboratory. The OCT system was composed of an Axsun swept laser with a 1064-nm central wavelength and a 100-nm bandwidth. B-scans to analyze the images were taken with a 14.5-mm field of view and 3.51-mm imaging depth.

The ablation setup used in our study, comprising an automated temperature feedback mechanism (IR camera) for the irrigation system (thin water jet) and pressurized air, was described in detail in our previous study.[11]

2.8 *Histology*

Sheep cortical bone samples were used to create cuts using the Er:YAG laser through an optical fiber. The non-decalcified bone samples were fixed in 4% buffered formalin, then dehydrated in an ascending series of ethanol, after which, the samples were defatted in xylene and immersed in methylmethacrylate under vacuum; final polymerization was reached after complete infiltration. Thick sections (200 to 700 μm) were cut using a diamond saw (Exact® 310 saw), mounted on Acropal slides and surface stained with toluidine blue. The sections were then imaged using a macroscope (Z6 APO A, Leica Microsystems) with a DFC450 Digital Camera (Leica Microsystems). For higher magnifications, we used a DMR microscope system (Leica Microsystems) with a DC320 digital camera (Leica Microsystems).

3 Results and Discussion

3.1 *Transmission Efficiency over Energy*

Figure 3 shows the transmission efficiency over the input energy of the laser, obtained for each fiber at 5 and 10 Hz. Each data point on the graph is the average over 100 pulses with the corresponding standard deviation.

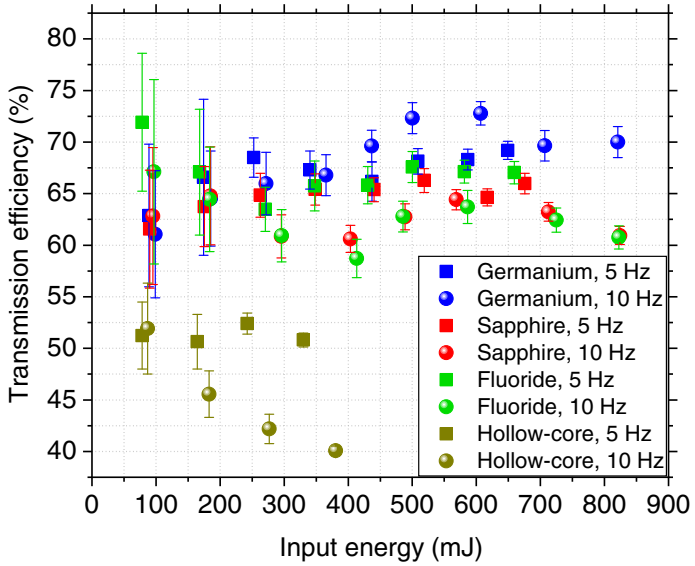

Fig. 3 Transmission efficiency of germanium oxide, sapphire, zirconium fluoride, and hollow-core silica fibers at 5 and 10 Hz at different input energies.

During our experiments, the transmission efficiency obtained for the sapphire fiber was 64% ± 2%; however, other researchers have shown that the sapphire fiber can reach up to 90% transmission efficiency.[18] The relatively low performance in our study was most likely caused by a beam divergence that did not completely fulfill the NA requirements of the sapphire fiber. As seen in Fig. 3, the fluoride fiber achieves higher transmission at low energies and then tapers off; its transmission efficiency was 65% ± 3%. The hollow-core fiber tip burned at energies higher than 400 mJ, resulting in the need to unmount and polish the fiber. The maximum input energy for the hollow-core fiber (without burning) was 330 and 380 mJ at 5 and 10 Hz, respectively. The lowest transmission was observed in the hollow-core fiber; at 5 Hz, the transmission efficiency was only 51% ± 1%, while at 10 Hz, the transmission was 45% ± 5%, decreasing over the energy. NA matching issues account in part for the low performance of the hollow-core fiber. Of the fibers used, the germanium fiber showed the highest transmission efficiency at 68% ± 3%, similar to that achieved in other studies.[22]

3.2 *Transmission Stability over Time and Monitoring the Input Tip Temperature*

After examining the behavior of the fibers exposed to different input energies, the transmission stability of the fibers was tested for 300 s (5 min). We applied the laser's maximum achievable energy level, about 820 mJ, to the input fiber face. Since the hollow-core fiber could not withstand such high energy levels, we used energy settings of 330 and 380 mJ at 5 and 10 Hz, respectively, for this fiber.

Figure 4 shows the evolution of the transmission efficiency of each fiber over 5 min at 5 and 10 Hz. The values (black data points) presented in each graph are an average of five individual measurements, the gray areas represent the corresponding standard deviation.

In general, all of the fibers showed stable energy transmission over time. The fluoride fiber showed a decrease in energy transmission in the first 100 s, but stabilized thereafter.

The input face temperature of each fiber was monitored while simultaneously measuring its energy transmission. Figure 5 shows the average temperature of each fiber tip.

At 10 Hz, the temperature of the germanium fiber dropped within the first 100 s; this is in part because the energy of the laser drops a little over time. The drop in temperature probably also reflects a decrease in the fiber material's heat capacity around the average temperature of 70°C, measured with our thermal camera. At lower temperatures, there was no noticeable change in the material's heat capacity, as observed for both the germanium oxide fiber at 5 Hz and for the other fibers. The sapphire fiber tip's temperature increased the least among all of the fibers. Additionally, sapphire's physical properties make it highly resistant to scratches and fractures.[23]

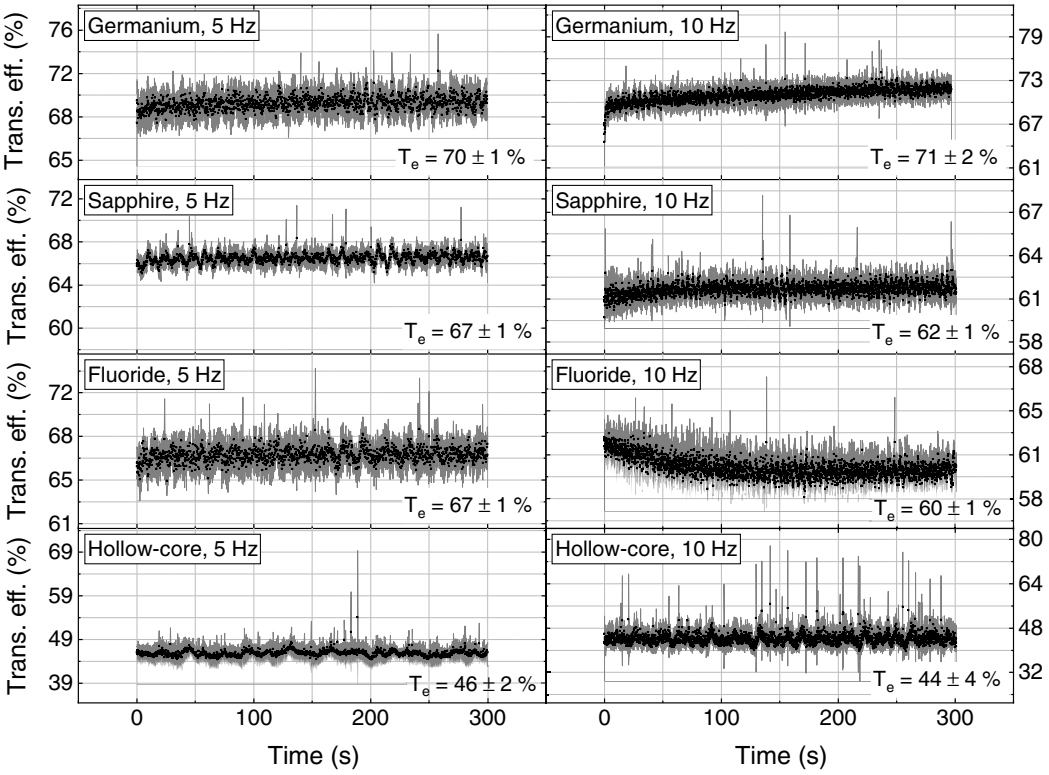

Fig. 4 Transmission efficiency over time of each fiber at 5 and 10 Hz. The input energy was 820 mJ for all fibers except the hollow-core fiber, which was set at 330 and 380 mJ at 5 and 10 Hz, respectively.

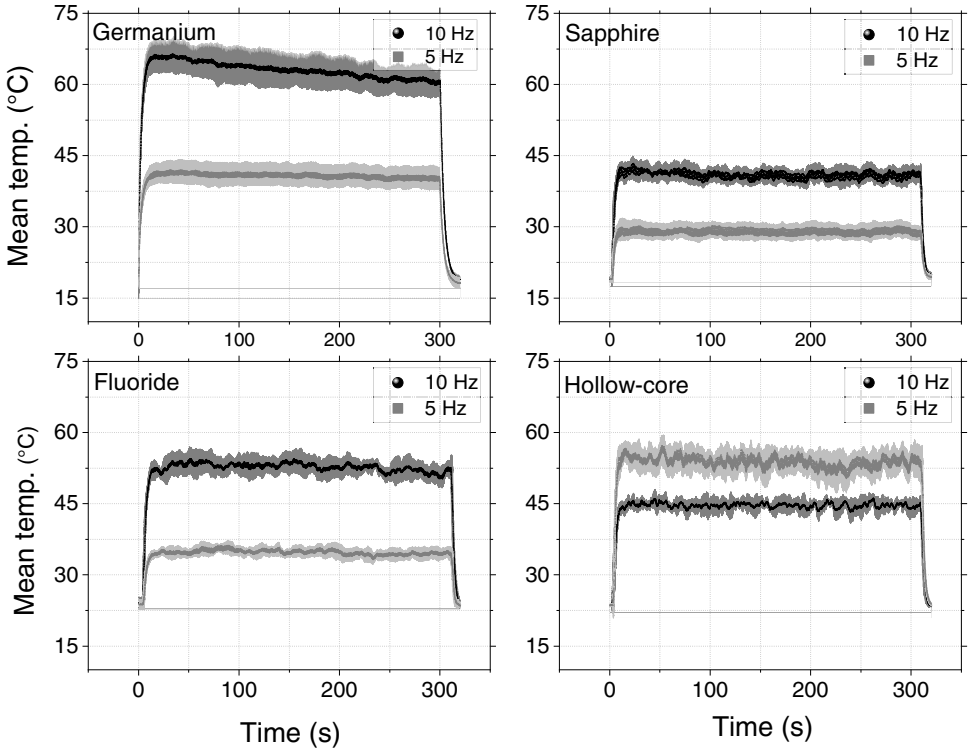

Fig. 5 Evolution of the temperature of each input fiber tip, monitored for 300 s. The input energy of the laser was 820 mJ for all fibers except the hollow-core fiber, which was set at 330 and 380 mJ at repetition rates 5 and 10 Hz, respectively.

Therefore, for endoscopic applications, one may consider using sapphire fibers or splicing them in other fibers.[24] Doing so may reduce the heat at the endoscope's tip, thereby also reducing the risk of damaging sensitive material and making it easier to manipulate the fiber.

3.3 *Bending Stability*

After the fibers were tested for transmission efficiency, behavior over time, and input tip temperature over time, we bent the fibers from a straight position up to the minimum bending radii reported by the manufacturers.

Figure 6 shows the effect of bending the fibers on transmission efficiency. As in Sec. 3.2, we delivered the maximum possible energy to the fibers. Each individual data point in the graph is the average over 5 min of five individual measurements.

As seen in Fig. 6, the transmission efficiency of the fibers does not change remarkably when bent to the minimum radius possible, except in the case of the sapphire fiber. At its minimum bending radius, the transmission of the sapphire fiber dropped from 60% to 53% at 10 Hz and from 67% to 60% at 5 Hz. The transmitted energy dropped in an unusual way for the bent fluoride fiber: the fiber tip was burnt and had to be polished. The transmission efficiency of the fluoride fiber at a 4.5-cm bending radius, as reported in Fig. 6, corresponds to the response of the fiber after repair.

3.4 *Bone Ablation Performance in Minimally Invasive Settings*

Based on the properties of the fibers (Table 1) and the studies realized in the previous sections, we found that the germanium oxide fiber fulfilled most of the requirements for use in endoscopic surgical applications. The germanium fiber is biocompatible, showed slightly higher transmission efficiency than the other fibers (Figs. 3 and 4), and is the most flexible among the fibers tested; its minimum bending radius is 4 cm. The only disadvantage of the germanium oxide fiber relative to the others is the high tip temperature reached while the laser was being coupled. However, this issue can be solved by choosing coupling and refocusing materials (for lenses and holders) that dissipate the heat efficiently, or by adding a cooling system to the fiber. The fiber tips can be treated, for instance. Previous studies have shown that the germanium fiber can be spliced with sapphire, although doing so reduced its transmission from 68% to 65%.[22]

In this section, we present a refocusing system designed for the germanium fiber. The refocusing system consisted of two lenses inserted into a holder. This system was used for ablating

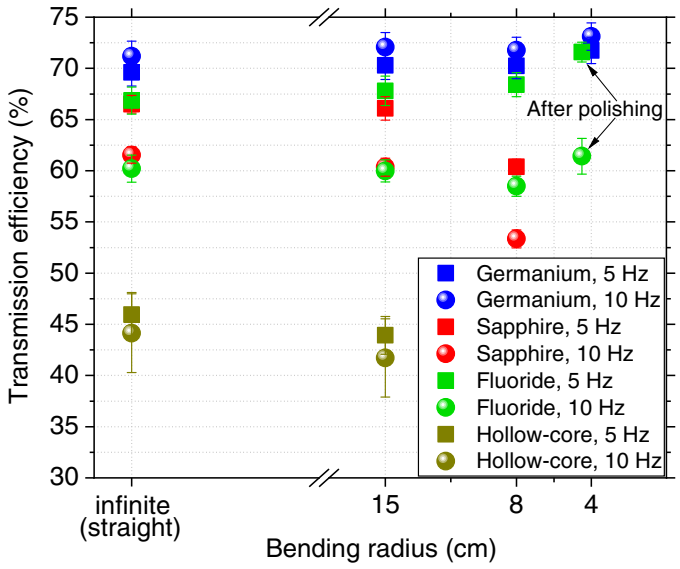

Fig. 6 Transmission efficiency of each fiber at different bending radii. The transmission efficiency of the fluoride fiber at 4.5 cm radius corresponds to the response of the fiber after polishing its surface. The input energy of the laser was 330 mJ (at 5 Hz) and 380 mJ (at 10 Hz) for the hollow-core fiber, and 820 mJ for the others. The repetition rate of the laser was 5 and 10 Hz.

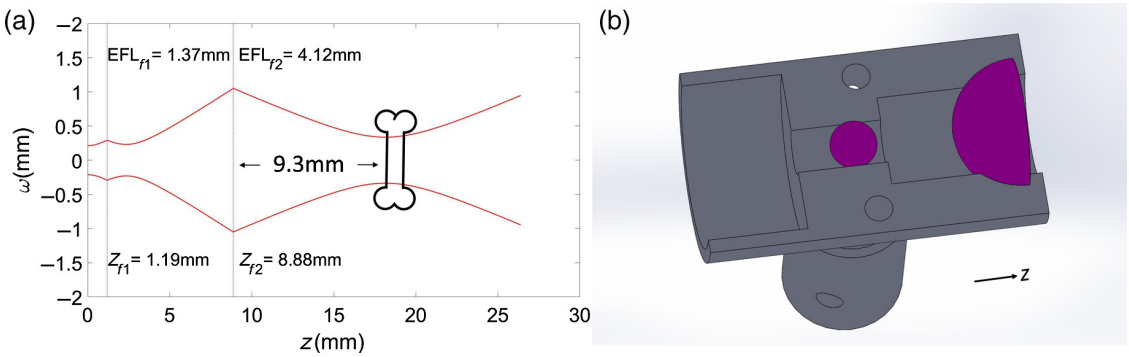

Fig. 7 (a) Schematic of the propagation of the beam after the fiber and the two focusing lenses (represented by the two vertical dashed lines) have been inserted, calculated using MATLAB. (b) Lenses and holder design made in SolidWorks.

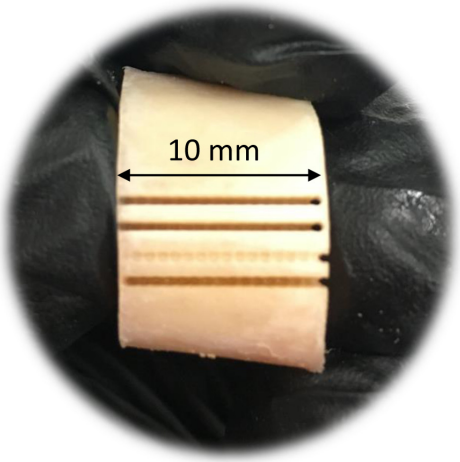

Fig. 8 Photograph of one of the sheep bones ablated with the Er:YAG laser through a germanium oxide fiber. All of the lines have a length of 10 mm. The first two lines and the fourth one were made by scanning the bone 180 times (about 4 min at a speed of 8 mm/s). The third line was ablated with only one laser scan.

sheep bones. Figure 7 shows a schematic of beam propagation after the fiber and the two focusing lenses have been inserted, such that the beam focuses on the bone surface at almost 10 mm beyond the last lens. The lenses were ruby-doped sapphire ball and half-ball lenses from Edmund Optics. The corresponding effective focal lengths were $\mathrm{EFL}_{f1} = 1.37$ mm and $\mathrm{EFL}_{f2} = 4.12$ mm. The first lens was a ball lens with a diameter of 2.38 mm, while the second lens was a half-ball lens with a diameter of 6.35 mm. This lens system provides a beam diameter of 673 μm at the focal plane, located 9.3 mm away from the last lens.

The lens holder was 3D-printed in VeroWhitePlus, RGD835 material. This material is not biocompatible and, therefore, not recommended for real surgery applications. However, it was a very useful prototype and served to identify the benefits of our system, as well as the issues to be improved.

Figure 8 shows a photograph of a sheep bone ablated with the Er:YAG laser coupled with the germanium oxide fiber. For ablation, the maximum achievable energy of the laser beyond the lenses was 370 mJ at a 10-Hz repetition rate. The ablation depth achieved through the germanium oxide fiber was 6.82 ± 0.99 mm, while the width was 0.69 ± 0.06 mm.

3.5 *Histology Analysis*

As shown in Fig. 9, the laser was able to cut through sheep cortical bone in a straight path through the bone lamellae. The structural features of the cortical bone adjacent to the laser path remained intact, as seen in Fig. 9(c).

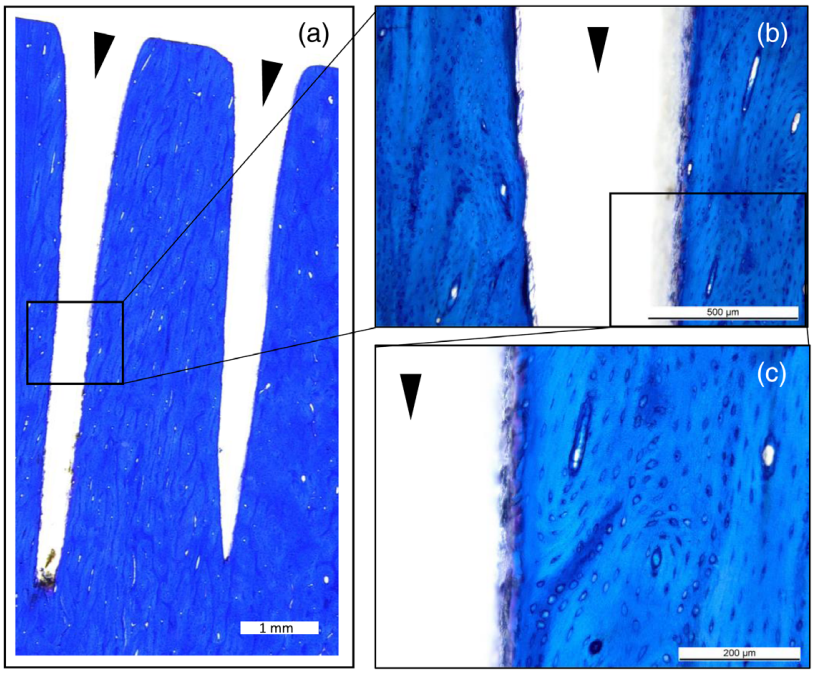

Fig. 9 Sheep cortical bone with two cuts made with the Er:YAG laser through GeO_2 fiber, shown in panel (a). Higher magnifications in panel (b) and panel (c) show the bone tissue interface with the laser's path, as well as the tissue structure. The toluidine blue stain highlights the cells within the bone and the lamellar structure, and shows how the laser can cut through these structures in a controlled manner. The black arrows indicate the laser cuts. The scale bars indicate 1 mm, 500 μm, and 200 μm in panels (a), (b), and (c), respectively.

4 Conclusion

Four fibers suitable for transmitting high-power laser energy in the mid-IR region of the spectrum were used for coupling an Er:YAG laser at a wavelength of 2.94 μm. The setup was not optimal for the sapphire and hollow-core fibers, since the divergence of the beam did not fully match the required NA. However, the sapphire fiber remained undamaged at the laser's maximum energy of 820 mJ. The hollow-core fiber could only withstand a maximum energy of 380 mJ, and the germanium fiber had the highest transmission efficiency at $68\% \pm 3\%$, as shown in Fig. 3. Transmission efficiency was stable for 5 min at 820 mJ for all but the hollow-core fiber, which was stable at 380 mJ. However, the fluoride fiber showed a drop in efficiency after the first 100 s (Fig. 4). Figure 5 shows the input tip temperature over time. In general, it was stable for all fibers, however, the maximum average temperature of the germanium fiber's tip showed higher temperature around 70°C compared to the other fibers. When decreasing the bending radius of the fluoride fiber to 4.5 cm, we observed a drop in the transmitted energy (Fig. 6) and an increase in the temperature of the tip. Examination of the fiber surface through a fiber microscope confirmed the suspicion that the fiber had been damaged. Based on the reported results, and on the results from our previous studies,[21] we consider the germanium oxide fiber to be the most appropriate choice for future endoscopic applications. Still, the temperature issue must be resolved, for instance, by splicing the end tips with sapphire. We designed a lens system capable of focusing the laser beam after the fiber, at nearly 10 mm beyond the last lens, with a beam diameter of 673 μm. At the maximum achievable output energy of 370 mJ at 10 Hz, we obtained an ablation depth of 6.82 ± 0.99 mm in sheep bone. At present, the small working space of the fiber setup limits our ability to align the water jet and pressurized air with the laser beam. Therefore, the irrigation and cleaning design must be adapted to small working distances of less than 10 mm. Histology image analysis showed no structural damage on the surroundings of the cut made with the Er:YAG laser through the GeO_2 fiber (Fig. 9). The fiber system presented in this study has the potential to be implemented in endoscopic laserosteotomy systems.

Disclosures

The authors have no conflicts of interest to declare in this paper.

Acknowledgments

The authors gratefully acknowledge funding from the Werner Siemens Foundation through the Minimally Invasive Robot Assisted Computer-guided LaserosteotomE (MIRACLE) project. The authors gratefully acknowledge Mr. Alex Tchap from Infrared Fiber Systems for providing us the GeO_2 fibers to perform our experiments and Mr. Samuel Poulain, Dr. Solenn Cozic, and Ms. Laurine Bodin from Le Verre Fluoré for providing us the double clad fluoride fiber.

Code, Data, and Materials Availability

The data generated and analyzed in this study are included in this paper.

References

1. S. R. Visuri, J. T. Walsh, and H. A. Wigdor, "Erbium laser ablation of dental hard tissue: effect of water cooling," *Lasers Surg. Med.* **18**(3), 294–300 (1996).
2. K. Stock, R. Hibst, and U. Keller, "Comparison of Er:YAG and Er:YSGG laser ablation of dental hard tissues," *Proc. SPIE* **3192**, 88–96 (1997).
3. M. Werner et al., "Co_2 laser free-form processing of hard tissue," in *Eur. Conf. Biomed. Opt.*, Paper 6632_1, Optical Society of America (2007).
4. L. Kuščer and J. Diaci, "Measurements of erbium laser-ablation efficiency in hard dental tissues under different water cooling conditions," *J. Biomed. Opt.* **18**(10), 108002 (2013).
5. K. Stock, H. Wurm, and F. Hausladen, "Primary investigations on the potential of a novel diode pumped Er:YAG laser system for middle ear surgery," *Proc. SPIE* **9689**, 96892K (2016).
6. N. Jowett et al., "Bone ablation without thermal or acoustic mechanical injury via a novel picosecond infrared laser (PIRL)," *Otolaryngology* **150**(3), 385–393 (2014).
7. K.-W. Baek et al., "A comparative investigation of bone surface after cutting with mechanical tools and Er:YAG laser," *Lasers Surg. Med.* **47**(5), 426–432 (2015).
8. M. Papadaki et al., "Vertical ramus osteotomy with Er:YAG laser: a feasibility study," *Int. J. Oral Maxillofacial Surg.* **36**(12), 1193–1197 (2007).
9. B. Fink et al., "Holmium:YAG laser-induced aseptic bone necroses of the femoral condyle," *Arthroscopy* **12**(2), 217–223 (1996).
10. S. Stübinger et al., "Er:YAG laser osteotomy: preliminary clinical and histological results of a new technique for contact-free bone surgery," *Eur. Surg. Res.* **42**(3), 150–156 (2009).
11. L. M. B. Bernal et al., "Optimizing deep bone ablation by means of a microsecond Er:YAG laser and a novel water microjet irrigation system," *Biomed. Opt. Express* **11**(12), 7253–7272 (2020).
12. K.-W. Baek et al., "Clinical applicability of robot-guided contact-free laser osteotomy in cranio-maxillo-facial surgery: *in-vitro* simulation and *in-vivo* surgery in minipig mandibles," *Br. J. Oral Maxillofacial Surg.* **53**(10), 976–981 (2015).
13. W. Deibel et al., "A compact, efficient, and lightweight laser head for Carlo®: integration, performance, and benefits," *Proc. SPIE* **9579**, 957905 (2015).
14. T. Borus and T. Thornhill, "Unicompartmental knee arthroplasty," *J. Am. Acad. Orthopaedic Surg.* **16**(1), 9–18 (2008).
15. G. Berci and K. A. Forde, "History of endoscopy," *Surg. Endosc.* **14**(1), 5 (2000).
16. G. Iddan et al., "Wireless capsule endoscopy," *Nature* **405**(6785), 417 (2000).
17. N. J. Scott et al., "Mid-IR germanium oxide fibers for contact erbium laser tissue ablation in endoscopic surgery," *IEEE J. Sel. Top. Quantum Electron.* **13**(6), 1709–1714 (2007).
18. J. Qiu et al., "Comparison of fluoride and sapphire optical fibers for Er:YAG laser lithotripsy," *J. Biophotonics* **3**(5–6), 277–283 (2010).

19. M. Sofer et al., "Holmium:YAG laser lithotripsy for upper urinary tract calculi in 598 patients," *J. Urol.* **167**(1), 31–34 (2002).
20. R. L. Blackmon, P. B. Irby, and N. M. Fried, "Holmium:YAG ($\lambda = 2,120$ nm) versus thulium fiber ($\lambda = 1,908$ nm) laser lithotripsy," *Lasers Surg. Med.* **42**(3), 232–236 (2010).
21. L. M. B. Bernal et al., "Measurements of coupling efficiency of high power Er:YAG laser in different types of optical fibers," *Proc. SPIE* **11233**, 112331H (2020).
22. T. J. Polletto et al., "Comparison of germanium oxide fibers with silica and sapphire fiber tips for transmission of erbium:YAG laser radiation," *Lasers Surg. Med.* **38**(8), 787–791 (2006).
23. E. R. Dobrovinskaya, L. A. Lytvynov, and V. Pishchik, *Sapphire: Material, Manufacturing, Applications*, Springer Science & Business Media, Germany (2009).
24. Y. O. Aydin et al., "Endcapping of high-power 3 μm fiber lasers," *Opt. Express* **27**(15), 20659–20669 (2019).

Lina M. Beltrán Bernal received her BSc degree in physics from the Universidad Nacional de Colombia (UNAL), Bogotá D.C., Colombia, in 2013 and her MSc (Hons) degree in advanced optical technologies from the Friedrich-Alexander-Universität Erlangen-Nürnberg (FAU), Erlangen, Germany, in 2016, and her PhD in biomedical engineering from the Universität Basel, Basel, Switzerland, in 2021. Her main research interests include laser technology, design of optical systems for the development smart devices, and smart laser surgery.

Ferda Canbaz is a postdoctoral researcher in the Department of Biomedical Engineering at University of Basel. She received her BS degree in engineering physics from Istanbul Technical University, Istanbul, Turkey, in 2011. She received her MS degree in optoelectronics and photonics engineering in 2013 and her PhD in physics in 2018 from Koç University, Istanbul, Turkey. Her research interests include mid-infrared solid-state/fiber lasers, ultrafast optics, photoacoustic diagnosis, and smart laser surgery.

Salim E. Darwiche received his bachelor's and master's degree in bioengineering from the University of Pennsylvania in 2006 and 2008, respectively. He then completed his PhD in biotechnology and bioengineering from the École polytechnique Fédérale de Lausanne in 2013. Since 2014, he has worked as a study director and senior scientist at the MSRU. He is also the scientific coordinator of the Center for Applied Biotechnology and Molecular Medicine (CABMM) and as such, acts as a liaison to facilitate collaborations within the consortium of CABMM experts. He has significant experience in designing, implementing, and managing *in-vivo* studies in compliance with GLP. He has directed and managed many multiyear projects with industrial and academic project partners. He is FELASA certified for directing animal experimentation and has extensive expertise in musculoskeletal tissue (bone, cartilage, and tendon) and skin repair and regeneration.

Katja M. R. Nuss received her degree in veterinary medicine from the University of Münich, Germany, in 1984, she finished her postgraduate studies from the University of Münich in anesthesiology in 1987, intensive care in 1988, and surgery in 1993. She pursued specializations in surgery (1990) and anesthesiology (2000). She became senior staff at the University of Zürich, Vetsuisse Faculty, Musculoskeletal Research Unit (MSRU) from 2004 to 2019 and became a member of the Leadership Consortium of the MSRU since 2020. She has authored over 71 publications in national and international journals.

Niklaus F. Friederich received his MD from the University of Berne, Switzerland in 1981, and finished post-graduate studies in general surgery, anesthesiology, bone radiology and orthopaedic surgery in Switzerland and USA. He is a board certified orthopaedic surgeon (1991) and adjunct professor of orthopaedic surgery of the University of Basel (2003). He was elected Head of the Dept of Orthopaedic Surgery Bruderholz (1998 to 2013), was a co-founder of Orthoklinik Dornach (2013 to 2015) and joined the Department of Orthopaedics & Traumatology University of Basel (2015-ongoing). He became a medical advisor to the MIRACLE project at the Department of Biomedical Engineering, University of Basel in 2015. In 2019, he was elected visiting professor at the Sunnybrook Health Sciences Center

in Toronto, Ontario, Canada. Citations: 4819 (since 2016: 1952); h-index 37 (since 2016: 24); i10-index 90 (since 2016: 51).

Philippe C. Cattin received his BSc degree from the University of Applied Science in Brugg/Windisch, Windisch, Switzerland, in 1991, his MSc degree in computer science, and his PhD in robotics from ETH Zürich, Zürich, Switzerland, in 1995 and 2003, respectively. From 2003 to 2007, he was a postdoctoral fellow with the Computer Vision Laboratory, ETH Zurich. In 2007, he became an assistant professor with the University of Basel, Allschwil, Switzerland, and was promoted to an associate professor in 2015 and to full professor in 2019. He is the founder of the Center for Medical Image Analysis and Navigation (CIAN), Medical Faculty, University of Basel, where he is the founding head and still heading the Department of Biomedical Engineering. He joined Brigham and Women's Hospital, Boston, MA, USA, in 2017, as a research fellow. He is also the founder of multiple spin-off companies and licensed his patents and software to medical device companies. His research interests include medical image analysis, image-guided therapy, robotics-guided laser osteotomy, and virtual reality. As a principal investigator, he has finished many projects in these areas and published over 250 papers, patents, and book chapters.

Azhar Zam received his BSc degree in medical physics from the University of Indonesia, Depok, Indonesia, in 2004, his MSc degree in biomedical engineering from the University of Lübeck, Lübeck, Germany, in 2007, and his PhD in advanced optical technologies from the Friedrich-Alexander University Erlangen–Nuremberg, Germany, with the focus on optical feedback for tissue-specific laser surgery, in 2011. He held various research positions at the University of Waterloo, Canada; the National University of Ireland Galway, Ireland; the University of California at Davis, USA; and Ryerson University, Toronto, Canada. He joined the Department of Biomedical Engineering, University of Basel, Switzerland, in 2016, as an assistant professor, where he founded and leads the Biomedical Laser and Optics Group (BLOG). He has authored over 80 peer-reviewed articles, book chapters, books, and patents. His main research interests focus on the development of smart devices for medical therapy, diagnostics and monitoring using novel optical technologies, including smart laser surgery, optical coherence tomography (OCT), photoacoustics, biomedical spectroscopy, AI-aided optical diagnostics, and imaging, optical-based smart wearable sensors, and miniaturized systems.

Chapter 7

Discussion and conclusion

7.1 Discussion

The main objective of this thesis was to provide a laser system capable of effectively ablating bone as deep as possible. Since the focus was on minimally invasive laser surgery using robotic endoscopic devices, the laser system also had to be flexible and miniaturized. These requirements were fulfilled by using an optical fiber and a miniaturized refocusing system placed at the end face of the fiber.

First, a microsecond Litetouch Syneron Er:YAG laser, working at a wavelength of 2.94 μm, was characterized and used for free-space bone ablation. The Er:YAG laser is already well known for its ability to ablate hard tissue; it is commercially available as a dental laser. However, in dentistry, where it is used for superficial cuts, there is no need to optimize its efficiency. Since the highest absorption peak of water is near 3 μm, working in a wet environment or using water to cool the tissue can affect ablation efficiency for deep cuts if not optimized.

In the first paper from Chapter 4, we explored the use of a 500 µm diameter water jet for irrigating bone during ablation with the Er:YAG laser. An optimized sequence for the jet was established so that the tissue would not carbonize. In the second paper, a speed for line ablation of 8 mm/s was found to yield higher bone ablation efficiency; more area was removed in less time, compared to other speeds in the range of 0.5 to 8 mm/s. At higher speeds, the separation between two pulses was not sufficient to provide homogeneous ablation along the cut line.

In Chapter 5, we used the Er:YAG laser with a novel 50 μm diameter water jet for irrigation, running at a pressure of of 30 bar, to reach deeper regions while cutting bone. The ablation process was optimized by adding a temperature-monitoring feedback system to avoid carbonization of the bone. A maximum superficial threshold temperature

(which may vary in different configurations, depending on the IR camera properties) of 104 °C was established; lower temperatures were considered safe for the tissue. The irrigation system was activated every time the temperature of the bone reached levels above 104 °C. With this system, a maximum ablation depth of 21 mm (for line ablation) could be achieved without any visible signs of carbonization. A theoretical maximum ablation depth of 30 mm was estimated, but could not be reached in practice because the feedback system was based on surface temperature detection, which is not accurate enough for depths greater than 10 mm. Moreover, the accumulated water and debris were not completely removed by the pressurized air. The results also show how the quality factor of the laser beam (M^2) affects the ablation process; M^2 has a direct impact on the divergence and, thus, on the beam's depth of focus. For constant beam size, as M^2 becomes larger, the divergence is greater and beam intensity rapidly decreases along the direction of propagation, stopping ablation once it reaches the ablation threshold energy density. For the current laser with $M^2 = 22$, the laser cannot ablate deeper than 21 mm. For hole ablation, theoretically, decreasing M^2 by half (from 22 to 10) would permit a cutting depth of 50 mm, achievable in 300 s of ablation; the current laser quality, however, would limit the depth to 18 mm in 300 s.

In Chapter 6, four different optical fibers with low attenuation at 2.94 μm, and suitable for coupling high-power lasers were studied. The aim of the study was to find the best fibers for use in minimally invasive laserosteotomy, and to evaluate ablation of bone through an optical fiber with the help of a miniaturized lens system. In this study, the *germanium oxide*, *sapphire*, and *zirconium fluoride* fibers were capable of withstanding the maximum laser energy output (about 820 mJ at 10 Hz) for at least 5 minutes, both straight and bent. However, the sapphire fiber reduced transmission efficiency from 60 to 53 % at its manufacturer's stated minimum bend radius of 8 cm. The fluoride fiber tip burned at its minimum bend radius of 4.5 cm. The fiber was repaired and, finally, the transmission efficiency reached 72 % at a 4.5 cm bend radius. Nevertheless, the fiber was damaged again after completion of the last set of experiments. The fourth fiber used was a *hollow-core silica* fiber. Since the beam divergence did not meet the NA requirements of the fiber, the fiber burned at energies above 380 mJ. Of the fibers tested, the germanium oxide fiber performed best and seems to be more suitable for minimally invasive laserosteotomy. The only drawback of using this fiber was the high temperature that it reached at its tip, up to 75 °C, while the rest of the fiber tips did not exceed 60 °C. The high temperature of the germanium fiber tip can be mitigated in different ways, for example, by splicing in sapphire tips or adding a cooling system for the fiber. A lens system was designed to refocus the laser beam from the germanium fiber tip to 10 mm beyond the last lens. The two lenses, made of sapphire, are 2.38 (ball lens) and 6.35 mm (half-ball lens) in diameter. This system provided maximum output energies of 450 mJ and 370 mJ, and the maximum ablation depths achieved in pig and sheep bones were 10 and 6.8 mm, respectively. In free space, we obtained a 9 mm ablation depth at 370 mJ and 10 Hz. The difference in the ablation depths achieved by the free space and the fiber systems can be explained by the alignment of the irrigation and pressurized air system

used in the fiber system, which was not adequate for a working distance of 10 mm beyond the last lens to the bone surface.

7.2 Future research

Future work towards achieving an optimal laser system for ablating bone in minimally invasive surgeries could address any of the following three issues: (1) Improving the free-space Er:YAG laser system by using an Er:YAG laser with lower M^2 factor and higher energy. A member of our group is currently working in building such laser device. Such a system should also be coupled in the fibers, especially in the germanium oxide fiber. For higher input energy, the fiber tips must be treated to avoid rising temperatures. Also, using a new laser may necessitate a redesign of the lens system to refocus the beam at the bone's surface. A new design should allow for a working distance as short as 10 mm; the irrigation jet and the pressurized air should be well aligned, so that both constantly follow the ablated spot during the ablation process. Likewise, the temperature feedback system can be improved, for example, by using an OCT system to locally and constantly monitor the temperature of the ablated area during the ablation process. The OCT study for temperature control has already started in our laboratory [100]. (2) Using a low energy laser, such as the microsecond Thulium fiber laser, with a simple coupling process. Energy amplification occurs within the fiber medium, so coupling energies are usually very low. In addition, low-OH silica fibers with a core diameter of 100 μm could be used in endoscopic applications, as the fibers are more flexible. One possible drawback of this system is that the ablation would not likely be deep enough for some bone surgery applications; the energy is usually less than 1 mJ, and contrary to the case of Er:YAG lasers, the absorption of water near 2 μm is quite low. (3) Using a diode-pumped Er:YAG laser with higher repetition rate and lower energy. The main advantage is that this laser is compact and nowadays is made for easily coupling a terminated fiber for high power delivery.

7.3 Conclusion

For this thesis, a microsecond Er:YAG laser with a wavelength of 2.94 μm was used for deep ablation of cortical bone in free space and through fiber. First, the laser and irrigation systems were optimized for bone ablation, reaching maximum depths of 21 mm. Next, the laser light was coupled at its highest power, about 8 W; 820 mJ at 10 Hz into four different fibers. The germanium oxide GeO_2 fiber performed best among the fibers used, providing ablation depths of up to 10 mm. Overall, the combination of an Er:YAG laser, a thin water jet for irrigation, a temperature feedback system, and germanium oxide fibers, together with a miniaturized refocusing lens system, offer a promising system for implementation in a robotic endoscopic device for minimally invasive laserosteotomy procedures.

Bibliography

[1] Karolin Rönn, Nikolaus Reischl, Emanuel Gautier, and Matthias Jacobi. Current surgical treatment of knee osteoarthritis. *Arthritis*, 2011, 2011.

[2] Dennis R Wenger and JD Bomar. Human hip dysplasia: evolution of current treatment concepts. *Journal of orthopaedic science*, 8(2):264–271, 2003.

[3] Shahid R Aziz. Simon p. hullihen and the origin of orthognathic surgery. *Journal of oral and maxillofacial surgery*, 62(10):1303–1307, 2004.

[4] David Redfern and Anthony Michael Perera. Minimally invasive osteotomies. *Foot Ankle Clin*, 19(2):181–189, 2014.

[5] TH Maiman. Stimulated optical radiation in ruby. *Nature*, 187(4736):493–494, 1960.

[6] Leon Goldman, Donald J Blaney, Dan J Kindel, Daniel Richfield, and Ernst K Franke. Pathology of the effect of the laser beam on the skin. *Nature*, 197(4870):912–914, 1963.

[7] Leon Goldman, Donald J Blaney, DJ Kindel, and Ernst K Franke. Effect of the laser beam on the skin. *J Invest Dermatol*, 40(121):2, 1963.

[8] Richard Taylor, Gerald Shklar, and Fred Roeber. The effects of laser radiation on teeth, dental pulp, and oral mucosa of experimental animals. *Oral Surgery, Oral Medicine, Oral Pathology and Oral Radiology*, 19(6):786–795, 1965.

[9] Thomas E Gordon JR. Some effects of laser impacts on extracted teeth. *Journal of Dental Research*, 45(2):372–375, 1966.

[10] Raimund Hibst and Ulrich Keller. Experimental studies of the application of the er: Yag laser on dental hard substances: I. measurement of the ablation rate. *Lasers in Surgery and Medicine*, 9(4):338–344, 1989.

[11] Shlomo Assa, Steve Meyer, and Daniel Fried. Ablation of dental hard tissues with a microsecond pulsed carbon dioxide laser operating at 9.3-μm with an integrated scanner. In *Lasers in dentistry XIV*, volume 6843, page 684308. International Society for Optics and Photonics, 2008.

[12] Mozammal Hossain, Yukio Nakamura, Yoshishige Yamada, Yuichi Kimura, Naoto Matsumoto, and Koukichi Matsumoto. Effects of er, cr: Ysgg laser irradiation in human enamel and dentin: ablation and morphological studies. *Journal of clinical laser medicine & surgery*, 17(4):155–159, 1999.

[13] Jinze Qiu, Joel Teichman, Tianyi Wang, Badr Elmaanaoui, David Gamez, and Thomas E Milner. Comparison of fluoride and sapphire optical fibers for er:yag laser lithotripsy. *Journal of biophotonics*, 3(5-6):277–283, 2010.

[14] Kyung-won Baek, Waldemar Deibel, Dilyan Marinov, Mathias Griessen, Michel Dard, Alfredo Bruno, Hans-Florian Zeilhofer, Philippe Cattin, and Philipp Juergens. A comparative investigation of bone surface after cutting with mechanical tools and er: Yag laser. *Lasers in surgery and medicine*, 47(5):426–432, 2015.

[15] Waldemar Deibel, Adrian Schneider, Marcello Augello, Alfredo E Bruno, Philipp Juergens, and Philippe Cattin. A compact, efficient, and lightweight laser head for carlo®: integration, performance, and benefits. In *Novel Optical Systems Design and Optimization XVIII*, volume 9579, page 957905. International Society for Optics and Photonics, 2015.

[16] K-W Baek, W Deibel, D Marinov, Mathias Griessen, A Bruno, H-F Zeilhofer, Ph Cattin, and Ph Juergens. Clinical applicability of robot-guided contact-free laser osteotomy in cranio-maxillo-facial surgery: in-vitro simulation and in-vivo surgery in minipig mandibles. *British Journal of Oral and Maxillofacial Surgery*, 53(10):976–981, 2015.

[17] Max Planck. Entropie und temperatur strahlender wärme. *Annalen der Physik*, 306(4):719–737, 1900.

[18] Orazio Svelto and David C Hanna. *Principles of lasers*, volume 1. Springer, 2010.

[19] Alphan Sennaroglu. *Photonics and laser engineering: principles, devices, and applications*. McGraw-Hill, 2010.

[20] David A Harmin. Theory of the stark effect. *Physical review A*, 26(5):2656, 1982.

[21] Walter Koechner. *Solid-state laser engineering*, volume 1. Springer, 2013.

[22] G Keiser. Biophotonics: concepts to applications. 2016.

[23] Boris Majaron, Tanja Rupnik, and Matjai Lukac. Temperature and gain dynamics in flashlamp-pumped er: Yag. *IEEE journal of quantum electronics*, 32(9):1636–1644, 1996.

[24] Bradley J Dinerman and Peter F Moulton. 3-μm cw laser operations in erbium-doped ysgg, ggg, and yag. *Optics letters*, 19(15):1143–1145, 1994.

[25] SA Pollack and DB Chang. Upconversion-pumped population kinetics for 4 i 13/2 and 4 i 11/2 laser states of er 3+ ion in several host crystals. *Optical and quantum electronics*, 22(1):S75–S93, 1990.

[26] Emma Arbabzadah, Simon Chard, Hemmel Amrania, Chris Phillips, and Michael Damzen. Comparison of a diode pumped er: Ysgg and er: Yag laser in the bounce geometry at the 3 μm transition. *Optics express*, 19(27):25860–25865, 2011.

[27] MA Noginov, GK Sarkisyan, Valerii A Smirnov, Aleksandr Filippovich Umyskov, and Ivan A Shcherbakov. Experimental observation of the nonadditivity of various mechanisms of population inversion of the 4i11/2→ 4i13/2 transition of the er3+ ion in a ysgg: Cr3+: Er3+ crystal. *Soviet journal of quantum electronics*, 20(6):638, 1990.

[28] VI Zhekov, VA Lobachev, Tamara Mikhailovna Murina, and Aleksandr Mikhailovich Prokhorov. Efficient cross-relaxation laser emitting at λ= 2.94 μ. *Soviet Journal of Quantum Electronics*, 13(9):1235, 1983.

[29] Krishna Karki, Vladimir Fedorov, Dmitry Martyshkin, and Sergey Mirov. High energy (0.8 j) mechanically q-switched 2.94 μm er: Yag laser. *Optics Express*, 29(3):4287–4295, 2021.

[30] John David Jackson. Classical electrodynamics, 1999.

[31] Joseph W Goodman. *Introduction to Fourier optics*. Roberts and Company Publishers, 2005.

[32] Miles Padgett, Johannes Courtial, and Les Allen. Light's orbital angular momentum. *Physics today*, 57(5):35–40, 2004.

[33] J Meister, C Apel, R Franzen, and N Gutknecht. Influence of the spatial beam profile on hard tissue ablation part i: Multimode emitting er: Yag lasers. *Lasers in medical science*, 18(2):112–118, 2003.

[34] David Shuji Sumida, David A Rockwell, and Metin S Mangir. Energy storage and heating measurements in flashlamp-pumped cr: Nd: Gsgg and nd: Yag. *IEEE journal of quantum electronics*, 24(6):985–994, 1988.

[35] ISO11146-1. *Test methods for laser beam widths, divergence angles and beam propagation ratios. Part 1: Astigmatic and simple astigmatic beams*. ISO, 2005.

[36] Anthony E Siegman. New developments in laser resonators. In *Optical resonators*, volume 1224, pages 2–14. International Society for Optics and Photonics, 1990.

[37] David Bailey and Edwin Wright. *Practical fiber optics*. Elsevier, 2003.

[38] Govind P Agrawal. Optical communication: its history and recent progress. In *Optics in Our Time*, pages 177–199. Springer, Cham, 2016.

[39] Ajoy Ghatak and K Thyagarajan. *An introduction to fiber optics*. Cambridge university press, 1998.

[40] William K Johnston III. The birth of fiberoptics from" light guiding". *Journal of endourology*, 18(5):425–426, 2004.

[41] DH Sliney. What is light? the visible spectrum and beyond. *Eye*, 30(2):222–229, 2016.

[42] Milton M Zaret, Goodwin M Breinin, Herbert Schmidt, Harris Ripps, Irwin M Siegel, and Leonard R Solon. Ocular lesions produced by an optical maser (laser). *Science*, 134(3489):1525–1526, 1961.

[43] HC Zweng, M Flocks, NS Kapany, N Silbertrust, and NA Peppers. Experimental laser photocoagulation. *American journal of ophthalmology*, 58(3):353–362, 1964.

[44] Leon Goldman, Peter Hornby, Robert Meyer, and Bernard Goldman. Impact of the laser on dental caries. *Nature*, 203(4943):417–417, 1964.

[45] Josef F Bille, Andreas W Dreher, and Gerhard Zinser. Scanning laser tomography of the living human eye. In *Noninvasive diagnostic techniques in ophthalmology*, pages 528–547. Springer, 1990.

[46] Tanuj Dada, Reetika Sharma, Dewang Angmo, Gautam Sinha, Shibal Bhartiya, Sanjay K Mishra, Anita Panda, and Ramanjit Sihota. Scanning laser polarimetry in glaucoma. *Indian journal of ophthalmology*, 62(11):1045, 2014.

[47] Paisan Ruamviboonsuk and Wipawee Mahatthanatrakul. *Argon Laser Therapy*, pages 1–4. Springer Berlin Heidelberg, Berlin, Heidelberg, 2016.

[48] Naresh Kumar Yadav, Chaitra Jayadev, Anand Rajendran, and Manish Nagpal. Recent developments in retinal lasers and delivery systems. *Indian journal of ophthalmology*, 62(1):50, 2014.

[49] Walter J Stark, Wallace Chamon, Mary T Kamp, Cheryl L Enger, Erik V Rencs, and John D Gottsh. Clinical follow-up of 193-nm arf excimer laser photokeratectomy. *Ophthalmology*, 99(5):805–812, 1992.

[50] MH Niemz. Cavity preparation with the nd: Ylf picosecond laser. *Journal of dental research*, 74(5):1194–1199, 1995.

[51] Dragana Gabrić, Anja Baraba, Goran Batinjan, Marko Blašković, Vanja Vučićević Boras, Irina Filipović Zore, Ivana Miletić, and Elizabeta Gjorgievska. Advanced applications of the er: Yag laser in oral and maxillofacial surgery. In *A Textbook of Advanced Oral and Maxillofacial Surgery Volume 2*. IntechOpen, 2015.

[52] Y Kimura, P Wilder-Smith, and K Matsumoto. Lasers in endodontics: a review. *International Endodontic Journal*, 33(3):173–185, 2000.

[53] Adam Stabholz, Sharonit Sahar-Helft, and Joshua Moshonov. Lasers in endodontics. *Dental Clinics*, 48(4):809–832, 2004.

[54] Maarten A Meire, Tom Coenye, Hans J Nelis, and Roeland JG De Moor. In vitro inactivation of endodontic pathogens with nd: Yag and er: Yag lasers. *Lasers in medical science*, 27(4):695–701, 2012.

[55] Giuseppe Tam. Low power laser therapy and analgesic action. *Journal of clinical laser medicine & surgery*, 17(1):29–33, 1999.

[56] Stephen C Brady, Andrew Blokmanis, and Lawrence Jewett. Tattoo removal with the carbon dioxide laser. *Annals of plastic surgery*, 2(6):482–490, 1979.

[57] David B Apfelberg, Morton R Maser, and Harvey Lash. Argon laser treatment of decorative tattoos. *British journal of plastic surgery*, 32(2):141–144, 1979.

[58] Eric F Bernstein. Laser tattoo removal. In *Seminars in plastic surgery*, volume 21, page 175. Thieme Medical Publishers, 2007.

[59] Reinhold Brunner, Michael Landthaler, Diether Haina, Wilhelm Waidelich, and Otto Braun-Falco. Treatment of benign, semimalignant, and malignant skin tumors with the nd: Yag laser. *Lasers in surgery and medicine*, 5(2):105–110, 1985.

[60] Konstantin Moskalik, Alexander Kozlov, Eugeny Demin, and Ernest Boiko. The efficacy of facial skin cancer treatment with high-energy pulsed neodymium and nd: Yag lasers. *Photomedicine and laser surgery*, 27(2):345–349, 2009.

[61] Steven L Jacques. Laser-tissue interactions: photochemical, photothermal, and photomechanical. *Surgical Clinics of North America*, 72(3):531–558, 1992.

[62] Praveen C Ashok, Mario E Giardini, Kishan Dholakia, and Wilson Sibbett. A raman spectroscopy bio-sensor for tissue discrimination in surgical robotics. *Journal of biophotonics*, 7(1-2):103–109, 2014.

[63] Anita Mahadevan-Jansen and Rebecca Richards-Kortum. Raman spectroscopy for cancer detection: a review. In *Proceedings of the 19th Annual International Conference of the IEEE Engineering in Medicine and Biology Society.'Magnificent Milestones and Emerging Opportunities in Medical Engineering'(Cat. No. 97CH36136)*, volume 6, pages 2722–2728. IEEE, 1997.

[64] Hamed Abbasi, Georg Rauter, Raphael Guzman, Philippe C Cattin, and Azhar Zam. Laser-induced breakdown spectroscopy as a potential tool for autocarbonization detection in laserosteotomy. *Journal of biomedical optics*, 23(7):071206, 2018.

[65] David Fantarella and Larry Kotlow. The 9.3-μm co2 dental laser: Technical development and early clinical experiences. *Laser Dent*, 22(1):10–27, 2014.

[66] Kevin K Tremper and Steven J Barker. Pulse oximetry. *Anesthesiology: The Journal of the American Society of Anesthesiologists*, 70(1):98–108, 1989.

[67] Zivile Luksiene. Photodynamic therapy: mechanism of action and ways to improve the efficiency of treatment. *Medicina (Kaunas, Lithuania)*, 39(12):1137–1150, 2003.

[68] Stanisław Kwiatkowski, Bartosz Knap, Dawid Przystupski, Jolanta Saczko, Ewa Kedzierska, Karolina Knap-Czop, Jolanta Kotlińska, Olga Michel, Krzysztof Kotowski, and Julita Kulbacka. Photodynamic therapy–mechanisms, photosensitizers and combinations. *Biomedicine & Pharmacotherapy*, 106:1098–1107, 2018.

[69] Ashley J Welch, Martin JC Van Gemert, et al. *Optical-thermal response of laser-irradiated tissue*, volume 2. Springer, 2011.

[70] Raleigh A Holt and Robert E Nordquist. Holmium: Yag laser in dentistry: photoconditioning of dentinal surfaces. In *Laser Surgery: Advanced Characterization, Therapeutics, and Systems IV*, volume 2128, pages 308–318. International Society for Optics and Photonics, 1994.

[71] Cecie Starr, Christine Evers, and Lisa Starr. *Biology Today and Tomorrow with Physiology*. Nelson Education, 2012.

[72] M Forrer, M Frenz, V Romano, HJ Altermatt, HP Weber, A Silenok, M Istomyn, and VI Konov. Bone-ablation mechanism using co 2 lasers of different pulse duration and wavelength. *Applied Physics B*, 56(2):104–112, 1993.

[73] MEJ Curson and MS Duggal. Dental disease— structure of teeth. 2003.

[74] TG Barton, H-J Foth, M Christ, and K Hörmann. Interaction of holmium laser radiation and cortical bone: ablation and thermal damage in a turbid medium. *Applied optics*, 36(1):32–43, 1997.

[75] Elise F. Morgan, George L. Barnes, and Thomas A. Einhorn. Chapter 1 - the bone organ system: Form and function. In Robert Marcus, David Feldman, David W. Dempster, Marjorie Luckey, and Jane A. Cauley, editors, *Osteoporosis (Fourth Edition)*, pages 3–20. Academic Press, San Diego, fourth edition edition, 2013.

[76] HG Vogel. Influence of age, treatment with corticosteroids and strain rate on mechanical properties of rat skin. *Biochimica et Biophysica Acta (BBA)-General Subjects*, 286(1):79–83, 1972.

[77] RC Haut. The effects of orientation and location on the strength of dorsal rat skin in high and low speed tensile failure experiments. 1989.

[78] George W Dombi, Roger C Haut, and Walter G Sullivan. Correlation of high-speed tensile strength with collagen content in control and lathyritic rat skin. *Journal of Surgical Research*, 54(1):21–28, 1993.

[79] Richard S Aycock and Jerome M Seyer. Collagens of normal and cirrhotic human liver. *Connective tissue research*, 23(1):19–31, 1989.

[80] Alfred Vogel and Vasan Venugopalan. Mechanisms of pulsed laser ablation of biological tissues. *Chemical reviews*, 103(2):577–644, 2003.

[81] Boris Majaron, P Plestenjak, and Matjaž Lukač. Thermo-mechanical laser ablation of soft biological tissue: modeling the micro-explosions. *Applied Physics B*, 69(1):71–80, 1999.

[82] RM Verdaasdonk, C Borst, and MJC Van Gemert. Explosive onset of continuous wave laser tissue ablation. *Physics in Medicine & Biology*, 35(8):1129, 1990.

[83] Gerald L LeCarpentier, Massoud Motamedi, Linda P McMath, Sohi Rastegar, and Ashley J Welch. Continuous wave laser ablation of tissue: analysis of thermal and mechanical events. *IEEE Transactions on biomedical engineering*, 40(2):188–200, 1993.

[84] JC Allain, M Le Lous, L Cohen-Solal, S Bazin, and P Maroteaux. Isometric tensions developed during the hydrothermal swelling of rat skin. *Connective Tissue Research*, 7(3):127–133, 1980.

[85] DM Simanovskii, MA Mackanos, AR Irani, CE O'Connell-Rodwell, CH Contag, HA Schwettman, and DV Palanker. Cellular tolerance to pulsed hyperthermia. *Physical Review E*, 74(1):011915, 2006.

[86] Asghar Gholami, Molood Baradaran-Ghahfarokhi, Marjan Ebrahimi, and Milad Baradaran-Ghahfarokhi. Thermal effects of laser-osteotomy on bone: mathematical computation using maple. *Journal of medical signals and sensors*, 3(4):262, 2013.

[87] Haim Azhari. *Basics of biomedical ultrasound for engineers*. John Wiley & Sons, 2010.

[88] Joseph T Walsh Jr, Thomas J Flotte, R Rox Anderson, and Thomas F Deutsch. Pulsed co2 laser tissue ablation: effect of tissue type and pulse duration on thermal damage. *Lasers in surgery and medicine*, 8(2):108–118, 1988.

[89] Joseph T Walsh, Thomas J Flotte, and Thomas F Deutsch. Er: Yag laser ablation of tissue: effect of pulse duration and tissue type on thermal damage. *Lasers in surgery and medicine*, 9(4):314–326, 1989.

[90] Marco JP Brugmans, Jim Kemper, Geert HM Gijsbers, Freerk W van der Meulen, and Martin JC van Gemert. Temperature response of biological materials to pulsed non-ablative co2 laser irradiation. *Lasers in surgery and medicine*, 11(6):587–594, 1991.

[91] FRED Long and T Deutsch. Pulsed photothermal radiometry of human artery. *IEEE journal of quantum electronics*, 23(10):1821–1826, 1987.

[92] Laurens JT Meijering, Martin JC van Gemert, Geert HM Gijsbers, and Ashley J Welch. Limits of radial time constants to approximate thermal response of tissue. *Lasers in surgery and medicine*, 13(6):685–687, 1993.

[93] Martin JC van Gemert, Gerald W Lucassen, and AJ Welch. Time constants in thermal laser medicine: Ii. distributions of time constants and thermal relaxation of tissue. *Physics in Medicine & Biology*, 41(8):1381, 1996.

[94] Vishwa Pal, Chene Tradonsky, Ronen Chriki, Alexander Brodsky, Natan Kaplan, Israel Grossinger, Asher A Friesem, and Nir Davidson. Diffractive elements for generating top-hat beams with extended depth of focus.

[95] Vishwa Pal, Chene Tradonsky, Ronen Chriki, Natan Kaplan, Alexander Brodsky, Mickael Attia, Nir Davidson, and Asher A Friesem. Generating flat-top beams with extended depth of focus. *Applied optics*, 57(16):4583–4589, 2018.

[96] Cristian-Alexander Tulea, Jan Caron, Nils Gehlich, Achim Lenenbach, Reinhard Noll, and Peter Loosen. Laser cutting of bone tissue under bulk water with a pulsed ps-laser at 532 nm. *Journal of biomedical optics*, 20(10):105007, 2015.

[97] C Tulea, J Caron, H Wahab, N Gehlich, M Hoefer, D Esser, B Jungbluth, A Lenenbach, and R Noll. Highly efficient nonthermal ablation of bone under bulk water with a frequency-doubled nd: Yvo4 picosecond laser. In *Photonic Therapeutics and Diagnostics IX*, volume 8565, page 85656E. International Society for Optics and Photonics, 2013.

[98] Joseph Neev, Luiz B Da Silva, Michael D Feit, Michael D Perry, Alexander M Rubenchik, and Brent C Stuart. Ultrashort pulse lasers for hard tissue ablation. *IEEE Journal of Selected Topics in Quantum Electronics*, 2(4):790–800, 1996.

[99] Lüko Willms, Andrea Herschel, Mark H Niemz, and Thomas Pioch. Preparation of dental hard tissue with picosecond laser pulses. *Lasers in Medical Science*, 11(1):45–51, 1996.

[100] Arsham Hamidi, Yakub A Bayhaqi, Ferda Canbaz, Alexander Navarini, Philippe C Cattin, and Azhar Zam. Imaging photothermal-induced expansion of bone during laser osteotomy by phase-sensitive oct: preliminary results. In *Biomedical Spectroscopy, Microscopy, and Imaging*, volume 11359, page 113590K. International Society for Optics and Photonics, 2020.

Curriculum vitae

Lina M. Beltrán B.

Physicist
Ph.D candidate -
Biomedical Engineering

lmbbbb830@hotmail.com

Network

LinkedIn Link

ResearchGate Link

Orcid Link

Languages

Spanish

English

German

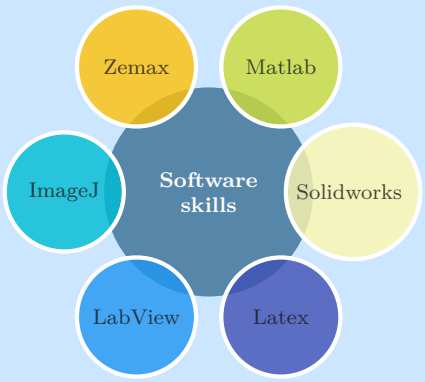

Soft skills

- Motivation
- Creativity
- Teamwork
- Leadership

Profile and latest projects

I am a physicist with emphasis in biophotonics, I have experience in interferometry, holography, laser technology and laser-tissue interaction. My PhD thesis is about designing and developing a laser system for cutting bone efficiently. The study of free space and fiber systems using a high power laser for developing such system is my main focus of study. My tasks are summarized as follows:

- Laser-tissue interaction: investigating the main forms of interaction and especially ablation of hard tissue. Using one of the best high power lasers known for hard tissue ablation and optimizing its performance by finding the most appropriate laser settings.
- Irrigation system: studying the impact of the irrigation system on the ablation rate and therefore, applying the appropriate irrigation to the tissue by means of an automated system.
- Fiber-based system for ablation: designing the coupling system from the free space to optical fibers. Investigating the properties of different optical fibers in order to efficiently transmit the energy. The main properties investigated are resistance to high power laser over time, bending radius, and tip temperature. The ablation rate of the fiber system for bone ablation is also investigated.

Education

2021 **Ph.D in Biomedical Engineering** University of Basel, Switzerland
Laser and wave-guides system for endoscopic/fiberscopic laser surgery.

2016 **Master in Advanced Optical Technologies** FAU, Germany

Master Thesis Max Planck Institute for the Science of Light
Obtaining bright squeezed vacuum in orbital angular momentum modes using a non-linear interferometer.

2013 **Bachelor in Physics** National University of Colombia, Colombia
Three-dimensional tomographic reconstruction of translucent objects.

Work experience

Currently **Researcher: Ph.D** University of Basel, Switzerland
Designing, developing, and optimizing a laser system for deep bone ablation though an endoscopic device. It includes a high power laser, fibers and irrigation system. PhD thesis defended.

2014-2016 **Internship: Teaching assistant** FAU Germany
Organizing, designing and teaching experimental optics to Master students of the program *Master in Advanced Optical Technologies*. **Basics of lasers**: teaching the students the basic working principles of a laser and how to built lasers in free space (NdYAG laser) and fiber-based (Erbium doped fiber) laser. **Advanced lasers**: teaching the students diffractive optics by means of a spatial light modulator and nonlinear effects such as second harmonic generation.

2010-2013 **Assistant** UNAL Colombia
Providing help in organizing the Experimental workshop for Master students of the program *Master's degree in natural science education*

2009 **Tutor of physics** UNAL Colombia
Teaching the students of the especial admission program (PAES) the basics of physics to help them reach the appropriate level of their respective bachelor studies.

List of publications

Journal papers

- **L. M. Beltrán B.**, F. Canbaz, S. E. Darwiche, K. M. R. Nuss, N. F. Friederich, P. C. Cattin, A. Zam. **Optical fibers for endoscopic high-power Er:YAG laserosteotomy.** *J. Biomed. Opt.* 26(9) 095002, September 2021.
DOI: https://doi.org/10.1117/1.JBO.26.9.095002

- **L. M. Beltrán B.**, F. Canbaz, A. Droneau, N. F. Friederich, P. C. Cattin, A. Zam. **Optimizing deep bone ablation by means of a microsecond Er:YAG laser and a novel water microjet irrigation system.** *Biomedical Optics Express*, December 2020.
DOI: https://doi.org/10.1364/BOE.408914

- **L. M. Beltrán B.**, **I. T. Schmidt**, N. Vulin, J. Widmer, J. G. Snedeker, P. C. Cattin, A. Zam G. Rauter. **Optimizing controlled laser cutting of hard tissue (bone).** *DE GRUYTER*, November 2018.
DOI: https://doi.org/10.1515/auto-2018-0072

- H. Abbasi., **L. M. Beltrán B.**, A. Hamidi, A. Droneau, F. Canbaz, R. Guzman, S. L. Jacques, P. C. Cattin, A. Zam. **Combined Nd:YAG and Er:YAG lasers for real-time closed-loop tissue-specific laser osteotomy.** *Biomedical Optics Express*, March 2020.
DOI: https://doi.org/10.1364/BOE.385862

Conference proceedings

- **L. M. Beltrán B.**, F. Canbaz, N. F. Friederich, P. Cattin, A. Zam. **Measurements of coupling efficiency of high power Er:YAG laser in different types of optical fibers.** Photonics West. "Optical Fibers and Sensors for Medical Diagnostics and Treatment Applications XX", *Proc. SPIE*, **11233**, 112331H, San Francisco USA, February 2020.
DOI: https://doi.org/10.1117/12.2546048

- **L. M. Beltrán B.**, G. Shayeganrad, G. Kosa, M. Zelechowski, G. Rauter, N. Friederich, P. Cattin, A. Zam. **Performance of Er:YAG laser-ablation in hard bone under different spray cooling conditions.** Photonics West. "Optical Interactions with Tissue and Cells XXIX", *Proc. SPIE*, **10492**, 104920B, San Francisco USA, February 2018.
DOI: https://doi.org/10.1117/12.2290929

- **L. Beltrán**, H. Abbasi, G. Rauter, N. Friederich, P. Cattin, A. Zam. **Effect of laser pulse duration on ablation efficiency of hard bone in microseconds regime.** *Proc. SPIE* **10453**, 104531S, Faro, Portugal, August 2017.
DOI: https://doi.org/10.1117/12.2272253

- H. Abbasi, **L. Beltrán**, G. Rauter, R. Guzman, P. Cattin, A. Zam. **Effect of cooling water on ablation efficiency in Er-YAG laserosteotome of hard bone.** *Proc. SPIE* **10453**, 104531I, Faro, Portugal, August 2017.
  DOI: https://doi.org/10.1117/12.2272138